Spring 2017

Development of a computational model to study instability and scapular notching in reverse shoulder arthroplasty

Vijay Niels Permeswaran
University of Iowa

DEVELOPMENT OF A COMPUTATIONAL MODEL TO STUDY INSTABILITY AND SCAPULAR NOTCHING IN REVERSE SHOULDER ARTHROPLASTY

by

Vijay Niels Permeswaran

A thesis submitted in partial fulfillment
of the requirements for the Doctor of Philosophy
degree in Biomedical Engineering in the
Graduate College of
The University of Iowa

May 2017

Thesis Supervisors: Professor Donald D. Anderson
Assistant Professor Jessica E. Goetz

Graduate College
The University of Iowa
Iowa City, Iowa

CERTIFICATE OF APPROVAL

PH.D. THESIS

This is to certify that the Ph.D. thesis of

Vijay Niels Permeswaran

has been approved by the Examining Committee for
the thesis requirement for the Doctor of Philosophy degree
in Biomedical Engineering at the May 2017 graduation.

Thesis Committee:

Donald D. Anderson, Thesis Supervisor

Jessica E. Goetz, Thesis Supervisor

Nicole M. Grosland

Carolyn M. Hettrich

David G. Wilder

To my loving wife, caring family, and supportive friends, I could not have accomplished so much without you.

ACKNOWLEDGEMENTS

I would like to thank my advisors Don Anderson and Jess Goetz. They provided me an excellent environment to develop my engineering, technical communication, and research skills. Also, I would like to thank the other members of the lab for helping me conduct research. In addition, I would like to thank my fellow graduate students, past and present, for pushing me to achieve more. Finally, I would like to thank my loving wife, my family, and my friends for their care and support throughout this process.

ABSTRACT

Reverse shoulder arthroplasty (RSA) is a common treatment for individuals with arthritis of the glenohumeral joint in the presence of a massive rotator cuff tear. Though this procedure has been effective in restoring function to these individuals, it has also been associated with high early to mid-term complications, such as scapular notching and instability.

A finite element (FE) modeling approach has previously been used to study the range of motion an individual with RSA could adduct their arm the polyethylene liner impinged on the inferior scapular bone and the contact stress at the impingement site. This model was then validated in a physical experiment using cadaveric tissue.

In this document, I introduce modifications to that FE model to further study instability and scapular notching risk. First, modern RSA implant geometries were introduced into the model, and the effect of polyethylene liner rotation and glenoid version on impingement-free range of motion and instability risk was assessed. Then, a physical material property characterization of rotator cuff tissues present after RSA was performed. Finally, those material properties and continuum elements representative of the rotator cuff tendons were introduced into the FE model. Throughout all of these studies, greater complexity and fidelity was added to improve the ability to model both contact at the impingement site and potential dislocation events through more accurate loadings and boundary conditions.

PUBLIC ABSTRACT

Rotator cuff tears are the most prevalent shoulder injury in the US, accounting for over 4.5 million clinical visits a year. Patients suffering from massive rotator cuff tears over a prolonged period can develop painful arthritis, leading to shoulder dysfunction. Fortunately, a new type of implant system was developed for these patients called a reverse shoulder arthroplasty (RSA). In this design, the natural ball-in-socket anatomy of the shoulder is reversed, replacing the humeral head (ball) with a humeral cup (socket) and the glenoid cavity (socket) with a glenosphere (ball). This change in anatomy provides function and relives pain for these patients. Unfortunately, this implant has also been associated with high rates of complications, such as instability or dislocation and scapular notching, a phenomenon where the humeral cup contacts and grinds against the bone of the shoulder blade, causing the bone and polyethylene cup to wear away.

In this document, I introduce a computer model studying RSA in which contact stresses can be computed. This allows for testing and experimentation of various implantation techniques to determine which techniques produce greater risks for these complications. Specifically, I analyze what effect glenosphere tilt and humeral polyethylene cup rotation have on dislocation risk. In addition, I conducted physical testing of cadaveric shoulder tendons that prevent dislocation to determine their mechanical behavior. These values were then used to enhance the computer model to better study how weak or strong shoulder tendons affect dislocation and scapular notching.

TABLE OF CONTENTS

LIST OF TABLES

LIST OF FIGURES

CHAPTER 1: LITERATURE REVIEW

Clinical Topics

Shoulder Anatomy

The upper extremity joins the trunk through the glenohumeral joint, the primary load bearing joint of the shoulder. The glenohumeral joint is comprised of the spherical proximal humerus mating with the shallow dish-shaped glenoid cavity of the lateral scapula. Unlike the hip, the most common ball-in-socket joint of the human body, the glenohumeral joint relies on soft tissue tension for its stability rather than bony congruity. The congruity of the shallow glenoid cavity is aided by the glenoid labrum, a ring of fibrocartilaginous tissue running around the margin of the glenoid. In addition, the humeral head is stabilized by the action of the rotator cuff [1].

The rotator cuff is a set of four muscles, the subscapularis, supraspinatus, infraspinatus, and teres minor, and their respective tendons running from the medial scapula across the joint space and attaching to the humeral head. The subscapularis, as its name implies, lies just anterior or deep to scapula when viewing the trunk posteriorly. It crosses the joint space anteriorly, functions as an internal rotator of the humerus, and prevents anterior dislocation. The supraspinatus and infraspinatus lie posterior or superficial to the scapula. The supraspinatus lies above the spine of the scapula, assists in abduction, and pulls the humeral head into the glenoid cavity, while the infraspinatus lies below the spine of the scapula, performs external rotation of the humerus, and resists posterior dislocation. Finally, the teres minor originates inferior to the infraspinatus on the scapular wing, assisting the deltoid in direction of abduction while also helping to prevent superior translation [2-4].

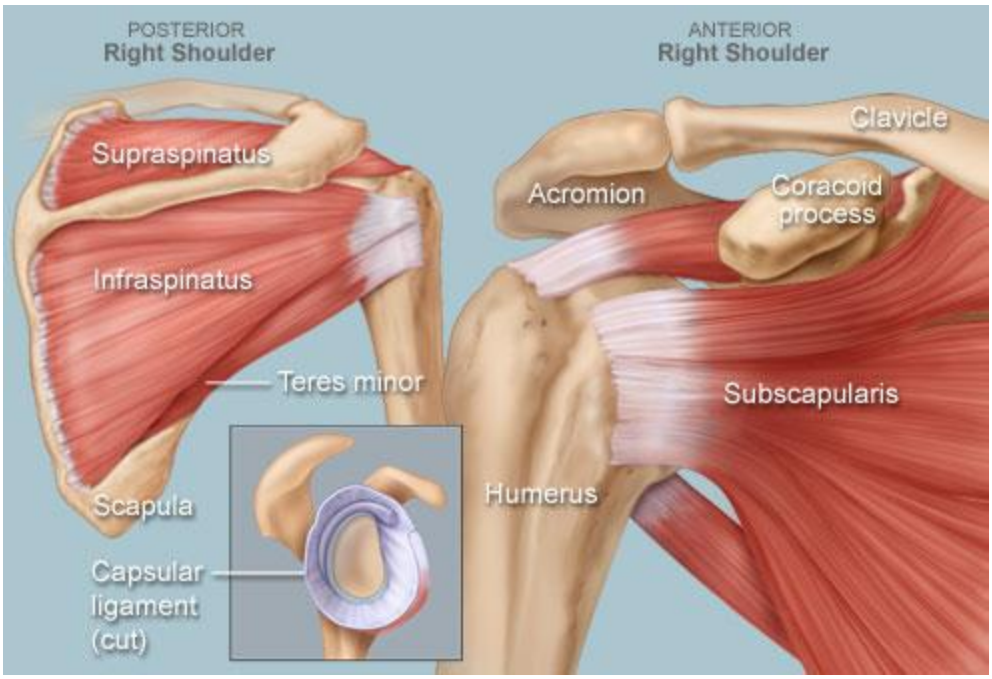

Figure 1: Anatomy of the glenohumeral joint. The rotator cuff musculature (subscapularis, supraspinatus, infraspinatus, and teres minor) are shown along with the humeral head and glenoid cavity. Image taken from WebMD [5].

Cuff Tear Arthropathy

In a healthy shoulder, the coordinated action of all of these muscles allows the shoulder to operate with a great deal of mobility, dexterity, and freedom. Understandably, disease of this structure can be debilitating. Rotator cuff tear is the most common shoulder injury in the United States, leading to over 4.5 million patients visit a year [6]. For many of these individuals, rotator cuff tears can lead to another disease known as cuff tear arthropathy (CTA), characterized by reduced shoulder strength, reduced range of motion, reduced shoulder function, osteoarthritis, and pseudoparalysis (small or no active range of motion, but near full passive range of motion) [7-12].

Figure 2: Patient demonstrating pseudoparalysis. The patient presents with extremely limited range of motion in active abduction. If assisted, however, the patient would be able to achieve greater range of motion in passive abduction. Taken from Gerber et al. 2009 [10].

Neer et al. were the first to characterize CTA [12]. They hypothesized that the disease started with a large rotator cuff tear, usually of the supraspinatus, degrading the stability of the glenohumeral joint. As discussed earlier, the action of the supraspinatus is to assist with abduction by pulling the humeral head into the glenoid cavity. Without this, the action of the deltoid, a much larger, more powerful abductor, translates the humeral head superiorly rather than rotating the humerus about a stable center of rotation. The effect is the humeral head and glenoid cavity experience uneven rocking contact rather than smooth rotating contact, damaging the cartilage at the interface. This increasing damage to the cartilage leads to greater arthritis and pain.

Shoulder Arthroplasty

The first proposed treatment of CTA was anatomic total shoulder arthroplasty (TSA) [8, 13-17]. Glenohumeral OA had been treated historically with TSA. Because of the pre-existing technology and the similarity of CTA to other glenohumeral OA, TSA

was suggested as a solution to pain and dysfunction caused by CTA. Although this treatment was able to relieve CTA patients of their pain, these patients were unable to regain healthy shoulder function. CTA patients undergoing this procedure did not regain a stable glenohumeral joint because the arthroplasty did nothing to restore the rotator cuff structures. These patients often presented with generic instability as well as glenoid loosening. This loosening was caused by rocking contact described as rocking horse loosening. Because of this, a new system needed to be developed to treat these patients.

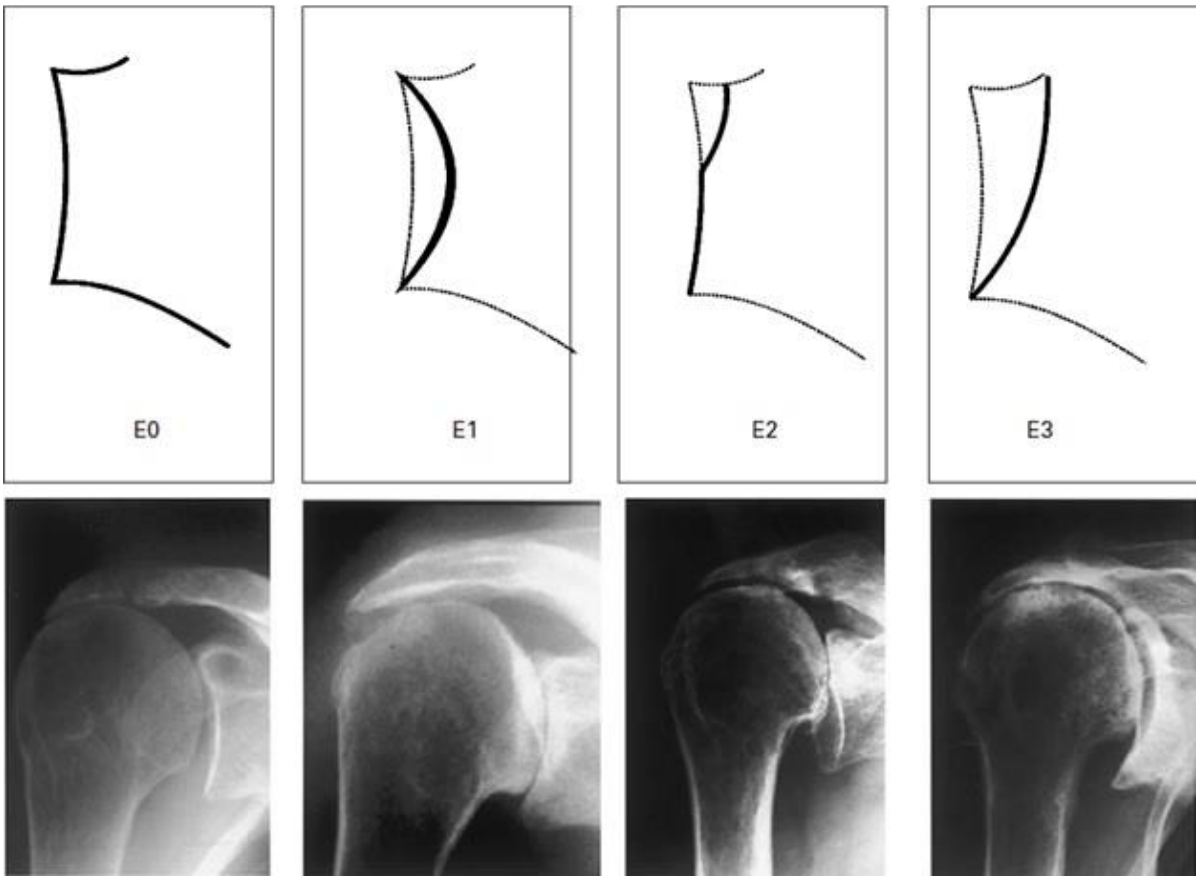

Figure 3: Progression of gleno-humeral arthritis due to massive rotator cuff tear. The first stage (E0) reveals superior migration of the humeral head into the acromion due to instability of the joint center. The instability leads to dysfunctional biomechanics of the joint. When TSA is performed in such a joint, the superior migration and instability leads to a complication known as rocking horse loosening of the glenoid component, due to alternating superior and inferior loads on the glenoid baseplate [18].

Reverse Shoulder Arthroplasty

Reverse shoulder arthroplasty (RSA) was first introduced by Grammont in 1983, and many of the design choices from then are still present today [7, 8]. With RSA, the natural anatomy of the glenohumeral joint is reversed. The glenoid cavity, naturally a shallow concave surface, is replaced by a metallic, usually hemispherical, convex surface or glenosphere. The humeral head, a normally spherical convex surface, is replaced by a concave, usually polyethylene, cup or liner. This reversal in join geometry changes the center of rotation from the humeral head to the glenosphere. Because of this, the center of rotation is now fixed with respect to the scapula, providing constraint usually provided by the supraspinatus. In addition, the center of rotation has been medialized and distalized, providing the deltoid a greater mechanical advantage. This advantage allows the deltoid to more easily rotate or abduct the arm. Many design factors have changed over time, such as polyethylene cup design, neck-shaft angle, hemi vs. ¾ spheres, etc., but these factors (convex glenoid shape with scapular fixation, concave humeral polyethylene liner) have remained consistent between implant designs and companies.

Figure 4: Traditional Grammont style RSA design demonstrated by the antiquated Delta III prosthesis (Depuy Synthes, Warsaw, IN) and a modern design demonstrated by Tornier Aequalis Ascend Flex Reversed system (Wright Medical, Memphis, TN).

RSA has proven to be very successful for treating individuals suffering from CTA. Previously, these patients had limited shoulder function and terrible pain. However, with RSA, these patients return to near-healthy range of motion and strength without pain [8, 10, 19-24]. These successes have lead clinicians to expand the indications for RSA to younger, higher demand patients, with severe rotator cuff tears in the absence of OA [25-36]. Usage of RSA has been shown to be on the rise, with more than 30,000 people undergoing RSA every year, up from 0 just 10 years ago [34].

Reverse Shoulder Arthroplasty Complications

Unfortunately, the change in geometry accompanying RSA has also led to unforeseen complications [30, 31, 33, 35-41]. Two of the most common complications are scapular notching and instability [7, 16, 31, 35, 41-56]. Scapular notching is a phenomenon in which the humeral polyethylene liner contacts or impinges on the lateral pillar of the scapula, inferior to the glenoid. This impingement causes macroscopic wear of both the polyethylene liner and the scapular bone, the latter of which can be observed radiographically. Over time, this wearing can lead to revision surgery due to the damage of the polyethylene cup, glenoid fixation loosening due to bone loss, or both. Our previous work has indicated that impingement is likely to happen during normal abduction. The work presented in this document will show that impingement occurs in even small degrees of external rotation.

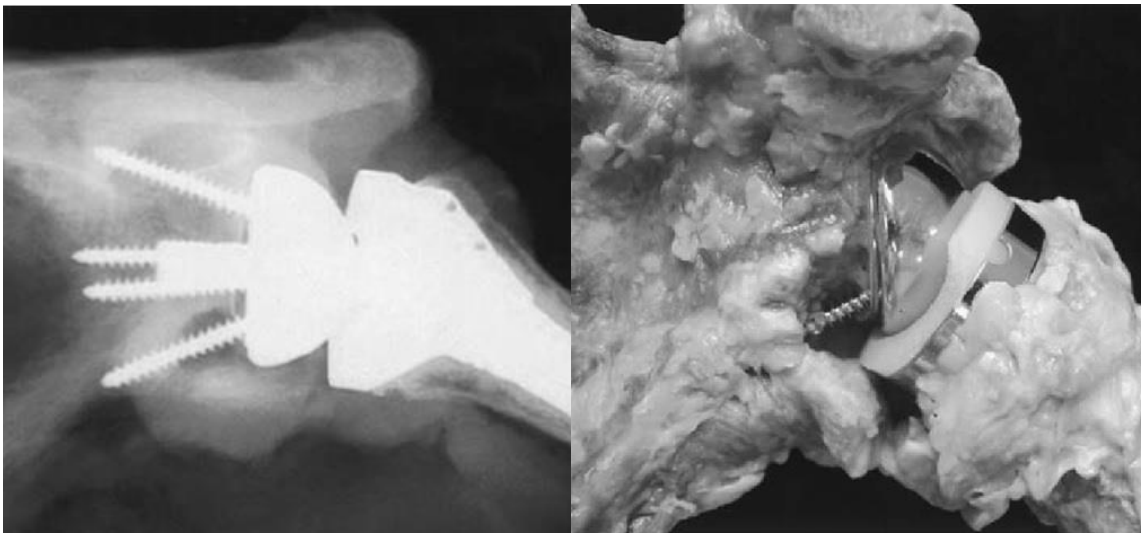

Figure 5: Radiograph and dissected image of cadaveric subject with RSA presenting scapular notching. The radiograph displays radiolucency near the inferior fixation screw of the glenosphere baseplate, and the dissection verifies the loss of bone in this region. The damage to the radio-transparent polyethylene liner is not found however until the full dissection is completed. Taken from Nyffeler et al. 2004 [57].

The other most common complication of RSA is instability leading to dislocation. This complication occurs due to imbalance of remaining rotator cuff soft tissue, improper deltoid tensioning, impingement, or many other factors. The imprecise nature of the cause of instability is also what makes it so difficult to treat [31, 35, 41, 54-56].

Research Hypotheses and Project Purpose

Previously, a finite element model was created studying impingement free range of motion in scapular and coronal plane abduction and effective deltoid muscle strength with varying medialization and lateralization of the glenoid center of rotation [58]. Greater lateralization of the center of rotation improved impingement-free range of motion and created small decreases in effective deltoid muscle strength. Following that study, a cadaveric validation was performed of that model. Contact stress at the impingement site was measured using a Tekscan sensor (Tekscan Inc., South Boston, MA). The contact patches computed in the FE model compared favorably with the

contact measured physically in the cadaveric model [59]. These studies can be found in Appendices A and B.

The broad hypothesis of this work is that since impingement is inevitable, soft tissue constraint is the deciding factor in determining the risk of developing scapular notching and instability. When impingement occurs, if too little soft tissue constraint is present, the humerus will lever off of the glenosphere, and the patient will likely experience instability. However, if the soft-tissue constraint of the gleno-humeral joint is strong, when impingement occurs, the polyethylene liner will be pulled into the scapular bone, leading to high contact stresses at the impingement site. These complications can be thought to exist on two ends of the spectrums of soft tissue constraint. This hypothesis suggests that there may be an optimal implantation in which stability is achieved while minimal contact stress is generated during impingement. The work reported in this document aims to identify this ideal implantation and includes studies performed to identify what conditions increase dislocation and scapular notching risk. In order to answer these questions, computational finite element models informed by physical testing and literature were created.

Engineering Topics

FE Modeling

Finite Element (FE) modeling is an important engineering tool used to study mechanics computationally. In finite element analysis, the object being modeled is divided into a *finite* number of elements. These elements can be 1, 2, or 3 dimensional entities with various geometric shapes. However, the vertices of these elements are always composed of nodes. Forces and displacements can be applied to these nodes, and

the deformation, strain, and stress can be computed. The advantages of FE modeling include lower costs than physical testing, repeatability of experiments, and the ability to create models and study geometries not currently present or available. Prior to the development of this technique, the only methods to determine internal stresses of materials were physical measurement using physical strain gauges or estimated using difficult or impossible to derive analytical mathematical models.

Abaqus/Standard

Abaqus Standard is a very common FE program. This program utilizes an implicit FE solving technique. The mechanics of an implicit static FE model are applications of Newton's Second Law of Motion, or $F = M\ddot{u}$, where F is the sum of all forces, M is the mass of the object, and $\ddot{u}$ is the second time derivative of the displacement (or the acceleration) of the object in question. Quite simply, this equation dictates that the acceleration of an object is directly related to the forces applied to it, and inversely related to the mass of the object. In a static example, the object or model is in static equilibrium meaning there is no acceleration of the object being modeled. Because of this, force equilibrium must be preserved or $F = 0$. This means that the internal forces must equal the external forces.

In Abaqus/Standard, the internal forces are notated as *I* and the external forces are notated as *P*. The internal forces developed due to the application of an external load are affected by the stiffness of the object itself and its deformation. Therefore, $I = Ku$, where K is the stiffness of the model, stored as a matrix, and u is the displacement of every degree of freedom of every node, stored in a vector. The final equation becomes

$Ku = P$, where the matrix K and external force vector P are known, and the displacement vector is solved. Once the displacements are solved, these values can be used to calculate the strains and stresses in the elements. In a static loading model, this is extremely efficient.

However, in the dynamic case, Abaqus/Standard is solving a much more complex equation due to the inclusion of motion and inertia. In this case, Abaqus/Standard is attempting to compute displacements of nodes and satisfy dynamic equilibrium simultaneously. The dynamic equation being solved at time iteration j becomes

$$K_j c_j = P_j - I_j - M_j \ddot{u}_j$$

where c_j is an incremental correction to incremental displacements Δu_j, P_j is the external forces vector, I_j is the internal forces vector, $M_j \ddot{u}_j$ is the inertial force vector, and K_j is the linear combination of the tangent stiffness matrix and the mass matrix for the iteration. A full Newton iterative solution method is utilized to solve a large number of simultaneous equations until several quantities are within prescribed tolerances such as force residual and displacement correction. Still Abaqus/Standard is remarkably efficient with a quadratic rate of convergence. However, for models with highly discontinuous contact events, the time increments over which the Newton solver is calculated can be very small, decreasing the convergence rate, and creating exceedingly long computational run times (on the order of days or weeks, even).

Abaqus/Explicit

Abaqus/Explicit is a different Abaqus solver that excels in this particular application. Both solvers are attempting to generally solve the equation:

$$M\ddot{u} = P - I$$

In Explicit however, the central difference rule is used to *explicitly* integrate through time to solve for new nodal positions. It does this in an iterative fashion by using kinematic conditions at one time increment to calculate the kinematic conditions at the next time increment. The nodal accelerations are solved at the beginning of the time iteration by direct multiplication of the inverse of the mass matrix and the difference of internal forces from the external forces.

$$\ddot{u}|_t = (M)^{-1} \cdot (P - I)|_t$$

Using the nodal velocities from the last half iteration and the nodal accelerations from the start of the current time iteration, the nodal velocities at the next half time iteration are solved using the central different rule.

$$\dot{u}|_{\left(t+\frac{\Delta t}{2}\right)} = \dot{u}|_{\left(t-\frac{\Delta t}{2}\right)} + \frac{\left(\Delta t|_{(t+\Delta t)} + \Delta t|_{(t)}\right)}{2}\ddot{u}|_t$$

Then using the velocity at the next half iteration, the nodal displacements at the last time iteration, and the total iteration length, the nodal positions at the next time iteration are computed.

$$u|_{(t+\Delta t)} = u|_{(t)} + \Delta t|_{(t+\Delta t)}\dot{u}|_{\left(t+\frac{\Delta t}{2}\right)}$$

The new nodal positions are used to calculate element strains, element strain rates, and stresses. Finally, the nodal positions are used to calculate the next internal nodal force vector. The time iteration is advanced and the cycle is repeated. In order for this procedure to be accurate, the time iteration lengths must be very small. As such, typical Abaqus/Explicit jobs require 10,000 to 100,000 iterations per step. However, these iterations can be computed extremely quickly. The explicit solving method does not

required a global stiffness matrix, an essential part of the implicit solving technique, and since the state of the model is advanced explicitly, iterations, convergence checks, and tolerances are not required. Finally, equilibrium is calculated automatically at the beginning of each iteration, allowing for faster computation. For these reasons, Abaqus/Explicit is an efficient FE solver for computing highly discontinuous contact.

Shoulder FE Modeling

A wealth of impressive FE models has been published studying the native glenohumeral joint. Recently, a thorough review of these models identified 18 published models studying native glenohumeral geometry, 9 studying total shoulder arthroplasty, and 2 models studying both total and reverse shoulder arthroplasty [60]. Examples of excellent FE modeling of the glenohumeral joint include the models studying the glenohumeral capsule produced by the Musculoskeletal Research Center at the University of Pittsburgh [61-68]. The culmination of many years of work by this research group led to subject-specific FE modeling of the glenohumeral joint. In these studies, isotropic Veronda-Westmann hyperelastic material properties of the capsule were calculated from cadaveric tissue. Optical motion tracking markers were placed on the capsule surface, the shoulder joint underwent a prescribed motion, and the deformation of the capsule was recorded. Afterwards, the capsule was sectioned out, and each section was tested uniaxially. Accompanying finite element modelling was conducted of each section, and optimization was performed to obtain the best fitting material model parameters. Using this approach, the authors were able to produce a subject specific model of the glenohumeral capsule. This type of soft tissue model fidelity is important and necessary in studying complications such as instability.

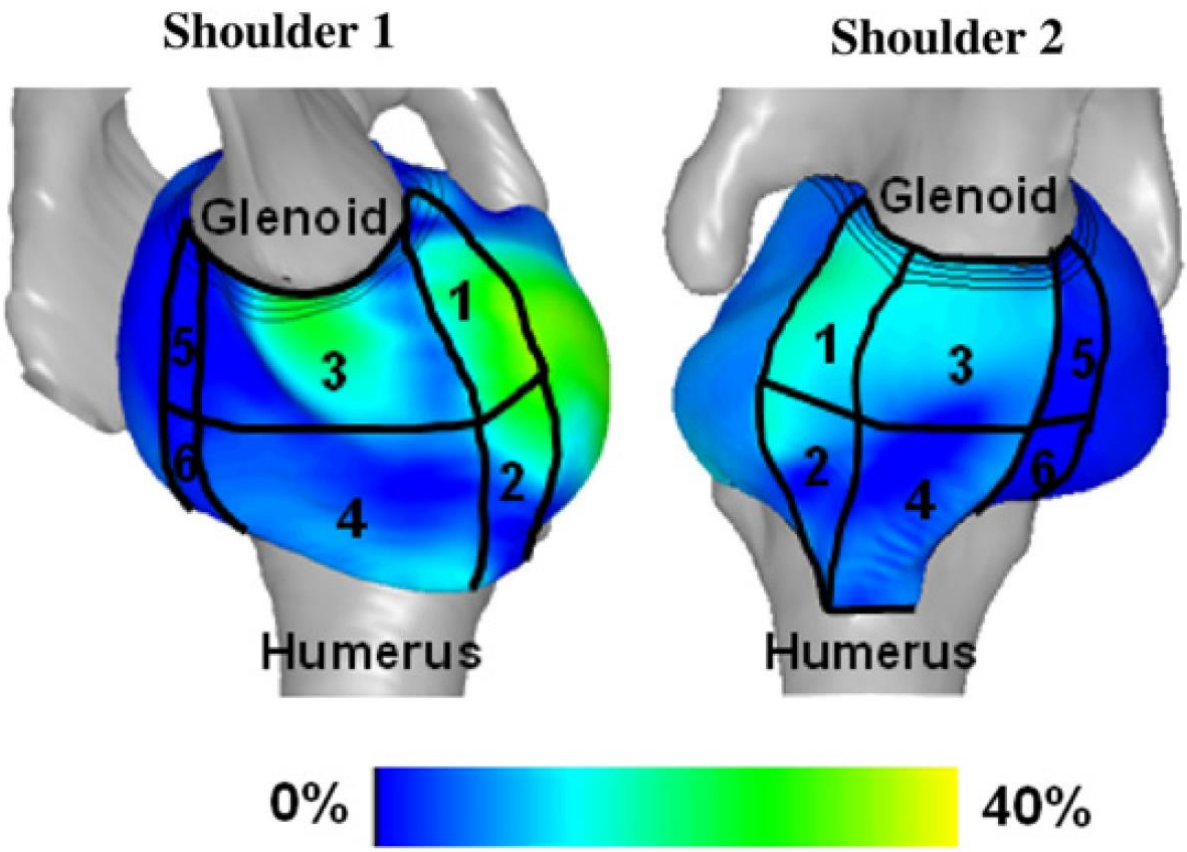

Figure 6: Strain distribution in the glenohumeral capsule of two subject-specific FE models. Combined computational and physical testing of the six capsule segments identified above was performed to compute optimal material property parameters. Taken from Drury et al. 2011 [67].

RSA FE Modeling

Unfortunately, relatively little FE modeling has been conducted studying RSA. Currently, a PubMed search of "reverse shoulder arthroplasty finite element" returns 16 total articles, including two articles generated by this lab. Many of these articles focus on glenosphere fixation and the stresses generated by the fixation in the glenoid region, as well as micromotion of the glenoid fixation [69-78]. Although such research is important in ensuring the safety of glenoid fixation, the models used to study glenosphere fixation are fairly simplistic, especially when compared to other orthopaedic and arthroplasty research available in the literature [79-83]. Some limitations of those models include true

and pseudo-two-dimensionality, lack of contact, static loadings boundary conditions, outdated implant geometry, limited computation or presentation of stresses, and lack of bony anatomy. The primary complications of RSA are scapular notching and instability. Unfortunately, the simplification of bone and soft tissue leaves many of these models unable to study these complications.

An example of some of these limited models is presented by Denard et al. 2016 [76]. In this study, the authors state "A 3D finite element analysis (FEA)" was performed to determine the effect of glenoid-sided lateralization in reverse shoulder arthroplasty. In this study, the authors are primarily concerned with stresses at the interface between the baseplate fixation screws and the bone, as well as the glenosphere and its baseplate. For this purpose, they modeled only the glenosphere, the baseplate, and screws. Furthermore, instead of modeling bony scapular anatomy, the authors modeled a rigid foam block of polyurethane, replicating ASTM testing standard F2028 [84]. The humerus and humeral implants were not modeled. The models were statically loaded with a distributed load equaling 750 N in both compressive and superior directions. The stresses in the model were analyzed, and implantations with greater lateralization were found to experience greater stress.

The results of this study clearly show that with greater lateralization, loads applied to the glenosphere create greater stress due to a larger moment arm. However, the translation of these results to a clinical setting is questionable. The static, purely compressive and superior shear loading modeled is simplistic, and applied equally across the glenosphere, rather than focally, as through a contact interface. In addition, the bone is modelled as an ideal block of foam. However, the glenosphere baseplate is implanted

into the scapula, a thin, complex bone in which the baseplate screws are likely to perforate, causing stress risers. Lastly, although the model claims to be three-dimensional, the results are displayed as two-dimensional cross sections, and furthermore, the model itself gains little from being three-dimensional. The loadings are applied symmetrically about a spherical implant, oriented non-anatomically. Many of these limitations are reminiscent of other FE studies present in the literature.

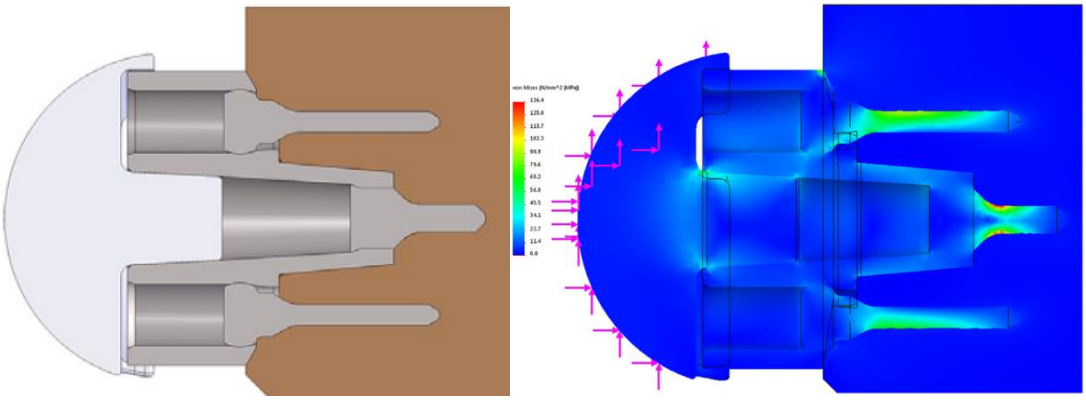

Figure 7: Undeformed and Von Mises stress plots for the model introduced in Denard et al. 2016 [76]. Limitations of this model include lack of contact, static boundary conditions, and lack of three-dimensional loading.

Greater model complexity can be found in a few models studying RSA. An example of current state of the art work, can be found by reading Langohr et al. 2016, in which the authors produce a fairly robust, high resolution finite element model in order to examine contact mechanics of reverse total shoulder arthroplasty during abduction [85]. In this study, an FE model of the glenosphere and humeral stem with polyethylene liner was created. The variables of interest were the neck-shaft angle (the angle between the normal of the liner and the axis of the stem), the depth of the polyethylene liner, and the diameter of the glenosphere. Three neck-shaft angle models, two glenosphere diameters, and three cup depths were paired with each other, and statically loaded with fixed loads at 14 physiologic abduction angles. The primary finding was larger neck-shaft angles

produced smaller contact area and greater contact stresses at the interface when compared to smaller neck-shaft angles. The authors presented a contact stress plot of the polyethylene liner with greater stress present in the inferior portion of the liner than the superior. They assert that this increase in contact stress in the liner is likely leading to the polyethylene liner damage present in scapular notching.

These findings raise some concerns. The contact stresses presented in this study (~1 MPa) are not large enough to produce notching. Furthermore, the distribution of the contact stress, equally about the entire inferior region of the liner, does not match with retrievals where small focal regions of the liner are worn away. This article is an example of confusion present around the biomechanics of RSA, as well as the danger in utilizing a static, implant-only, planar model of RSA to explain complex phenomena caused by the geometry of the bone and the multiplanar dynamics of the shoulder.

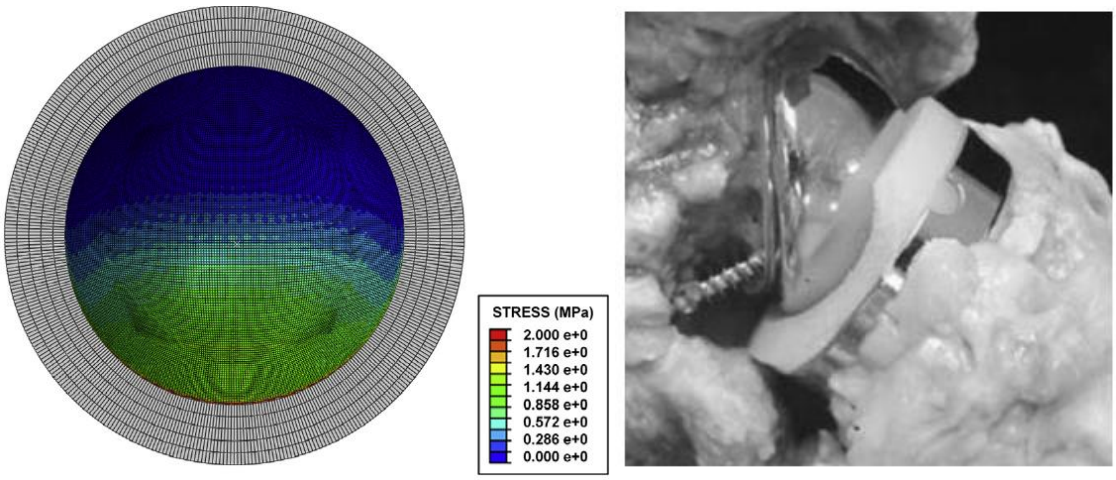

Figure 8: Contact stress mapping taken from Langohr et al 2016 (Left) and image of a damaged polyethylene liner taken from Nyffeler et al. 2013 (Right) [57, 85]. Although higher stress is present in the FE model, the contact stress values present are likely not high nor focal enough to be responsible for the type of liner damage associated with scapular notching.

Current FE Model Capabilities and Limitations

In general, there are no current FE models of RSA with sufficient complexity to adequately study instability and scapular notching. In order to perform this type of analysis, a fully dynamic FE model is required, in which contact between the scapular bone and polyethylene liner is modeled and quantified. In addition, in order to study instability, the model must be able to compute unstable, dislocation events.

Previously, we developed a FE model utilizing Abaqus/Explicit. The model is comprised of continuum elements representing the glenoid region of the scapula, a glenosphere, the humeral polyethylene liner and stem, and the humeral head. The model also possesses two soft tissue springs located anteriorly and posteriorly symmetrically about the center of rotation and a series of slipring connector elements, representing the deltoid muscle. Capabilities of the model include the ability to compute contact, between any surfaces that touch, just as would happen *in vivo*. Furthermore, the model can compute the complex, discontinuous contact that occurs at the impingement site interface between the polyethylene liner and the inferior scapula, causing the humerus to lever away from the glenosphere during motions such as extension/flexion, abduction/adduction, and external/internal rotation.

But more is required from the model. The soft tissue in that previous model is represented by two nonlinear elastic springs. These springs provide support and constraint to the humerus, allowing for modelling the humerus in a clinically relevant manner as a floating ball in socket joint, capable of achieving dislocation. In addition, these springs are computationally inexpensive, allowing for faster run times. This soft tissue representation has some limitations. Foremost, contact is not calculated for spring elements. As such, the springs can and do penetrate through different continuum portions

of the model as the humerus rotates. When this happens, the line of action of the soft tissue springs loses relevancy, as the soft tissue of the shoulder cannot, obviously, intersect the implants and bones *in vivo*. In turn, the direction of the tensile loads delivered by these springs deviate from inferred *in vivo* loading conditions. To resolve this, continuum element representation of the soft tissue present after RSA is needed.

Several steps were required to add this type of representation to the model. First, material properties of the relevant soft tissue were required. These material properties must then be incorporated into either a linear elastic, nonlinear elastic, hyperelastic, or some other type of continuum material model. Finally, the geometry of the soft tissues modeled must be acquired and converted into a finite element mesh.

Rotator Cuff Tendon Testing

The primary tissues responsible for stability of the joint post-RSA are the subscapularis and infraspinatus tendons. Thorough survey of scientific literature found few articles available in which the material properties of these tissues were quantified, especially in human cadaveric tissue. This is to be expected. The most important muscle and tendon of the rotator cuff is the supraspinatus. As such, the vast majority of the literature concerns material property quantification of the supraspinatus [86-92].

Two articles concerning subscapularis and infraspinatus tissue properties were written and published by the same research group, with nearly identical testing protocols [93, 94]. In each of those studies, 19 cadaveric specimens were analyzed. For each specimen, the subscapularis, infraspinatus, and teres minor tendons were dissected away from the scapula, and the muscle bellies were bluntly removed to isolate the tendons. The distal two thirds of the humerus were transected, and the proximal third was potted in

PMMA bone cement. The potted humerus was placed in a custom made fixture allowing rotation about the long axis of the bone, and the abduction angle of the fixture could be changed. The proximal end of the tendon was fixed in a cryo clamp rigidly fixed to a load cell and linear variable differential transducer. The humerus was held fixed, and the tendon underwent 10 pre-conditioning cycles of 1.5 mm displacement at 0.5 Hz. Then the tendon was destructively tested at 100% strain over 1 second. The load-displacement curve for each specimen was recorded, and, using calculated cross sectional area values, stress-strain curves were generated. The linear elastic modulus was fit to the linear region of each curve of each test.

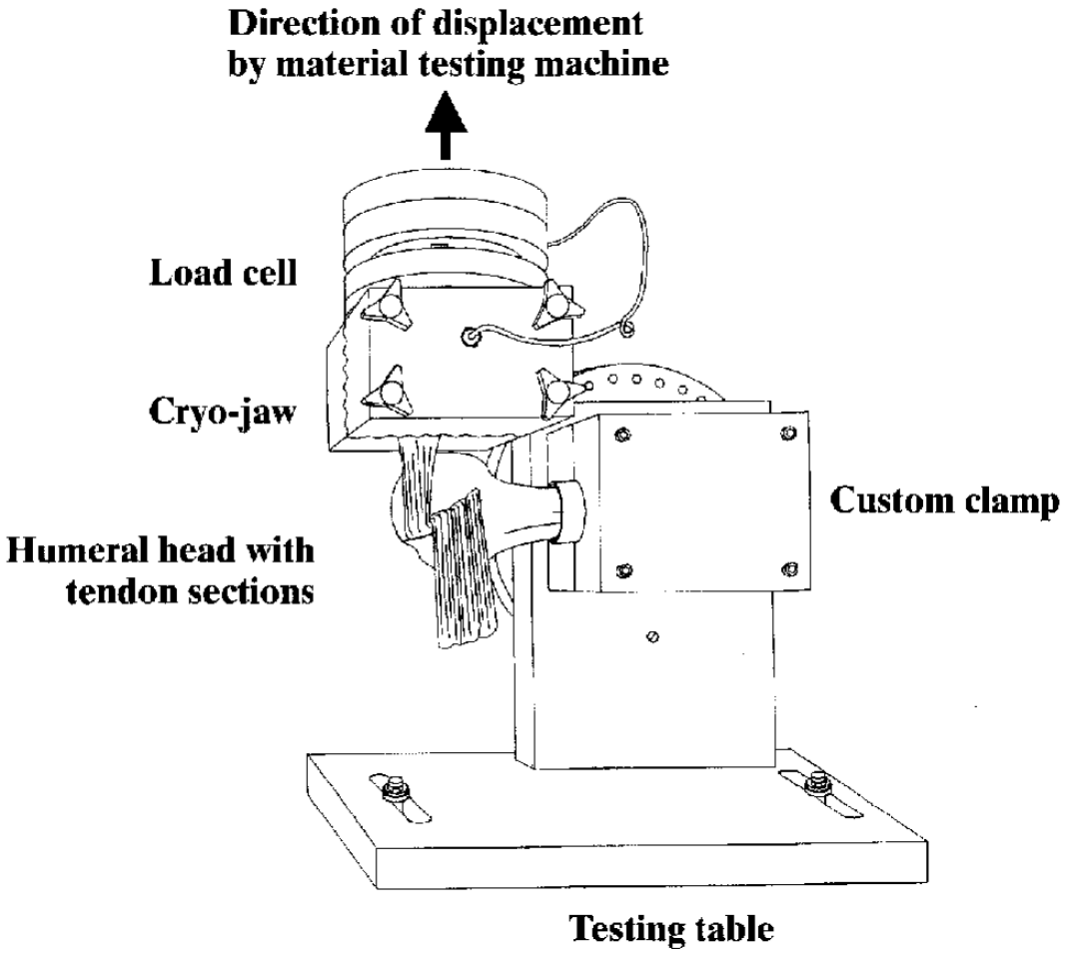

Figure 9: Physical testing setup for measuring stiffness of subscapularis, infraspinatus, and tere minor tendons [93, 94].

There are several limitations to this testing, which render it unusable as a source for FE soft tissue representation. First, the testing of the tendons was completed over a very small time period with a destructive load. For viscoelastic tissues such as tendon, the loading rate is very important to determining its stiffness. This loading rate and magnitude are far too fast to be comparable to the physiologic loading performed in the FE model. In addition, for the subscapularis tendon, no elastic modulus values were published. As only stiffness values (force/displacement) were presented, it is impossible to use these values without some simplifying assumptions. Finally, all displacement data were captured using the linear variable differential transducer (LVDT). This can be a very accurate method of quantifying strain if the stiffness of the tissue is much less stiff than the testing construct itself. However, the cantilevered nature of the humeral bone is likely to deflect as the tendon stretches. By measuring strain using only the LVDT, the elastic modulus of the tissue could be artificially low. A stiffness analysis of the construct could help verify their results.

As this is the most complete characterization of the elastic modulus and stiffness values of human subscapularis and infraspinatus tendon tissues available in the literature, more testing must be performed. In our testing, we measured the stiffness of these tissues using video techniques.

CHAPTER 2: THE EFFECT OF GLENOID COMPONENT VERSION AND HUMERAL POLYETHYLENE LINER ROTATION ON SUBLUXATION AND IMPINGEMENT IN REVERSE SHOULDER ARTHROPLASTY

Introduction

The indications for reverse shoulder arthroplasty (RSA) have expanded over the past decade. Originally intended only for an older, less demanding population suffering from cuff tear arthropathy [9, 15, 20, 24], clinical successes in restoring arm abduction and elevation function have provided confidence to expand RSA indications to proximal humeral fractures, deficient bone with intact cuff, cancer, as well as many others [7, 8, 20, 95, 96]. In 2007, shoulder arthroplasty was found to be growing at the same or higher rate as knee and hip arthroplasty [97], and recently RSA was found to account for 42% of total shoulder arthroplasties [34].

Unfortunately, RSA has also been associated with high complication rates [8, 37, 41, 55, 57, 95, 96, 98], with the two most common complications being scapular notching and instability [37, 99]. Scapular notching is a phenomenon in which the inferior aspect of the glenoid is eroded, and the inferior rim of the humeral polyethylene liner is severely worn. Scapular notching is thought to occur due to direct impingement between the humeral polyethylene and glenoid bone. While concerning, scapular notching can be monitored and assessed over time radiographically and is commonly only a cause for revision when the glenoid erosion jeopardizes the glenosphere fixation or distorted polyethylene geometry produces instability [18, 37, 41, 43, 49, 96]. Prosthetic instability leading to dislocation is the most common complication, reported as 38% of all complications following RSA [41]. In addition, instability can be difficult to effectively

address, with Chalmers et al reporting only 44% of early dislocations remaining stable following revision surgery and Frankle et al reporting nearly identical outcomes with closed reduction and revision surgery [31, 35, 41, 56].

Several new RSA implants have been introduced with specific design features intended to combat these common complications. One of the new design features is an asymmetrical humeral polyethylene liner, a departure from the original Grammont style design [7]. These polyethylene liner geometries vary between designs, but many feature thicker inferior regions and thinner superior regions. These changes in polyethylene liner design are thought to reduce the likelihood of scapular notching by lateralizing the humerus and increasing the impingement-free range of motion (ROM).

The influence of these design features on abduction/adduction ROM has been studied [100], but there has been little investigation of how this design change affects impingement-free ROM in other motions, especially those where direct contact of the humeral polyethylene liner on the inferior glenoid is likely. Furthermore, with the introduction of these asymmetrical designs, a new surgical variable, humeral polyethylene liner rotation, has been introduced. This variable is vital to study for two reasons. First, literature provided by medical device companies implies that neutral polyethylene liner rotation is ideal for all patients and motions. However, this may not be the case, and tradeoffs may need to be made to ensure that impingement or dislocation does not occur due to individual patient anatomy or motion differences. Secondly, if there is an ideal liner rotation, the effect associated with not setting the rotation precisely at that position must be determined.

Building upon our previous finite element (FE) analyses of RSA [58, 101], the goal of this study was to determine the effect of humeral polyethylene liner rotation on impingement-free ROM and the subluxation that would be generated after impingement during humeral external/internal rotation (ER/IR) and extension/flexion. The influence of glenoid component version on impingement-free ROM and subluxation was also studied. We hypothesized that neutral glenoid component version and neutral polyethylene liner rotation would produce the largest arc of motion prior to impingement and the smallest amount of subluxation/instability.

Materials and Methods

A previously validated finite element (FE) modeling approach for studying lateralization in RSA was used in the current study [58, 101]. Briefly, the surface geometries of the scapula and the humerus were generated from segmentations of the female cadaver of the Visible Human Project. Bone segmentations were performed with OsiriX DICOM viewing software (Pixmeo, Geneva, Switzerland) using an Intuos pen tablet/display (Wacom Technology Corporation, Vancouver, WA). Computer models of the 36 mm Aequalis Ascend Reverse Flex implant system were provided by Tornier (Wright Tornier, Memphis, TN).

Hexahedral finite element meshes were created in TrueGrid 3.1.3 (XYZ, Pleasant Hill, CA) consisting of a 15 mm section of glenoid bone, the glenosphere, the humerus implanted with a humeral implant at 0° version relative to the bone, and the polyethylene liner insert. To minimize computational time, the substantially stiffer metallic glenosphere and humeral stem were modeled as rigid. Bone and polyethylene elements were modeled as deformable, with linearly elastic material properties assigned [58, 101].

In addition, two springs were placed symmetrically about the joint center to replicate the soft tissue tension of the reconstructed capsule [58, 101]. Finally, a series of slipring connector elements with passive deltoid muscle stiffness values were modeled to represent the deltoid as a cable and pulley system [102, 103]. All FE analyses were completed using Abaqus/Explicit 6.14-2 (Dassault Systèmes, Vèlizy-Villacoublay Cedex, France).

From this baseline FE model, additional models with parametrically varied glenoid component version and polyethylene liner rotation within the humeral component were created. The glenoid version was defined by first creating a transverse plane oriented normal to the superior/inferior axis. The plane was placed through the center of the glenoid, measured as the distance halfway between the most inferior and superior points on the glenoid face (Figure 10).

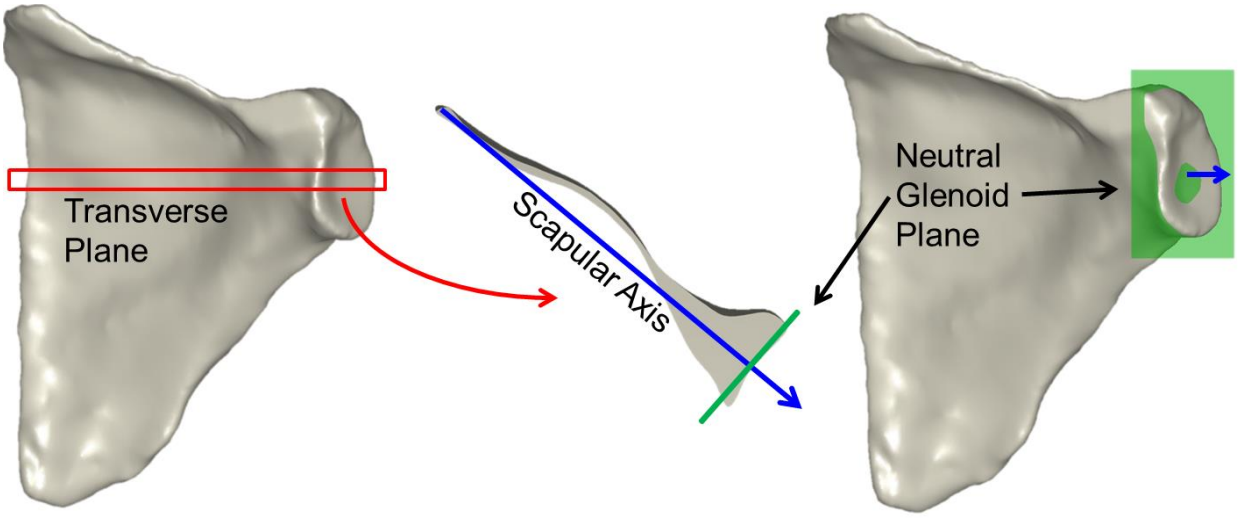

Figure 10: Definition of the neutral glenoid plane. A transverse section of the scapula was created through the middle of the glenoid. A scapular axis was created by drawing a line on the transverse plane from the most medial section of the scapula to the middle of the glenoid. The plane normal to the scapular axis was defined to be the neutral glenoid plane.

On this transverse plane, a scapular axis was defined from the most medial scapular bone to the center of the glenoid [104, 105]. The plane normal to this scapular axis at the very base of the glenoid fossa was defined as the neutral plane. Finally, the most inferior and most superior bony points lying on this cut plane were connected to define the glenoid version axis. Using Geomagic Studio Software (3D Systems, Rock Hill, SC) to manipulate surface geometries, glenosphere placement on the neutral plane was performed under supervision of a fellowship-trained shoulder surgeon (CMH) following manufacturer-recommended guidelines. To create FE models with various amounts of glenoid version, the cutting plane was rotated in 5° increments about the glenoid version axis. The humeral polyethylene liner rotation was varied by rotating the superior aspect of the polyethylene liner anterior or posterior within the humeral stem tray. For this study, five different glenoid version (5° anteversion, neutral, 5° retroversion, 10° retroversion, 20° retroversion) and five different humeral polyethylene liner rotation (20° anterior, 10° anterior, neutral, 10° posterior, 20° posterior) models were created (Figure 11).

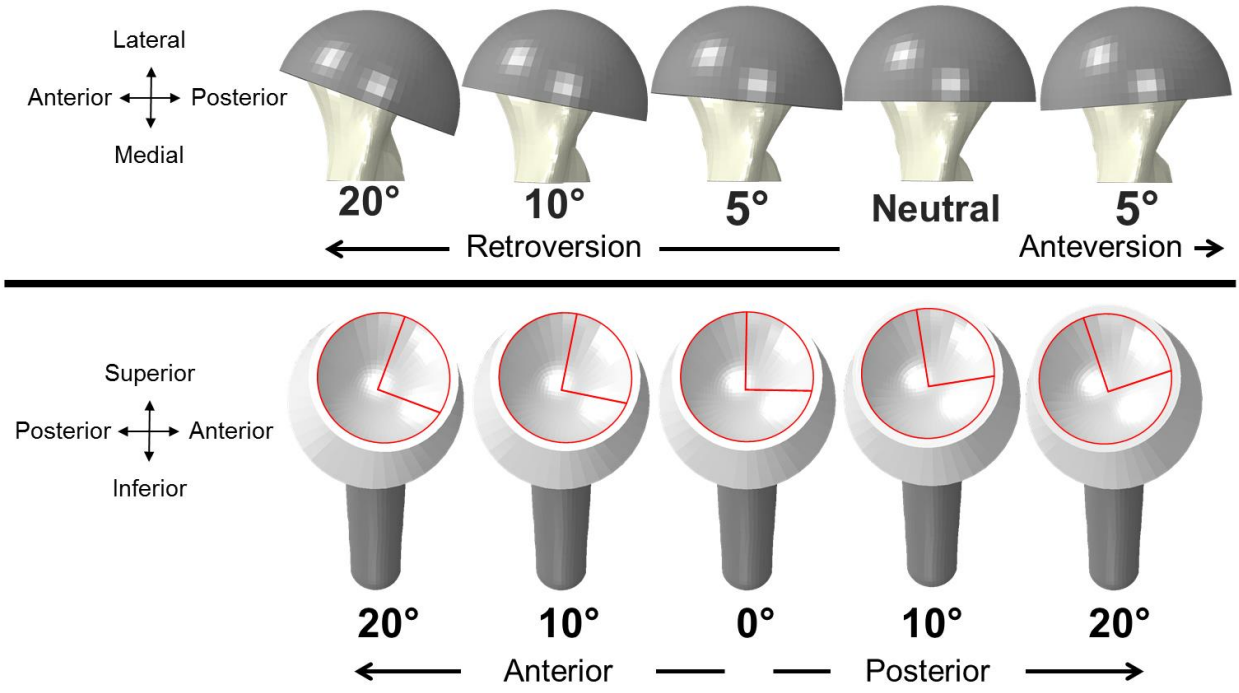

Figure 11: Five models of glenoid version and polyethylene rotation were created for study of ER/IR and Extension/Flexion. Shown above are inferior views of the glenoid models and shown below are medial views of the polyethylene models.

Humeral extension/flexion and external/internal rotation (ER/IR) motions were modeled to determine the risk of subluxation during different functional arm movements first for a series of ten models: all five glenoid component version models paired with a neutral humeral liner rotation and all five humeral liner rotations paired with a neutral glenoid version. These motions all began with the humerus abducted 20° and neutrally rotated. First, a load comparable to the weight of the arm (40 N) was applied to the distal region of the stem, and the deltoid cable was held fixed to prevent inferior subluxation [58]. The ER/IR motion then consisted of external rotation about the humeral axis to 45° of external rotation followed by internal rotation past neutral to 45° of internal rotation. The extension/flexion motion started with extension of 60° followed by flexion past neutral to 30° of flexion, with 35° of prescribed abduction during flexion to replicate arm

swinging. The soft tissues about the joint were assumed to be appropriately tensioned to investigate how otherwise well-tensioned RSA joints sublux when there is impingement between the polyethylene component and the inferior glenoid. Subluxation was quantified by the distance measured between the centers of rotation of the humeral polyethylene liner and the glenosphere (Figure 12). Additional rotation beyond the onset of impingement produced sequentially greater subluxation. The angles at which each motion first produced impingement were recorded. Impingement was defined as the angle at which greater than 0.5 mm of subluxation occurred.

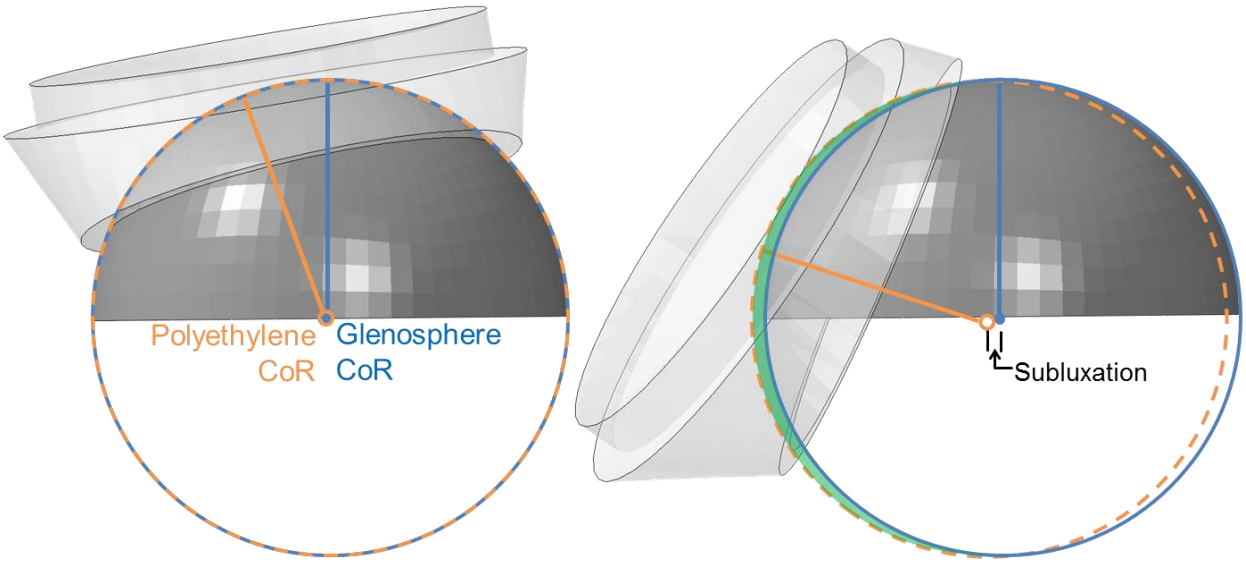

Figure 12: Depiction of fully seated (left) and subluxed (right) humeral components. Subluxation was defined as the distance between the glenosphere and humeral centers of rotation.

The initial results of the modeled extension/flexion and ER/IR motions indicated that the ER/IR motion was associated with much greater subluxation than the extension/flexion motion for any given implant position. To further assess the effects of implant position, a more extensive parametric study was performed modelling only ER/IR motion for an additional thirty-five different combinations of implant positions. Each of the five glenoid version models noted earlier (5° anteversion, neutral, 5°

retroversion, 10° retroversion, 20° retroversion) were paired with seven different humeral insert rotation models: 20° anterior, 10° anterior, neutral, 10° posterior, 20° posterior, 30° posterior, 40° posterior. Again, the maximum subluxation and the angle at impingement were recorded.

Two additional scapular specimen geometries [101] were modeled during ER/IR in order to verify whether or not the effects of changes in polyethylene liner rotation and glenoid component version varied with scapular geometry. Eight models were generated and tested for each additional scapular geometry: neutral glenoid component version paired with five amounts of humeral insert rotation (20° anterior, 10° anterior, neutral, 10° posterior, 20° posterior) and three glenoid component version models (5° anteversion, 5° retroversion, 10° retroversion) paired with a neutral humeral insert.

Results from the initial testing with clinically expected glenoid/liner combinations indicated that polyethylene inserts rotated posteriorly produced less subluxation and those rotated anteriorly produced more subluxation. In order to determine the extent of these effects (i.e. the point at which inserts rotated posteriorly might produce more subluxation), a greater range of humeral insert rotations were studied. Twelve models were created by pairing twelve humeral insert rotations (0°, 30°, 60°, 90°, 120°, 150°, 180°, 210°, 240°, 270°, 300°, and 330°) with a neutral glenoid component version. All models underwent ER/IR motion, and maximum subluxation and impingement angle were recorded.

Results

Impingement and subluxation were produced during both the extension/flexion motion as well as the external/internal rotation motion (Figure 13). However, external/internal rotation was found to impinge earlier in the motion (18±5 degrees vs. 32±10 degrees, p=.003) and to generate greater subluxation (6.1±1.1 mm vs. 0.8±0.3 mm, p<.001) than extension/flexion. Impingement and subluxation occurred primarily during extension and external rotation due to the coupled abduction that occurs during flexion.

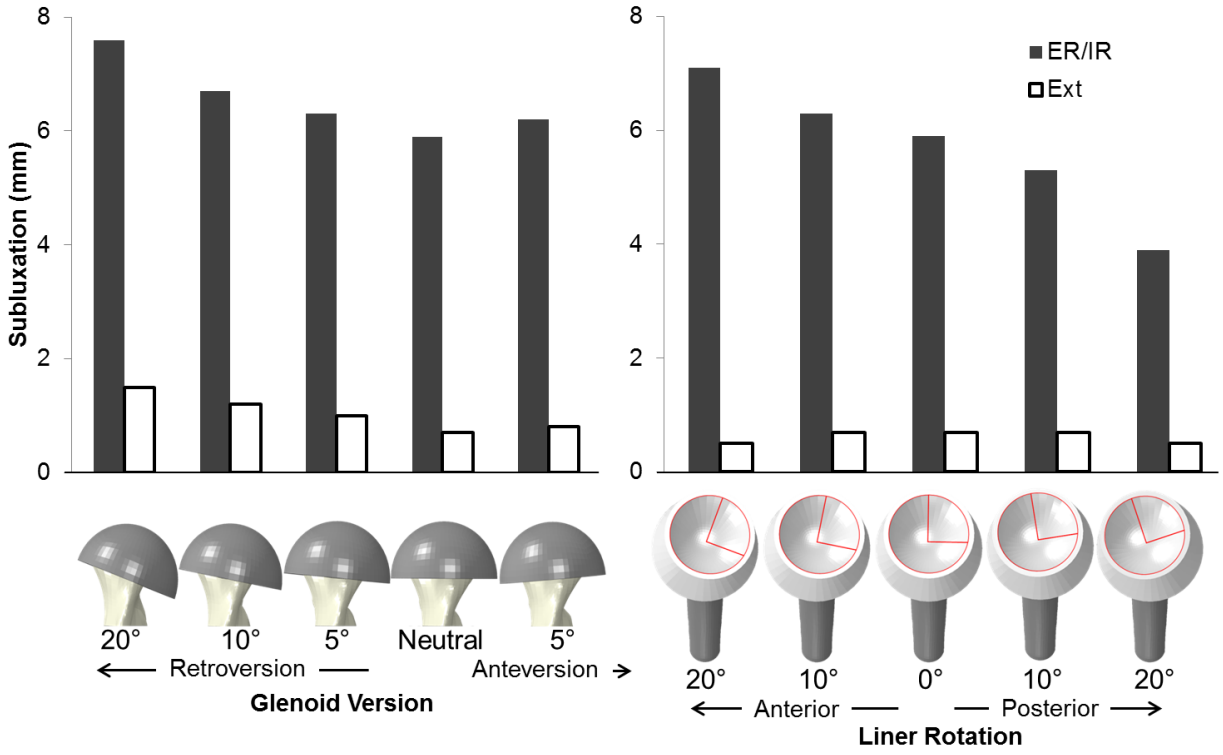

Figure 13: Maximum subluxation for models going through extension (gray) and external rotation (white) motions. All glenoid version models were run with a 0° humeral polyethylene insert, and all polyethylene rotation models were run with a neutral glenoid version. The ER/IR motion created much greater subluxation than the extension motion.

Neutral glenoid component version produced the greatest impingement-free range of motion regardless of polyethylene insert rotation and the least amount of subluxation in all but 30° posterior liner rotation (Figure 14). Progressively larger deviation from neutral glenoid component version caused progressively smaller impingement-free ranges of motion. Retroverted 5° and anteverted 5° models produced identical impingement-free ranges of motion for all humeral polyethylene insert rotations, and nearly identical subluxation (<0.3mm difference) for each specific humeral polyethylene insert rotation. The average deviations in impingement-free range of motion from neutral values across all polyethylene liner rotations were significantly different when comparing retroverted 20° and retroverted 10° model values (9±1 degrees vs. 4±0 degrees, $p<.001$), retroverted 10° and retroverted 5° model values (4±0 degrees vs. 2±0 degrees, $p<.001$), and retroverted 20° and retroverted 5° values (9±1 degrees vs. 2±0 degrees, $p<.001$) model values.

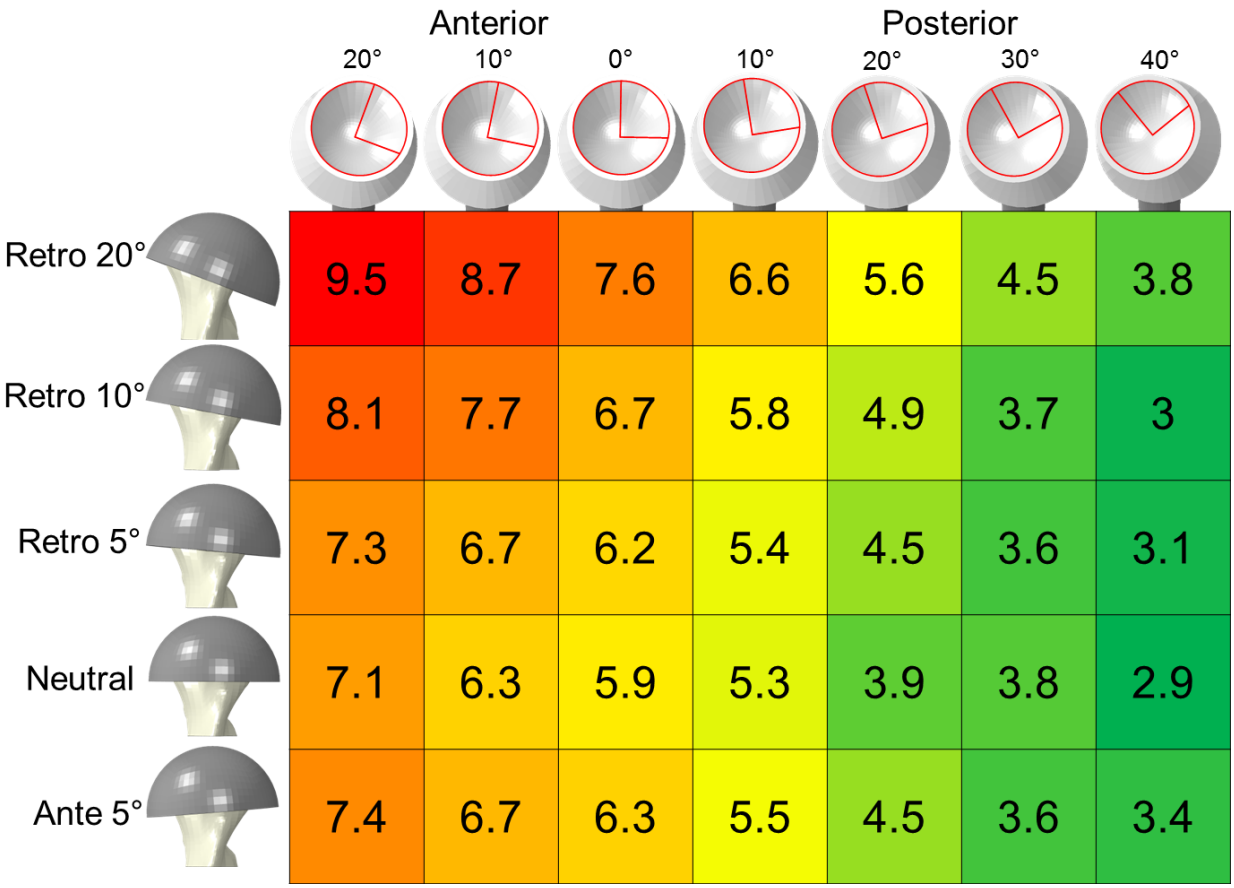

Figure 14: Maximum subluxation measured (mm) for each model during the ER/IR motion. All subluxation presented during external rotation.

In contrast, increased posterior rotation of the humeral polyethylene insert produced greater impingement-free ranges of motion as well as smaller subluxations. Humeral polyethylene inserts rotated posteriorly 40° produced the least amount of subluxation and the greatest impingement-free range of motion, and those rotated anteriorly 20° produced the greatest amount of subluxation and the smallest impingement-free range of motion (Figure 14). These trends in glenoid version and polyethylene insert rotation were the same in the additional two shoulder specimens that were modeled (Figure 15).

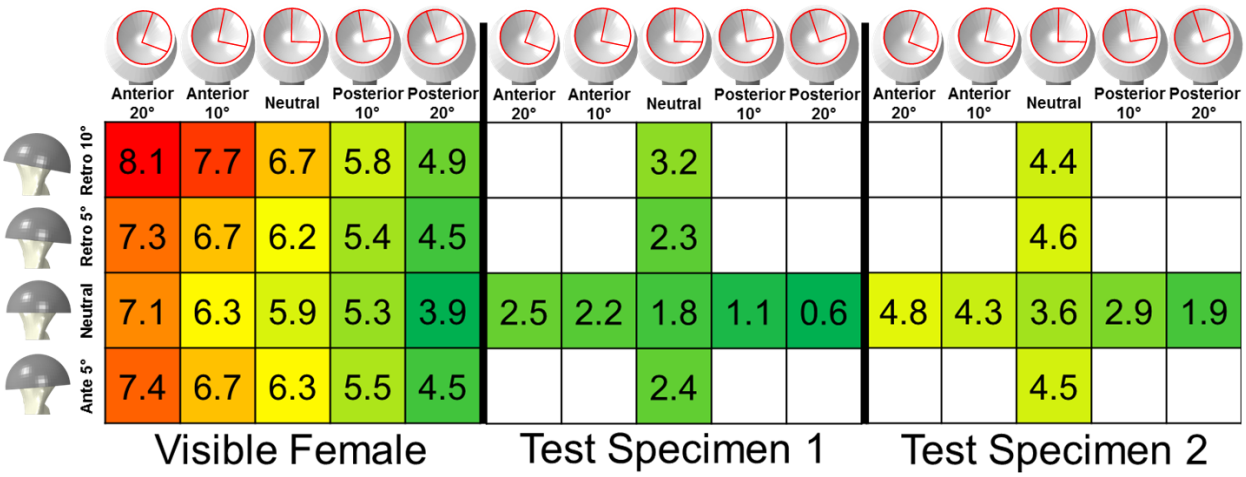

Figure 15: Maximum subluxation measured (mm) for two additional test specimens compared to the Visible Female results.

The 90° and 120° insert rotation models did not impinge during the motion modeled. In general, humeral insert rotations that placed the thickest portion inferiorly and posteriorly created earlier impingement and greater subluxation than rotations that placed it anterior and superior (Figure 16). These results signify that a polyethylene insert with the superior edge rotated posteriorly a given amount will experience less impingement than the same component rotated anteriorly by the same amount.

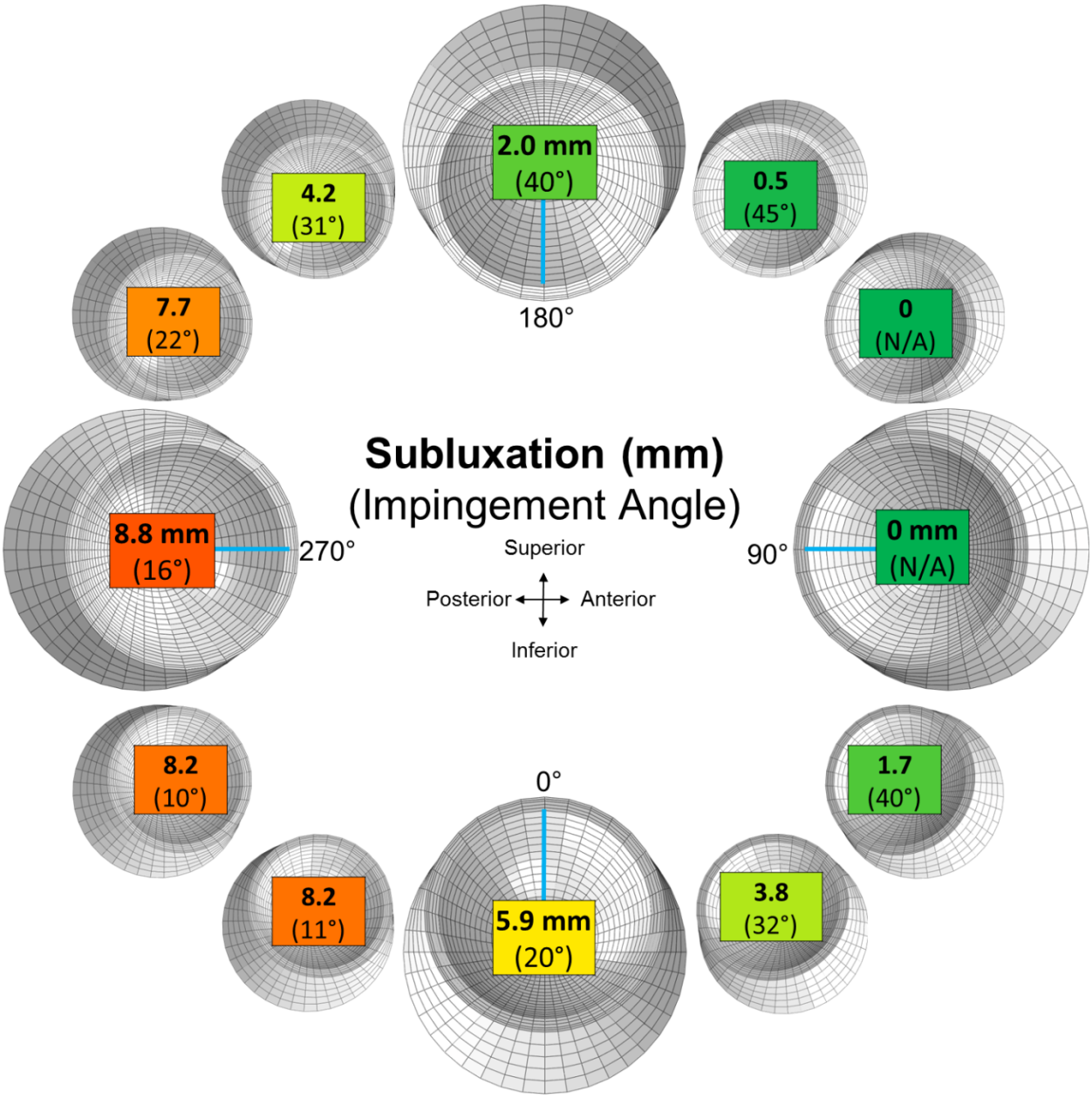

Figure 16: Subluxation (mm) and impingement angle for twelve humeral insert rotations. The current manufacturer-recommended humeral insert rotation is 0°.

Discussion

Glenoid component version and humeral polyethylene insert rotation were varied for the Tornier Ascend Flex system to determine their influence on subluxation. Impingement-free range of motion and subluxation were studied in external/internal rotation and extension/flexion motions. ER/IR was found to generate much greater subluxation than extension/flexion. Neutral glenoid component version was found to generate the least subluxation, and the greater the deviation from neutral version, the greater the subluxation. Polyethylene insert rotations which placed the thickest portion of the polyethylene in alignment with the inferior border of the scapula generated impingement earliest in the ER/IR motion and the greatest amount of subluxation. Likewise, rotations which positioned the thinnest portion of the polyethylene in alignment with the inferior border of the scapula (90° posterior in this system) generated no impingement and no subluxation for the motions studied. Glenoid component version is a variable that is not routinely addressed in RSA, except in cases of severe bone loss. However, our results indicate that an effort to correct the glenoid back to neutral scapular version can be beneficial for decreasing impingement. This correction could be achieved by reaming, bone grafting using tapered grafts with the BIO-RSA technique [96], or using custom implants.

Humeral polyethylene insert rotation is a challenging variable to measure clinically, and changes of less than 10° can be difficult to assess. Unfortunately, the modeling results indicate that even small changes in polyethylene insert rotation during implantation can create large differences in impingement angle and the amount of subluxation. The worst humeral polyethylene insert rotations in terms of impingement

angle and amount of subluxation were 300° and 270° (rotating the poly 60°-90° anteriorly from neutral) impinging at 16° and 10° of ER and producing 8.8 and 8.2 mm of subluxation, respectively. These rotations align the thickest part of the polyethylene with the inferior border of the scapula, causing the humeral component to impinge and sublux early in the ER motion. Following this logic, implantations in which the thinnest portion of the poly is aligned with the inferior border of the scapula would produce the least amount of subluxation and impingement much later in the ER motion. The modeling results support this claim, as the 90° and 120° models (rotating the poly 90°-120° degrees posteriorly from neutral) did not impinge during the 45° of ER and therefore created no subluxation. These results underline the importance of identifying humeral polyethylene rotation in RSA.

Corroborating our findings, Lewicki et al. recently reported that 45% of their RSA retrievals showed visually evident wear in the posterior-inferior region for the Zimmer RSA design, another radially asymmetrical insert design [106]. The wear pattern described in that work is similar to the patterns of elevated contact stress associated with impingement seen in our model for ER/IR motion (Figure 17).

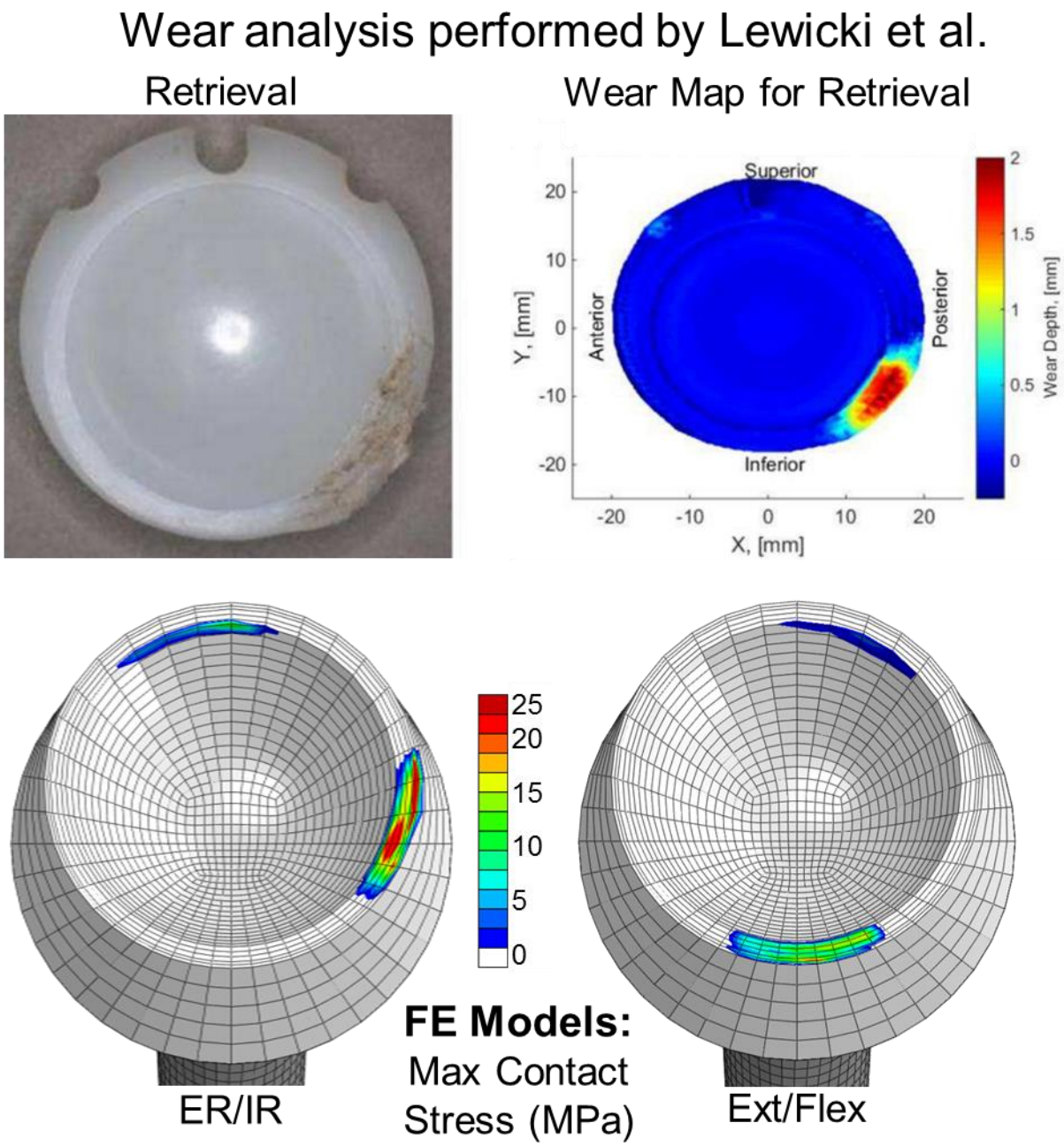

Figure 17: Example retrieval of a polyethylene component from the Zimmer RSA system and wear map taken from Lewicki et al. compared to the FE model calculation of the maximum contact stress generated for the entirety of both motion profiles for this study. The location of the highest contact stress for ER/IR corresponds well with the wear location presented in the physical testing referenced [106].

There are several limitations to this study. First, these results were generated using only one implant geometry, and the specific polyethylene insert rotations minimizing subluxation for this implant may not produce the least subluxation when applied to other implant systems with asymmetrical humeral polyethylene inserts. However, caution is advised when setting polyethylene insert rotation in RSA, as our results suggest that changes in rotation, regardless of system, can drastically alter mechanics. Another limitation to this work was the simple approach used to model the soft tissue restraints about the shoulder. The inclusion of different soft tissue properties and/or more complex material modeling could alter the amounts of subluxation calculated by the models. However, subluxation correlated well to impingement angle, an output dependent on bony geometry and independent of soft tissue tension. Because of this, we can assume that although subluxation may be dependent on soft tissue tension, impingement angle is not; it is only controlled by the geometry of the bone and polyethylene and the motion of interest.

Conclusion

In conclusion, impingement between the humeral polyethylene insert and the inferior glenoid bone during external rotation produces subluxation. Posterior rotation of an asymmetrical polyethylene insert reduces subluxation by increasing impingement-free range of motion, while anterior rotation increases subluxation. When placing an asymmetrical polyethylene insert, it is best to place it such that the thick inferior portion is rotated away from the scapula. However, other issues of joint stability related to soft tissue tensioning and the varying thickness of the polyethylene insert must also be considered when positioning the polyethylene insert.

CHAPTER 3: REVERSE SHOULDER ARTHROPLASTY-RELEVANT ROTATOR CUFF TENDON MATERIAL PROPERTIES CALCULATED USING VIDEO-BASED STRAIN MEASURES

Introduction

Over the past decade, reverse shoulder arthroplasty (RSA) has become a common treatment for those suffering from cuff-tear arthropathy [15, 20, 24], a disease categorized by both osteoarthritis of the glenohumeral joint as well as a massive rotator cuff tear. RSA restores glenohumeral joint stability by reversing the native anatomy of the joint, replacing the convex humeral head with a metallic humeral stem containing a concave polyethylene liner and replacing the native glenoid cavity with a convex metallic glenosphere [7]. RSA is effective in simultaneously relieving joint pain and returning functionality to patients previously unable to elevate their arm [7, 10, 95]. RSA has also been increasingly used to treat younger patient populations presenting with rotator cuff tears in the absence of arthritis, as well as individuals with shoulder pathology unrelated to glenohumeral arthritis, including proximal humeral fractures, deficient bone stock with an intact rotator cuff, and cancer [7, 8, 20, 95, 96].

Unfortunately, this reversed implant design has also been associated with high complication rates[8, 37, 41, 55, 57, 95, 96, 107]. The two most common complications are scapular notching and instability leading to dislocation [37, 97]. Scapular notching is a phenomenon in which frequent prolonged contact between the polyethylene liner and the inferior scapular wing causes bone loss at this site and macroscopic wear of the polyethylene liner. Instability is thought to occur due to poor or imbalanced soft tissue tensioning across the joint leading to dislocation [41].

Previous finite element studies have indicated that surgical decisions about implant orientation can substantially affect the risk of these two complications [58, 59]. However, in that previous work, extremely simple representations of the soft tissue capsule (i.e. nonlinear springs) were utilized. Although such definitions are easier to implement and require less computational run time, such assumptions do not accurately represent the *in vivo* situation in which the remaining rotator cuff tendons from the subscapularis, infraspinatus, and teres minor wrap around the joint. This wrapping would likely provide a buttressing effect, thereby affecting the risk of dislocation. In addition, not all RSA patients have identical rotator cuff deficiencies, and the presence or absence of any combination of these tissues could differentially contribute to instability and scapular notching.

In order to develop FE models incorporating accurate representations of these tissues which are important to stability in RSA, material properties from physical testing must be incorporated. Unfortunately, the overwhelming majority of reported rotator cuff tissue testing focuses on the supraspinatus tendon [86, 88, 89, 92], which is absent in RSA patients. Furthermore, the limited literature describing mechanical tests of the other rotator cuff tissues that are present in RSA patients does not provide adequate data from which to produce material models [93, 94]. In addition, those previous studies directly measured strain from the servohydraulic testing machine. This approach can produce inaccurate elastic moduli values for these tissues if the stiffness of the testing construct is not orders of magnitude higher than the tissue being tested. To isolate the data to only the tissue of interest, some groups have used video-based methods to measure strain during physical testing of the supraspinatus tendon [87, 108]. This method allows for tissue

displacement and strain tracking in a non-contact manner independent of testing fixture geometry or stiffness.

In order to determine accurate material properties of the subscapularis, infraspinatus, and teres minor tendons and to produce elastic moduli values of the rotator cuff tendons present in RSA patients, we performed physical measurements of tissue behavior under load and used video strain measurement techniques. We hypothesized that elastic modulus values for these tissues currently reported in the literature are artificially low due to reliance on tissue displacement values obtained by a servohydrualic testing machine.

Methods

Three fresh frozen cadaveric upper extremity specimens were analyzed (2 female, 1 male; ages 59, 49, and 56 years; BMI 26, 15, and 30; cause of death cardiogenic shock, lung cancer, and ALS respectively). Each specimen consisted of a full scapula and full humerus, including all overlying soft tissues. Each specimen was thawed at room temperature for 24 hours prior to an MRI scan using an Axial PD Cube sequence (slice thickness=.4 mm, in-plane resolution=.3 mm, TE=25.596 ms, TR=1500 ms) in a 3T GE Discovery 750W MRI Scanner (GE Healthcare, Chicago). 12 hours after the MRI scan, a fellowship-trained shoulder surgeon excised all non-rotator cuff soft tissue from the specimen. The supraspinatus was also removed as presence of the supraspinatus is a contraindication for RSA. The origins of the subscapularis, infraspinatus and teres minor were released from the scapula, and the muscle tissue was removed from the rotator cuff tendons. The humeral head with the rotator cuff tendons was wrapped in saline-soaked gauze to prevent dehydration. The distal humerus was transected 13 cm distal to the

lesser humeral tuberosity, and the remaining distal-most humerus was potted in a cylindrical block of poly-methyl methacrylate (PMMA) bone cement. The subscapularis and infraspinatus tendons, due to their size, were sectioned into two halves to ensure uniform tensioning across the section. The teres minor was left intact (Figure 18).

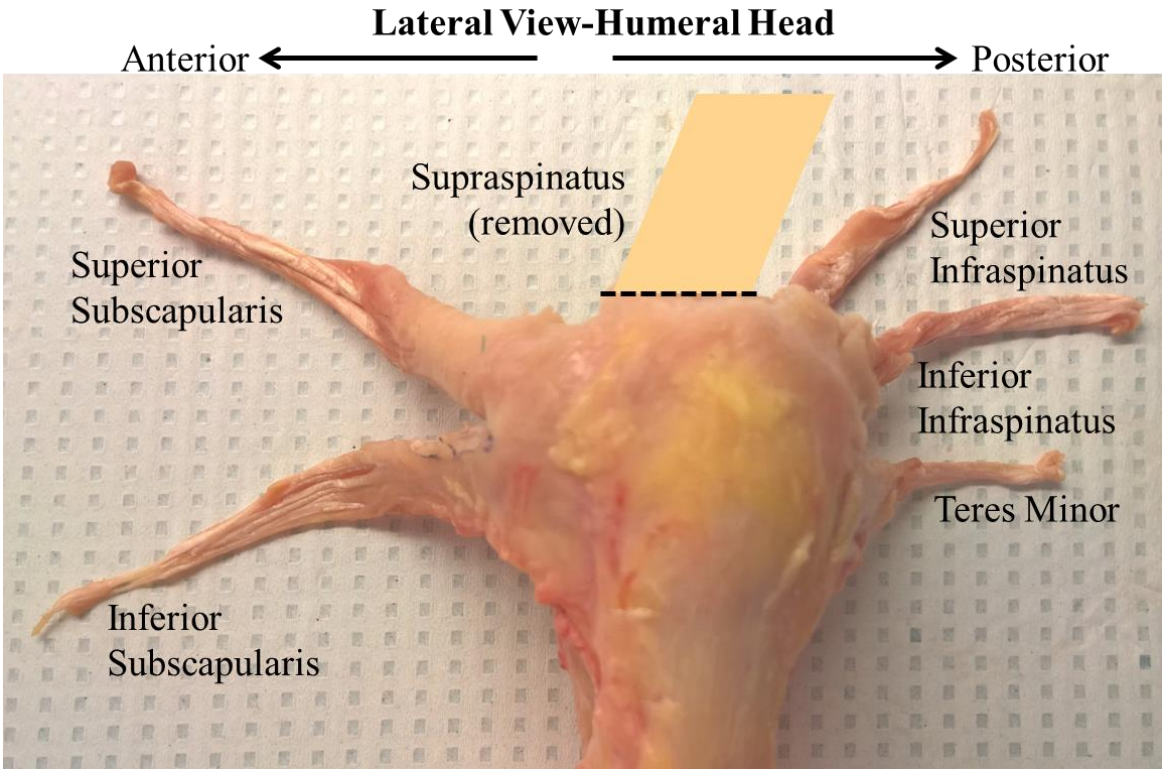

Figure 18: Lateral view of humeral head following tendon sectioning. The subscapularis and infraspinatus were divided lengthwise into equal section while also respecting existing fiber geometry.

The cross sectional area of each tendon section was measured. For the first specimen, the tendon was clamped in the testing setup, placed under a 10 N load, and the width and thickness at the mid-substance were measured using a digital caliper. These measurements were repeated three times and averaged. The tendon dimensions were used to calculate an elliptical cross sectional tissue area. Unfortunately, the design of the testing clamp made manual caliper measurement of the tendon cross sectional area

difficult, as the serpentine clamp and humeral head obstructed perpendicular caliper measurement of the thickness of the tissue. Therefore, a more robust measurement method using a custom device was implemented for the second and third specimens. Using the assumption of incompressibility, the tendon was constrained into a rectangular slot created by a 0.5 mm resolution ruler and a 10 mm t-ruler until firm resistance was met. The superior-inferior width of the tendon was measured to the nearest half mm using the device, and the thickness of the tendon was measured by using a digital caliper to measure the height of the slot to the nearest tenth of a millimeter. This measurement was repeated three times for each tendon section, the area was calculated as the product of the two dimensions, and the average tissue cross-sectional area was computed for each specimen.

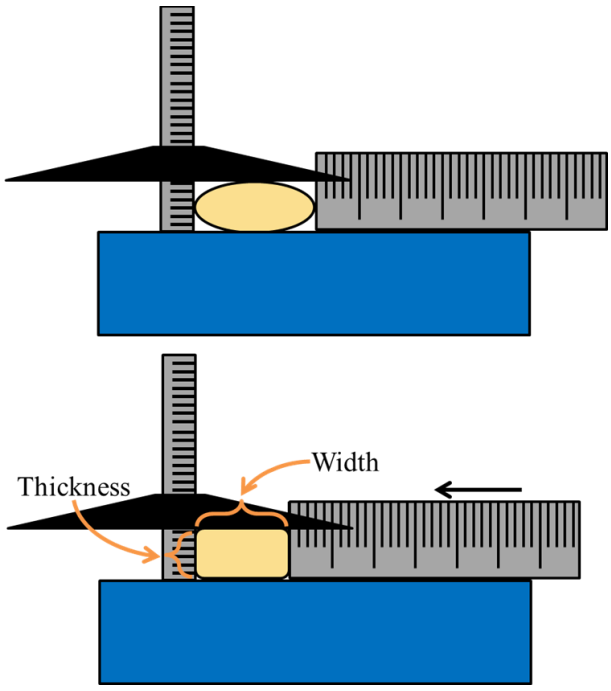

Figure 19: Cross sectional area measurement schematic and image. The tissue was constrained into a slot created by two measurement devices until firm resistance was met due to incompressibility of the tissue. The thickness of the tissue was measured using a digital caliper to measure the height of the slot, and the width was measured to the nearest half millimeter with a ruler.

After measuring tissue cross-sectional area, the specimen was placed into a custom designed testing fixture (Figure 20) attached to a servohydraulic testing system (MTS Bionix 858; MTS Systems Corporation, Eden Prairie, MN). The fixture held the long axis of the humerus horizontally, perpendicular to the direction of the cross head displacement. The rotation about the long axis of the humerus was set such that there was at least 5 mm of tendon wrapping around the humeral head to make the direction of the pull more anatomically accurate along the axis of the tendon, while preventing peeling of the tendon away from the bony insertion. The humeral fixture was mounted on an X-Y table to permit humeral displacement in all directions perpendicular to the direction of tendon pull and preventing loading that was not aligned with the axis of the tendon.

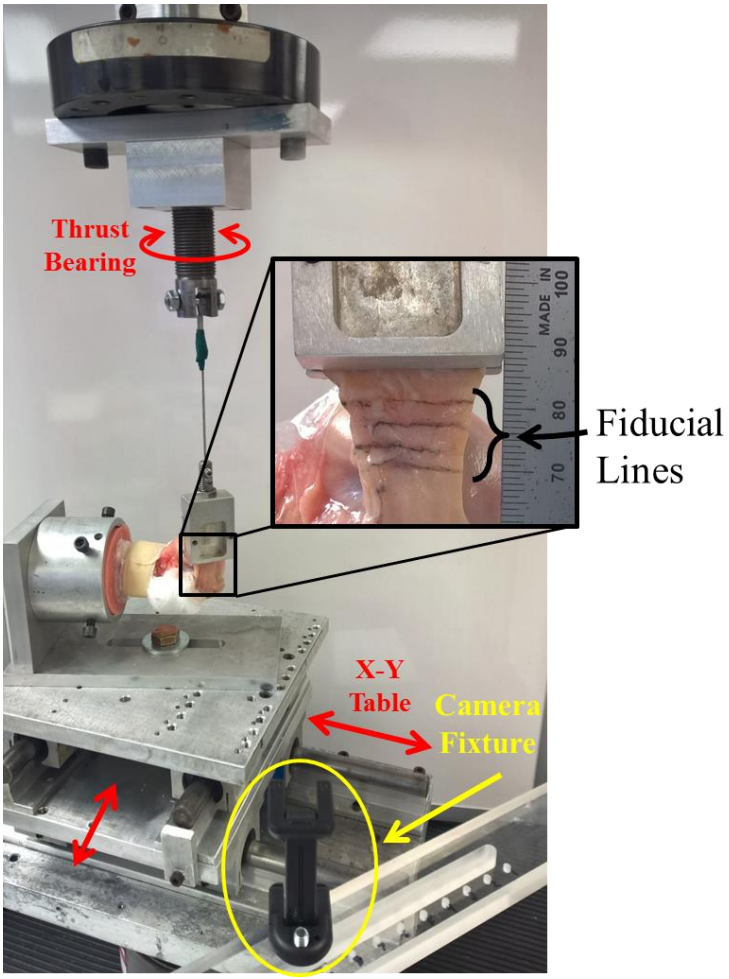

Figure 20: Image of testing setup. The specimen was free to translate in all direction perpendicular to the direction of the tensile tendon load. In addition, the tendon was free to rotate about the tensile load direction. The camera was rigidly attached to the testing device through the use of a camera fixture.

For testing, each individual tendon section was isolated and the medial end was placed into a serpentine clamp to minimize tendon slippage during loading. The remaining tendon sections remained sealed in plastic cling wrap and saline-soaked gauze to prevent dehydration. The serpentine clamp was attached by a braided cable to the displacement head through a thrust bearing, allowing free rotation of the tendon about the axis of displacement. Under displacement control, a 10 N tensile load was applied to remove tendon slack. For the placement of fiducial lines on the tissue, the tendon section

was patted dry using gauze. Black India ink was applied to a strand of suture, and the ink-coated suture strand was run horizontally across the tendon section in several locations, creating a series of parallel fiducial lines on the tissue surface. The load was then removed, and the tendon was rehydrated for testing using saline spray.

All tests were performed in load control while video was recorded at 1080p (1920x1080), 30 fps, using a Nokia Lumia 929 camera phone with Carl Zeiss optics (Microsoft Corporation, Redmond, WA) mounted for stability using a custom built acrylic fixture rigidly attached to the MTS. First, 20 N of preload was applied. The tendon sections were tested with a ramp load of 30 N/s applied for 10 seconds (300 N applied). Tests were repeated for a total of three replicate tests, with less than 2 minutes occurring between tests. During load application, an observer verbally called out the tensile loads applied by the MTS in 50 N intervals. A custom, semi-automated Matlab (MathWorks, Natick, MA) program was developed to measure video-based tissue displacement and strain for comparison with the values obtained from the MTS. The program read in the video and audio from each test and the corresponding MTS-measured values. The audio of the test video was filtered to remove noise produced by the testing machine, and peak analysis was performed to determine the times at which the load call-outs were performed. The audio clips corresponding to these peaks were played for the program user to identify the load called out. The times and loads achieved at these times were recorded. The video frames were then analyzed between the first and last loads using two different methods to determine which method most reliably identified the fiducial lines.

First, manual chosen points were used to automatically crop each image into regions containing only one fiducial line. The first method used a thresholding algorithm to identify the fiducial line in each region by first removing the blue channel from the image to increase the relative darkness of the black lines compared to the tissue. Using a pixel intensity histogram, the darkest 20% of pixels were identified, and the centroid of these pixels was computed. This process was performed for each fiducial line of every frame.

In the second method, a Dijkstra's method algorithm identified the least "costly" path across the image in each region, starting at the left and progressing to the right. The pixel intensity values represented the cost of each pixel; in this way, darker pixels were less costly, and lighter pixels were more costly[109, 110]. The centroid of the Dijkstra's path for each fiducial line was calculated.

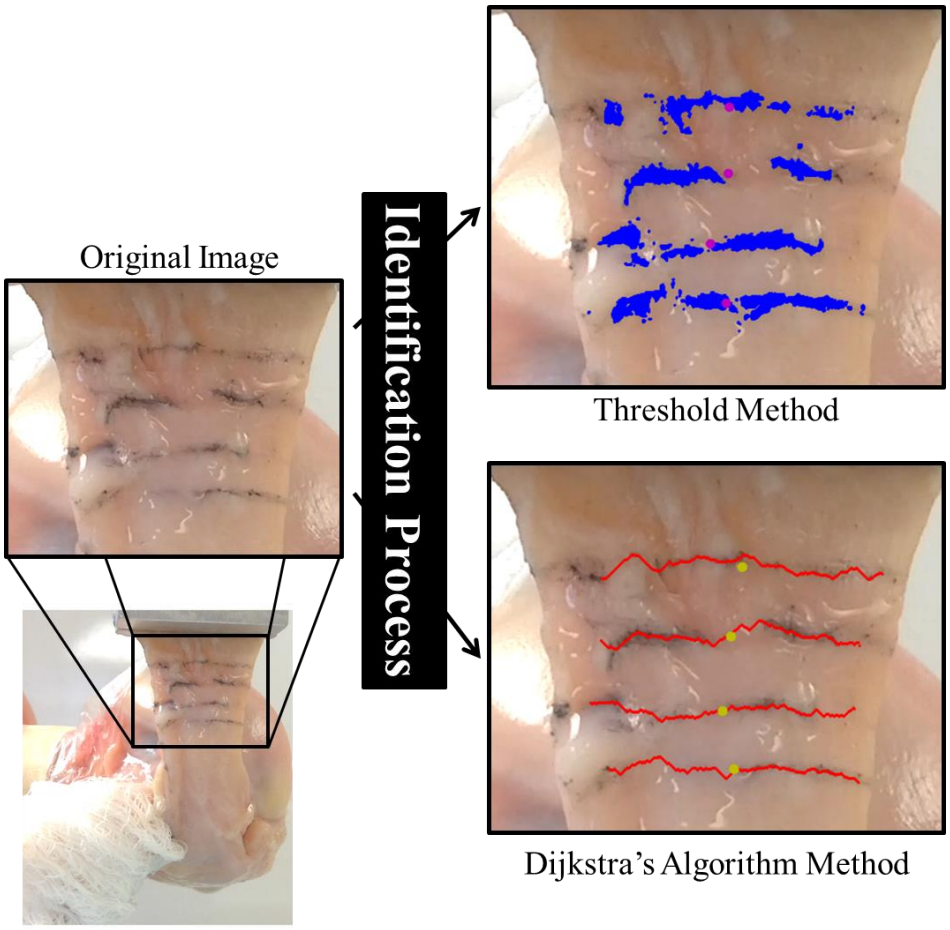

Figure 21: Overview of video analysis process. Two methods are used to identify the fiducial lines drawn across the tendon. All methods are then plotted on each frame of the test and reconverted into a video.

Each of the three methods was completed for each frame of each test video. Tissue strain was measured between the middle two fiducial lines and defined as the difference of the current length and initial length divided by the initial length. This region was chosen as it was least affected by the effects of the clamping and corresponded to the location at which the cross sectional area measurements were performed. The length was defined as the distance in pixels between the centroids of the middle two lines for each method, and the initial length was defined as the distance between centroids when the first load (20 N) was called out. The strain-time curves were plotted for each method (Figure 22).

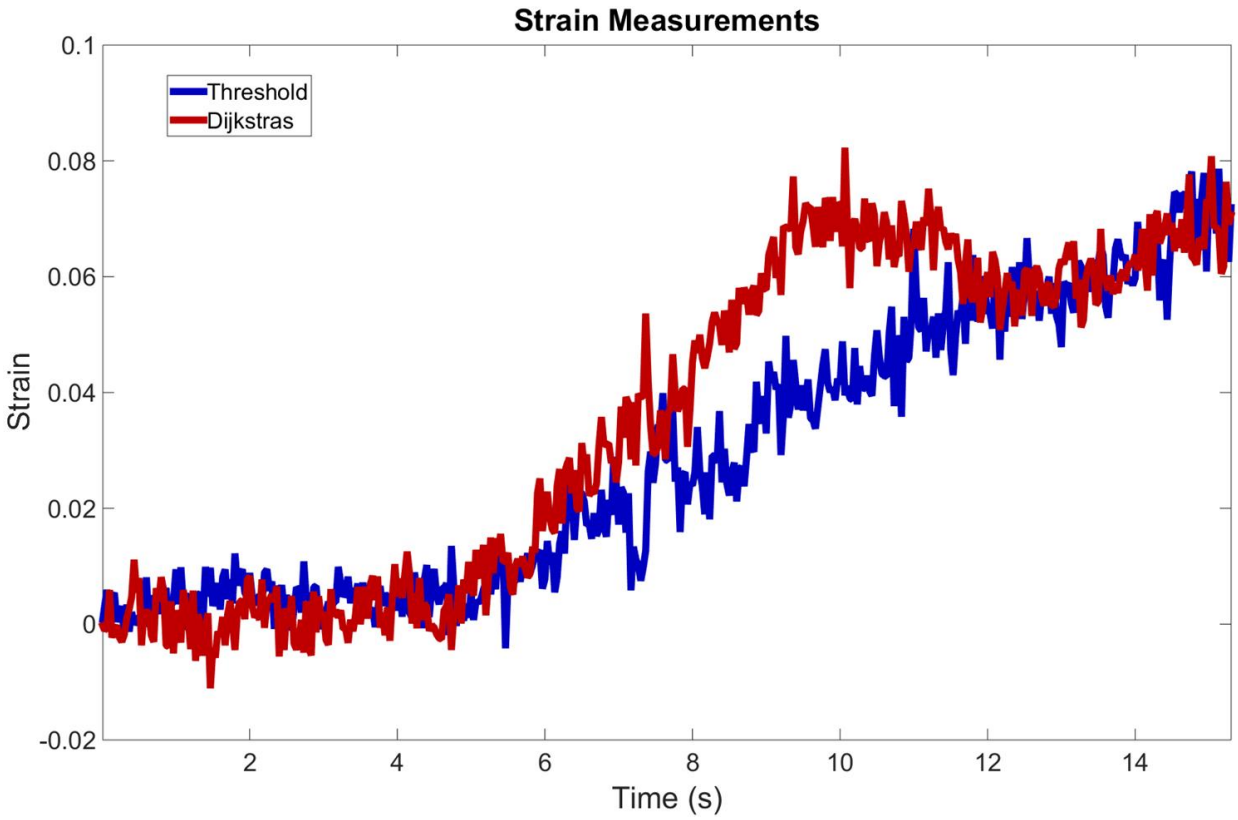

Figure 22: Representative strain vs. time diagram of the central region of a tendon section for each of the three different methods used. The relatively flat region in the beginning corresponds to the initial 20 N preload, and the increase in strain just before the 6 second mark corresponds to the start of load application.

The physical testing data was then incorporated. For comparison to the video-based data, the times at which the MTS device recorded a load within 0.5 N of the load called out in the video were identified. The differences between MTS and video load times were calculated to determine the amount of error in verbally calling out loads. Preliminary images of the undeformed tendon sections with a ruler for scale and displacements from the MTS data and were used to calculate MTS strain.

Load data were converted to stress values using the cross sectional area values computed previously. The Threshold and Dijkstra's method video strain measurements were compared to the MTS data strain measurements. Resulting stress strain plots were created (Figure 23), and elastic modulus values were calculated by fitting a line to the

data. One-way ANOVA and t-tests were used to assess differences in elastic modulus measured using both video methods compared to servohydraulic methods and differences in elastic modulus measured for specific regions of the rotator cuff using both video methods.

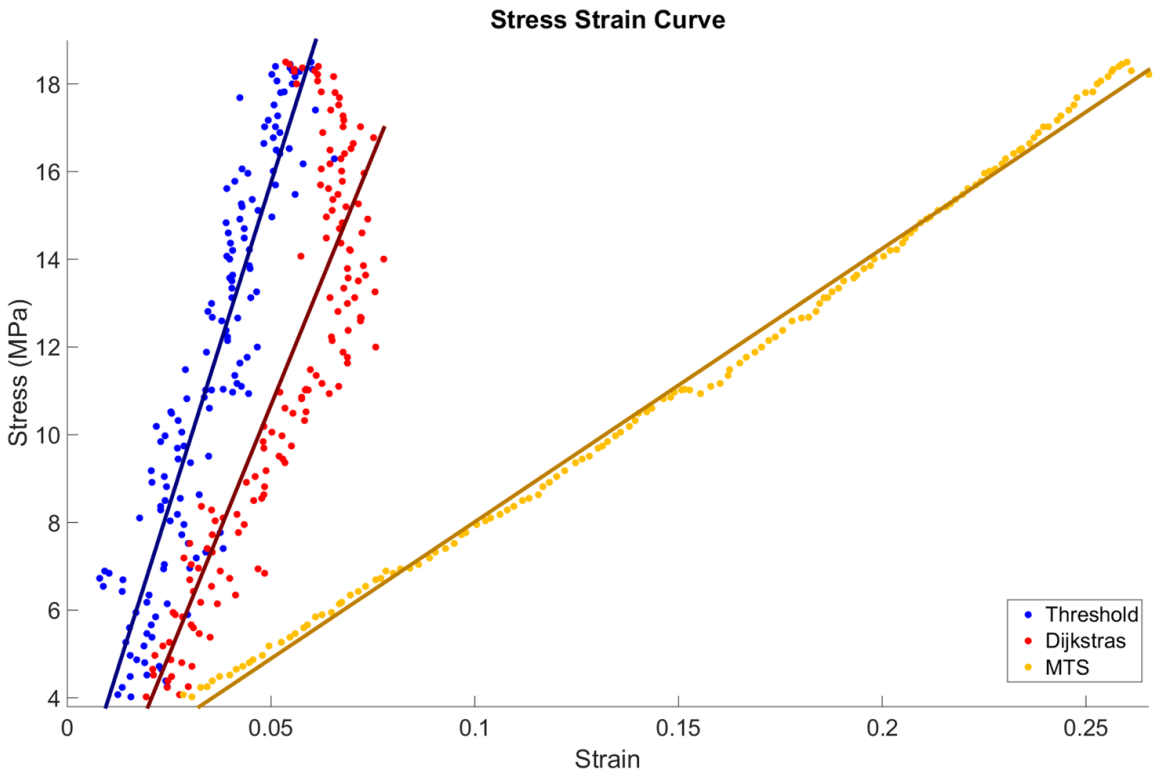

Figure 23: Stress vs. strain diagram for the teres minor tendon section of specimen 2. Preload stresses and strain are omitted, leaving only the stress and strain values recorded during the test. The higher strain and less stiff elastic moduli values were observed for the MTS values than the video strain measurements due to the compliance of the testing construct.

Results

Cross-sectional area measurements are shown in Table 1. There were differences in tendon cross section areas. Although equivalent dissection of the tendons was performed, care not to cut through fibers led to unequal widths between sections. In addition, differences in thickness between superior and inferior tendon sections also affected area calculations.

Table 1: Cross sectional area of tendon sections tested

	Area (mm^2)		
	Specimen 1	**Specimen 2**	**Specimen 3**
Superior Subscapularis	59.1	61.8	67.7
Inferior Subscapularis	86.1	26.9	74.3
Superior Infraspinatus	32.5	13.3	64.4
Inferior Infraspinatus	32.1	30.0	47.4
Teres Minor	25.7	7.9	35.9

Small errors were measured when comparing the time difference between loads measured by the video and MTS methods, verifying the accuracy of the load times determined from the video. The average time difference between successive loads as measured in the video versus the MTS data was -.03 seconds or 1.8% of the total time interval. The elastic modulus values derived using servohydraulic displacement strain were significantly lower than both video-based methods. However, there was no significant difference associated with the different video-based methods (Table 2).

Table 2: Comparison of elastic modulus values obtained using three methods across all tendon sections. The average elastic modulus for each specimen calculated using the Threshold, Dijkstra's, and MTS methods were analyzed, and the video methods were found to calculate much stiffer modulus values.

	Comparison of Measurement Methods					
	Threshold	MTS	Dijkstra's	MTS	Threshold	Dijkstra's
Specimen 1	245±204	52±11	185±88	52±11	245±204	185±88
	p=.007		**p<.001**		*p=0.357*	
Specimen 2	206±142	26±18	175±65	26±18	206±142	175±65
	p<.001		**p<.001**		*p=0.466*	
Specimen 3	73±44	13±2	88±59	13±2	73±44	88±59
	p<.001		**p<.001**		*p=0.447*	

The elastic moduli of the tissues tested are displayed in Figure 24 using both the Threshold and Dijkstra's method. A statistically significant difference in elastic modulus value was found between the Threshold and Dijkstra's algorithm methods in the inferior subscapularis section of specimen 3 (Threshold: 60 ± 8 vs. Dijkstra's: 41 ± 7 MPa, p=.039). However, no significant difference was found when comparing elastic modulus values calculated by both methods in all other tendon sections of all specimens (Table 3).

Table 3: Comparison of Threshold and Dijkstra's methods in calculating elastic modulus values measured in MPa for specimens 1, 2, and 3. The teres minor failed following the first testing in specimen 3, and the inferior subscapularis of specimen 1 failed during the initial testing.

Elastic Modulus Values (MPa)			
Specimen 1			
Section	**Threshold (Mean ± SD)**	**Dijkstra's (Mean ± SD)**	**p-value**
Superior Subscapularis	380 ± 327	270 ± 93	0.632
Superior Infraspinatus	327 ± 188	204 ± 36	0.382
Inferior Infraspinatus	68 ± 12	71 ± 2	0.671
Teres Minor	207 ± 15	193 ± 39	0.592
Specimen 2			
Section	**Threshold (Mean ± SD)**	**Dijkstra's (Mean ± SD)**	**p-value**
Superior Subscapularis	129 ± 61	137 ± 45	0.864
Inferior Subscapularis	180 ± 54	197 ± 42	0.695
Superior Infraspinatus	328 ± 208	230 ± 29	0.504
Inferior Infraspinatus	85 ± 11	94 ± 34	0.683
Teres Minor	361 ± 77	239 ± 9	0.269
Specimen 3			
Section	**Threshold (Mean ± SD)**	**Dijkstra's (Mean ± SD)**	**p-value**
Superior Subscapularis	128±41	116±12	0.686
Inferior Subscapularis	41±7	60±8	**.039**
Superior Infraspinatus	74±50	141±104	.385
Inferior Infraspinatus	57±23	51±7	.702
Teres Minor	45	44	N/A

Although there was no significant difference overall between the Dijkstra's and Threshold methods, the Dijkstra's method derived elastic modulus values produced smaller standard deviations. For this reason, only Dijkstra's method values are discussed and presented in the following results.

The superior infraspinatus of both specimens 1 and 2 exhibited statistically significant stiffer material properties than the inferior infraspinatus (Superior Infraspinatus: 227 ± 33 MPa vs. Inferior Infraspinatus: 83 ± 25 MPa, $p<.001$). The teres minor tendon was also stiffer than the inferior infraspinatus (Teres Minor: 211 ± 37 vs. Inferior Infraspinatus: 83 ± 25 MPa, $p<.001$). No statistically significant difference was found between the elastic moduli values of the superior infraspinatus and teres minor tendons (Superior Infraspinatus: 227 ± 33 vs. Teres Minor: 211 ±37 MPa, $p=.781$).

The anterior t produced less clear results. The inferior subscapularis section for specimen 1 failed early on the initial test and, as such, did not produce a meaningful elastic modulus measurement. As opposed to the posterior region, there were large, though not significant, differences between the elastic moduli values of specimen 1 and specimen 2 for the superior subscapularis (Specimen 1: 270 ± 93 MPa vs. Specimen 2: 137 ± 45 MPa, $p=.111$).

Finally, the elastic modulus values of the third specimen were significantly lower across both methods than the other two specimens, due to the diminished soft tissue quality found in late-stage ALS (Table 4). Elastic modulus values for the healthy tissues are shown in Table 5.

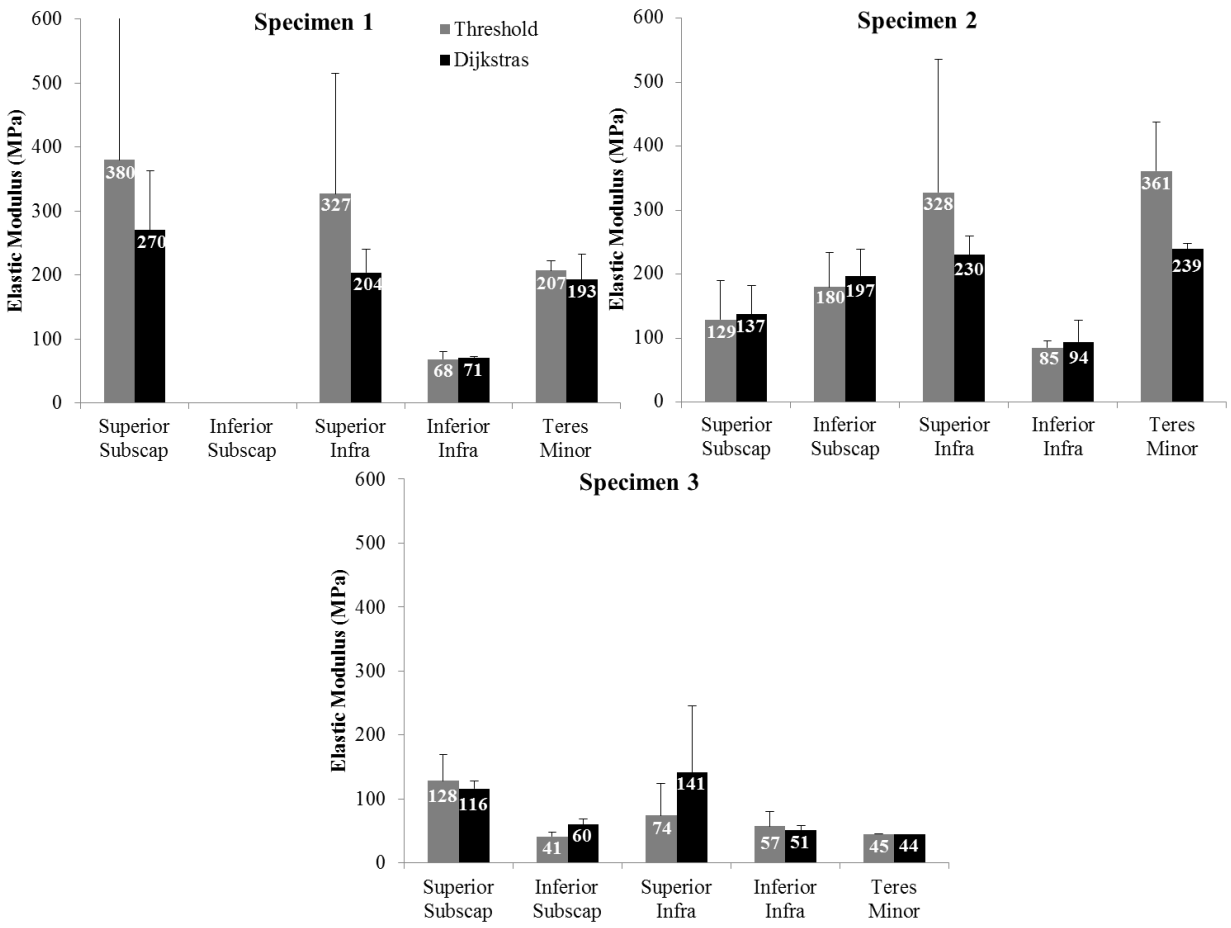

Figure 24: Elastic moduli values calculated for specimens 1, 2, and 3.

Table 4: Average elastic modulus values measured using the Dijkstra's method for each specimen across all tendon sections. Specimen 3 (ALS) was found to be significantly less stiff than the other two specimens.

	Comparison of Specimens					
	Specimen 1	Specimen 2	Specimen 2	Specimen 3	Specimen 1	Specimen 3
Elastic Modulus (MPa)	185±88	175±65	175±65	72±44	185±88	72±44
p-value	*p=.763*		**p<.001**		**p=.001**	

Table 5: Elastic modulus values calculated for the healthy specimens tested.

Elastic Modulus (MPa)	
Superior Subscapularis	204 ± 98
Inferior Subscapularis	197 ± 42
Superior Infraspinatus	217 ± 33
Inferior Infraspinatus	83 ± 25
Teres Minor	211 ± 37

Discussion

When tensioned appropriately, rotator cuff tendons are the primary tissues preventing instability after RSA. In this study, we aimed to determine elastic moduli and strain values for these tissues to inform a finite element model of RSA studying instability and scapular notching. In addition, we aimed to test our hypothesis that video strain measurements will compute significantly stiffer elastic modulus values than the limited MTS-derived elastic modulus values available in the literature.

As was hypothesized, the elastic modulus values for the healthy specimens (1 and 2) were stiffer than those previously reported in the literature that were derived using strain data generated by a servohydraulic testing machine across all tendon sections (current testing: 179 ± 75 vs. Halder et al.: 94 ± 39 MPa) [93, 94], and the teres minor was much stiffer than was previously reported (current testing: 211 ± 37 vs Halder et al.: 14 ± 9 MPa). Also, although collagen and soft tissue properties are diminished in subjects suffering from ALS [111], our methods were capable of detecting a decrease in soft tissue quality with this specimen. Furthermore, the average values across all tendon sections from the ALS specimen related most to values previously reported (current

testing: 88 ± 59 vs. Halder et al.: 94 ± 39 MPa), demonstrating the compliance of the previously published data.

In our results, the measurement of the elastic modulus using only MTS data would have severely underreported tissue stiffness values, supporting the use of video-based strain measurement for soft-tissue strain measurement. In this work, deflection of the humerus and deformation of the cable connection to the clamp were observed as the largest factors of construct movement. Although a stiffer construct could have diminished this effect, the use of video would still be necessary to ensure that the deflection is small relative to the displacement of the tissue and metal construct. If MTS data is to be taken at face value without video verification, a construct stiffness experiment must be performed in order to determine the base stiffness of the construct. In addition, the researchers must be certain that no slipping or sliding of tissue is occurring in the clamp.

Two methods were used to identify the fiducial lines. Although the Threshold method was less complex and rigorous than the Dijkstra's method, no statistically significant difference was observed between the measured elastic modulus values calculated by the two methods for all but one tendon section in one specimen, indicating that, although the Dijkstra's method most often created less variability in elastic moduli values, both methods are satisfactory in measuring this value.

Video resolution is very important in video strain measurements. Care was taken to fill the field of view with tissue, in order to enhance strain precision, while also capturing the lines during the entirety of the video. The vertical direction of the video contained 1080 pixels at every frame. On average, tendon sections consisted of approximately 80 pixels, creating just over 1% strain precision. Higher resolution video

recording methods (4K) could be used in future testing to enhance resolution and improve strain precision.

In conclusion, elastic moduli values for rotator cuff tendons present in RSA were quantified using video strain measurement techniques. Video methods of measuring strain calculated significantly stiffer elastic modulus values than servohydraulic methods, exhibiting the importance of video strain measurement techniques to verify data gathered during soft tissue testing. No significant difference in elastic modulus values were found between the video strain measurement methods. These methods were capable of measuring differences in tendon quality between relatively healthy and diminished soft tissue. We plan to use the stress-strain curves generated from these experiments to create finite element models studying instability and scapular notching in RSA.

CHAPTER 4: A FINITE ELEMENT MODELING APPROACH TO STUDYING INSTABILITY IN REVERSE SHOULDER ARTHROPLASTY

Introduction

Reverse shoulder arthroplasty (RSA) is an effective treatment for relieving pain and restoring function to individuals suffering from glenohumeral instability and arthritis secondary to rotator cuff deficiency [8]. RSA works to restore glenohumeral stability by reversing the natural anatomy of the joint – replacing the naturally concave glenoid cavity with a convex metallic glenosphere, and the naturally convex humeral head with a concave polyethylene liner. The RSA design moves the center of rotation medially and inferiorly from the humeral head to the center of the glenosphere, effectively restoring shoulder function [7, 8, 10, 95]. Built on this success, a large number of other surgical indications for RSA have been approved including proximal humeral fractures, revision from total shoulder arthroplasty or hemiarthroplasty, as well as cancer [7, 8, 27, 28, 30, 95, 112, 113].

However, RSA has suffered from high early to mid-term rates of complication [17, 30, 31, 33, 36, 37, 41, 81, 114]. The two most common complications are instability and scapular notching [37, 97]. Scapular notching is a phenomenon in which chronic contact between the inferior portion of the polyethylene liner and inferior neck of the glenoid causes bone loss at the impingement site, which can be seen radiographically, and macroscopic wear of the polyethylene liner. Instability is subluxation/dislocation of the humerus away from the glenosphere rotation center, thought to be caused primarily by an imbalance of the soft tissue tensioning across the joint [41]. Given the underlying

cuff deficiency in these patients, passive tissue tensioning likely plays a large role in joint stability.

In our prior work, we studied the effect of glenoid version and polyethylene rotation on risk of scapular notching and instability in RSA during humeral internal/external rotation. We did this by measuring impingement-free range of motion, contact stress developed once impingement occurred, and propensity for subluxation of the humerus away from the glenosphere when impingement occurred. The passive soft tissue tensions of the reconstructed capsule were modeled by an anterior and a posterior spring placed symmetrically about the joint center.

We found that impingement occurred only in external rotation, a result matching well with clinical studies linking patients with greater external rotation range of motion post-operatively to increased rates of scapular notching [42], as well as findings that limitations of internal rotation are likely not due to bony impingement [18, 23, 115]. In addition, our results indicated that the subscapularis is the primary structure limiting excessive subluxation and frank dislocation during external rotation. Clinically, these findings conflict with evidence showing equivalent complication rates and dislocation events for patients regardless of whether the subscapularis is repaired [114], but agree with other evidence that significantly more dislocations occur in patients with irreparable subscapularis tendons [116].

In summary, our prior findings suggest (1) that external rotation range of motion is linked to scapular notching risk and (2) subscapularis tendon tissue integrity influences the risk of subluxation leading to dislocation. However, the veracity of the second observation was limited by the complexity with which we modeled the passive stabilizing

soft tissues about the joint. Building upon the previously developed FE modeling approach [58, 59], we re-visited these hypotheses by explicitly modeling the stabilizing influence of the subscapularis and infraspinatus muscle groups. The subscapularis structural properties were varied, as were implant geometry parameters, to investigate contributions to RSA stability.

Methods

Axial PD Cube sequence MRI images were obtained of an intact cadaveric shoulder on a 3T GE Discovery 750W MRI Scanner (GE Healthcare, Chicago). The MRI images were segmented using Seg3D (CIBC, Salt Lake City, UT) to produce bone and tendon surfaces, as well as tendon insertion site data. Geometries segmented included the scapula, humerus, subscapularis, and infraspinatus tendons. The bone and tendon surfaces were then decimated and smoothed using Geomagic Studio (3DS, Rock Hill, SC).

Tornier Aequalis Ascend Flex Reverse implant hardware was placed within the bony geometry of the shoulder following manufacturer guidelines. This involved adjusting the humerus surface from an anatomic position into an RSA position (medial and inferior to anatomic) using Geomagic Studio. Fully hexahedral meshes were generated in TrueGrid (XYZ Scientific Applications, Livermore CA) for the scapula, glenosphere, humeral liner and tray, and subscapularis and infraspinatus tendons. All FE analyses were run in Abaqus/Explicit (Dassault Systemes, Vèlizy-Villacoublay, France).

All tendons were assigned Ogden hyperelastic material properties using the *data point input* option in Abaqus. Source stress and strain data were available from previously performed physical testing of the rotator cuff tendons (Chapter 3). The Abaqus hyperelastic *data point input* option accepts nominal stresses and strains as

inputs, and performs an optimization with these data to create the best fitting hyperelastic material model. Rather than importing data from every uniaxial tendon test, a series of best fit data curves were generated from complete stress-strain data for the tendons of interest from all tests. A best fit exponential model was found using Matlab built in functions. Seven different curves representing the variation in tendon stiffness properties were computed. Data from these curves were used to generate the hyperelastic material property definitions.

RSA surgery is most commonly performed using a deltopectoral approach [117]. In this approach, an incision is made between the deltoid and pectoralis major muscles, aiming to spare the deltoid from damage. The approach also involves making an incision through the subscapularis tendon, if present, near its humeral insertion site. After RSA implantation, if the subscapularis tendon is deemed to be of adequate quality, the tendon is reattached to the humeral insertion with sutures. During reattachment, because of the inferior and medial change in position of the humerus associated with RSA, the subscapularis tendon is stretched from its normal anatomy. To capture this effect in the FE model, the subscapularis tendon model was likewise adjusted from its native anatomy. First, the tendon surfaces were meshed in an undeformed, native state, and then displaced inferiorly and laterally in their entirety within the model along with the humerus (Figure 25). This served as the starting point for the finite element simulations.

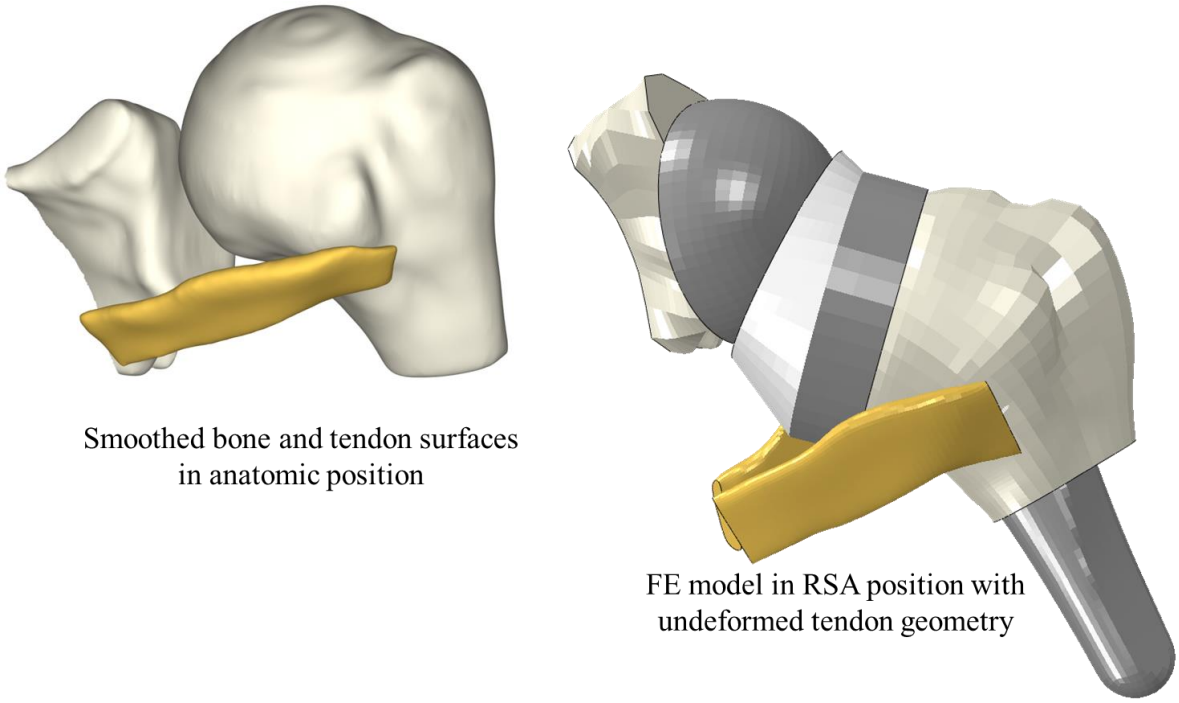

Figure 25: Original anatomic position of bone and tendon surfaces (left), with the RSA position of the meshed humerus and tendon in the undeformed state (right).

FE simulations consisted of three separate steps, the first two of which were used to tension the tendons while the position and rotation of the humerus was held fixed. In Step 1, the proximal free ends of the tendons were displaced toward their anatomic origins and 5 mm outward from the joint, to avoid any contact with bone or implant surfaces. In Step 2, the proximal ends of the tendons were displaced 5 mm towards the joint, with contact now enforced between all surfaces, effectively wrapping the tendons around the glenosphere, polyethylene liner, and humeral tray (Figure 26). During these two initial steps, the humeral insertion sites of the tendon were tied to the humeral rigid body using a rigid connector element. This attachment allowed realignment of the distal tendon with the axis of the proximal tendon during tensioning and wrapping.

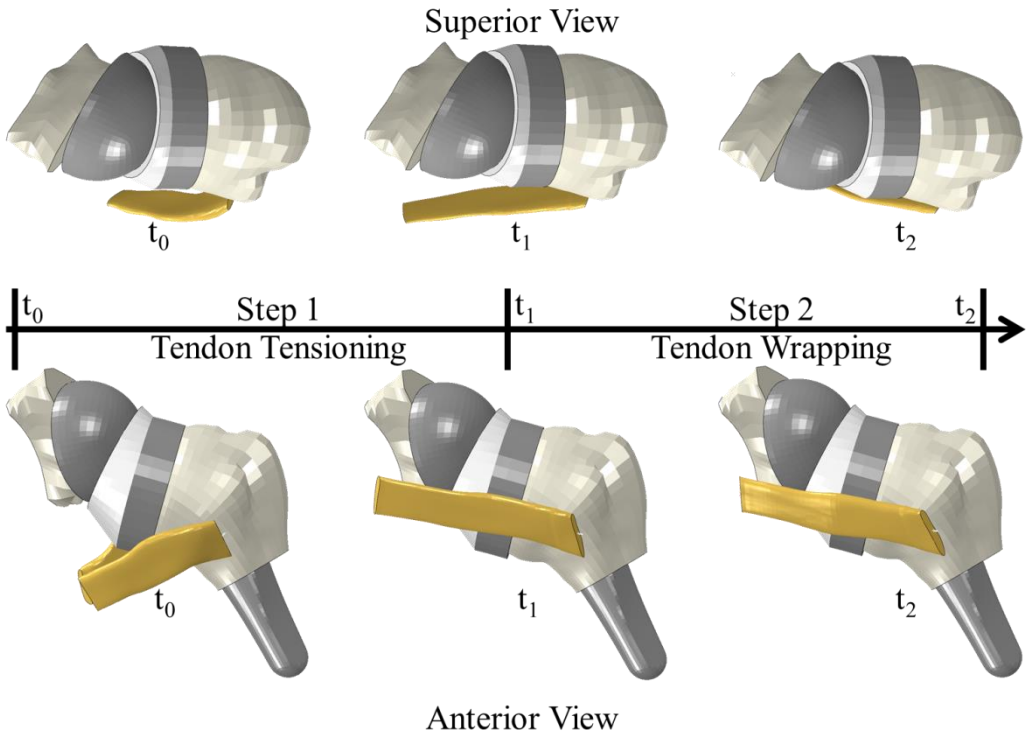

Figure 26: Anterior and superior views of the model during the tendon tensioning steps. The tendon starts in an RSA position with undeformed geometry. In Step 1, the proximal end of the tendon is stretched to its original anatomic location and 5 mm outward from the joint. During Step 2, the proximal end of the tendon is moved 5 mm toward the joint as it wraps across the implant geometry (i.e. as surface contact is invoked).

Proximal Cuff Tissue Restraints

During Step 3, the humerus was externally rotated about its long axis from neutral to 45° of external rotation. While the translations of the humerus were not explicitly constrained during this step, the tension and wrapping of the tendon tissues implicitly control the position of the humerus during rotation. The tendons are attached proximally to their respective rotator cuff muscle bellies, but the functional integrity of these muscles varies considerably among RSA patients. This presents ambiguity in modeling the proximal restraint of the tendons, so two different approaches were explored.

The first approach to modeling proximal cuff tissue restraints involved using explicitly defined boundary conditions (BCs). Three different combinations of proximal-end-tendon BCs were evaluated to represent the antagonistic eccentric contraction of the subscapularis expected during external rotation: (BC1) holding the proximal end of the tendon fixed in all translations, (BC2) fixing only the AP and superior/inferior (SI) translations while applying a 1000 N medially-directed load, and (BC3) applying a 1000 N load along the line of action of the tendon while allowing free translation. The subluxation of the humerus was measured for all three BC combinations, where subluxation was defined as the distance between the centers of rotation of the polyethylene liner and glenosphere.

The second approach to modeling proximal cuff tissue restraints involved placing a piecewise linear elastic spring at the proximal attachment point of the subscapularis, with the proximal end of the spring rigidly fixed in space. The spring stiffness was defined so that the tendon would never experience tensile forces greater than the tension present when wrapping (Step 2) was completed. Thus, during external rotation of the humerus, the proximal spring would extend to relieve increases in tension due to tendon lengthening, replicating an isotonic eccentric contraction of the subscapularis (Figure 27). Table 6 lists the tensile forces present in the seven subscapularis material models during external rotation.

Table 6: Table of constant tensile forces exerted on tendon models by nonlinear springs during external rotation.

Material Model	Purple	Navy	Blue	Teal	Green	Orange	Red
Force (N)	97	193	367	572	650	1084	3155

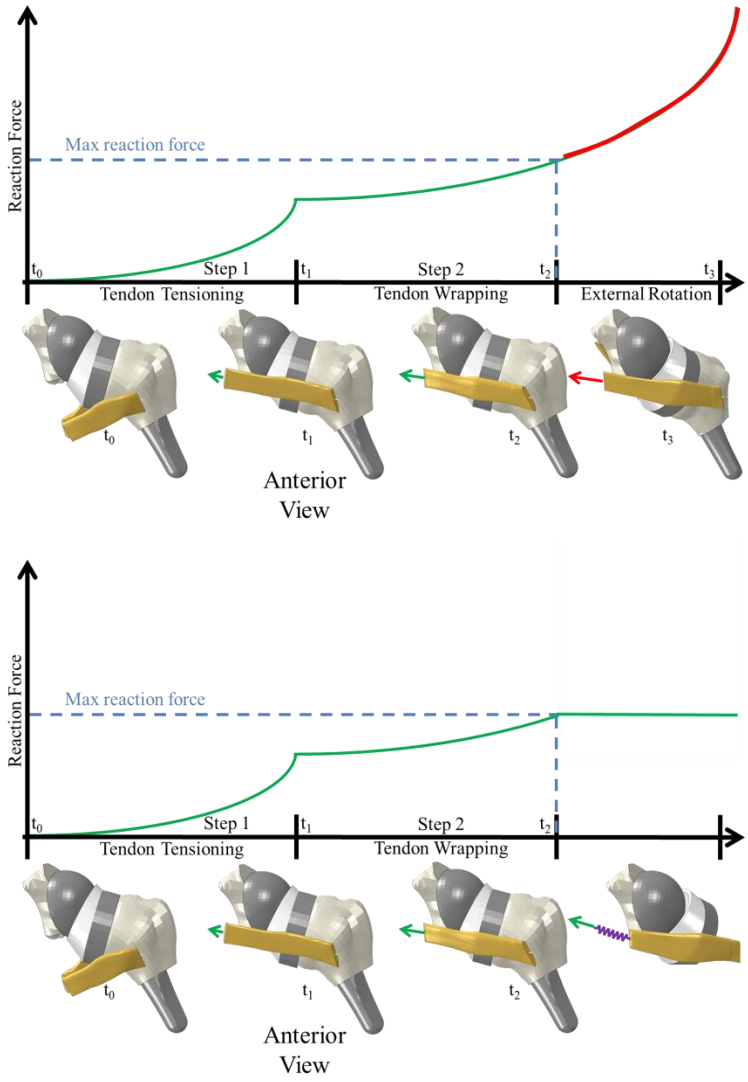

Figure 27: Subscapularis reaction force vs time plots comparing the fixed and spring boundary conditions. In the fixed boundary condition, force in the tendon increases throughout external rotation, while tensile force in the tendon remains fixed during external rotation for the spring boundary condition.

Variation of material model and polyethylene liner rotation

Seven different subscapularis material models were run with three different polyethylene liner rotations (posterior 30°, neutral, anterior 30°), creating 21 separate models. Higher resolution meshes of the polyethylene liner and tray were created for this study to obtain enhanced contact patch resolution when compared to the previous study. Also, the humeral bone and stem were removed from the model in order to reduce

computation time, as no contact occurred at these locations. The maximum amount of subluxation generated during Step 3 external rotation of the humerus was recorded, where subluxation is calculated as the distance between the centers of rotation of the glenosphere and polyethylene liner. In addition, the maximum contact stress experienced by the polyethelene liner over the external rotation motion was recorded.

Results

Proximal Cuff Tissue Restraints

For each of the three initial BC combinations, impingement was computed between the polyethylene liner and inferior glenoid bone. The primary impingement occurred at the same amount of external rotation for all cases. However, different behavior of the subscapularis tendon was observed for each, as well as different amounts of humeral subluxation. The least subluxation was computed for BC1 (2.99 mm), followed by for BC2 (3.67 mm), and the humerus subluxed the most for BC3 (4.93 mm).

The BC1 case created stable behavior of the tendon, and the tendon orientations stayed relatively fixed during the external rotation. However, excessive force (3123 N) was generated in the tendon, with associated high contact stresses (560 MPa) at the impingement site. In the BC2 case, the proximal end of the tendon translated only 8.8 mm laterally, with significantly less force developing in the AP (400 N) and SI (594 N) directions. Finally, the BC3 case displayed the most interesting result, as the tendon slid inferiorly under the humeral tray during external rotation (Figure 28). Comparison of the contact stresses experienced by the liner at the end of the external rotation arc for the three BC cases is shown in Figure 29.

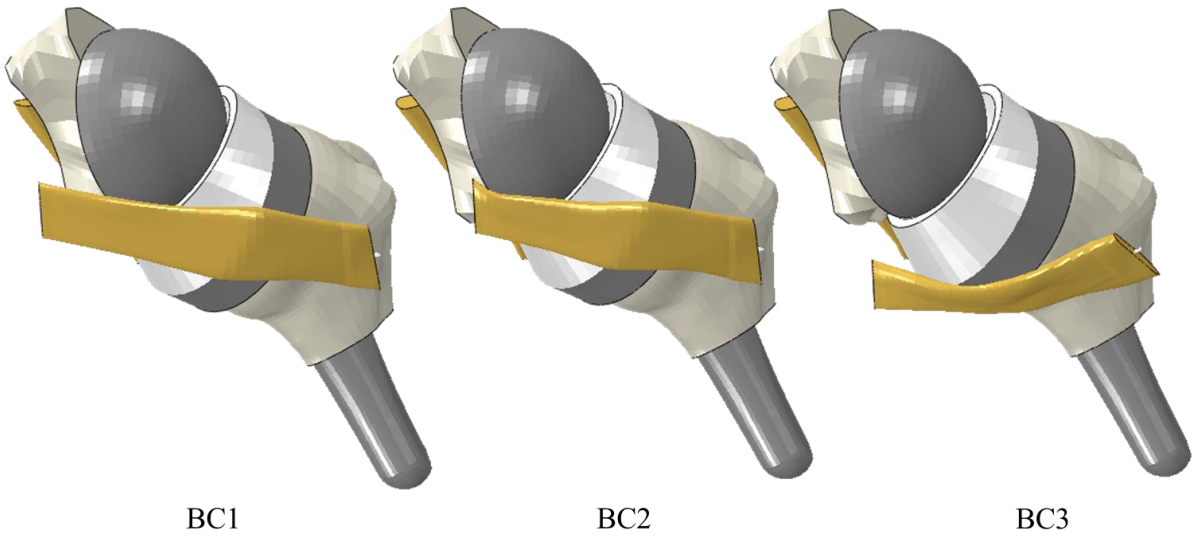

Figure 28: All cases are shown at the end of external rotation movement. The sliding inferior translation of the tendon is shown on the right model.

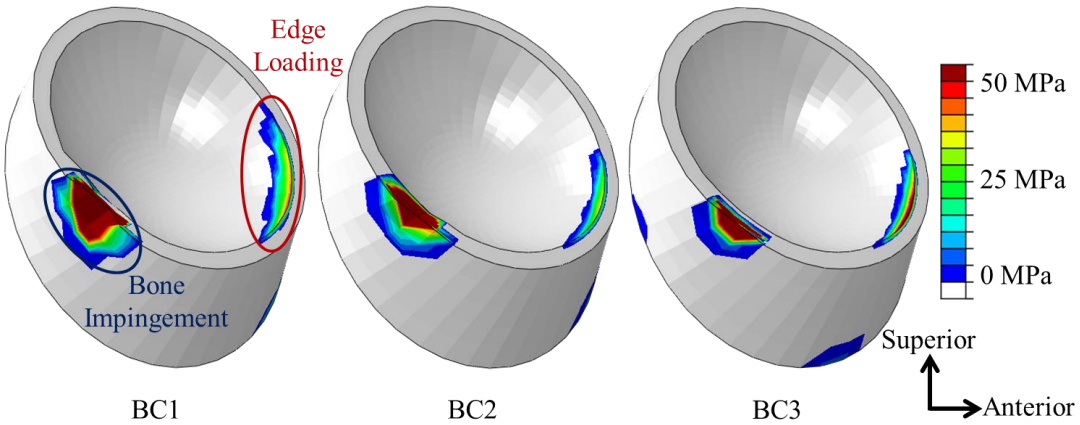

Figure 29: Contact stress contour plots of the BC1, BC2, and BC3 cases at 45° of external rotation. The large contact patch located posteriorly is the impingement site with the bone, while edge loading can be seen anteriorly and inferiorly in all models

The proximal spring boundary conditions exhibited behavior that was deemed to be more physically realistic than was observed in the three initial BC combinations. Forces developed in the tendons were more reasonable. In addition, as opposed to the constant force method (BC3), the proximal spring method provided greater stability to the proximal end of the tendon, preventing inferior dislocation of the humeral

polyethylene liner while still applying constant force. This constant force could also be tuned easily to match each tendon material model. Given this favorable behavior, all subsequent analyses were performed using this approach to model the proximal cuff tissue restraints.

Variation of material model and polyethylene liner rotation

Implant geometry was found to influence maximum subluxation generated during 45° of external rotation more than soft tissue tensile force. Significant differences in maximum subluxation were found between the three polyethylene liner rotations ($p<.001$). However, little effect in maximum subluxation was found due to changes in soft tissue tension (Figure 30). No impingement or subluxation was recorded for any of the subscapularis models with posteriorly rotated polyethylene liners. The least stiff material subscapularis neutral polyethylene liner models began subluxing at 31.5°, and the most stiff material subscapularis neutral polyethylene liner model began subluxing at 36°. Maximum subluxation for the neutral polyethylene liner rotation models only varied 0.5 mm between the most and least stiff subscapularis material models. For the anterior rotated models, the least stiff subscapularis model begin subluxing at 15.75°, and the most stiff began subluxing at 20.25°.

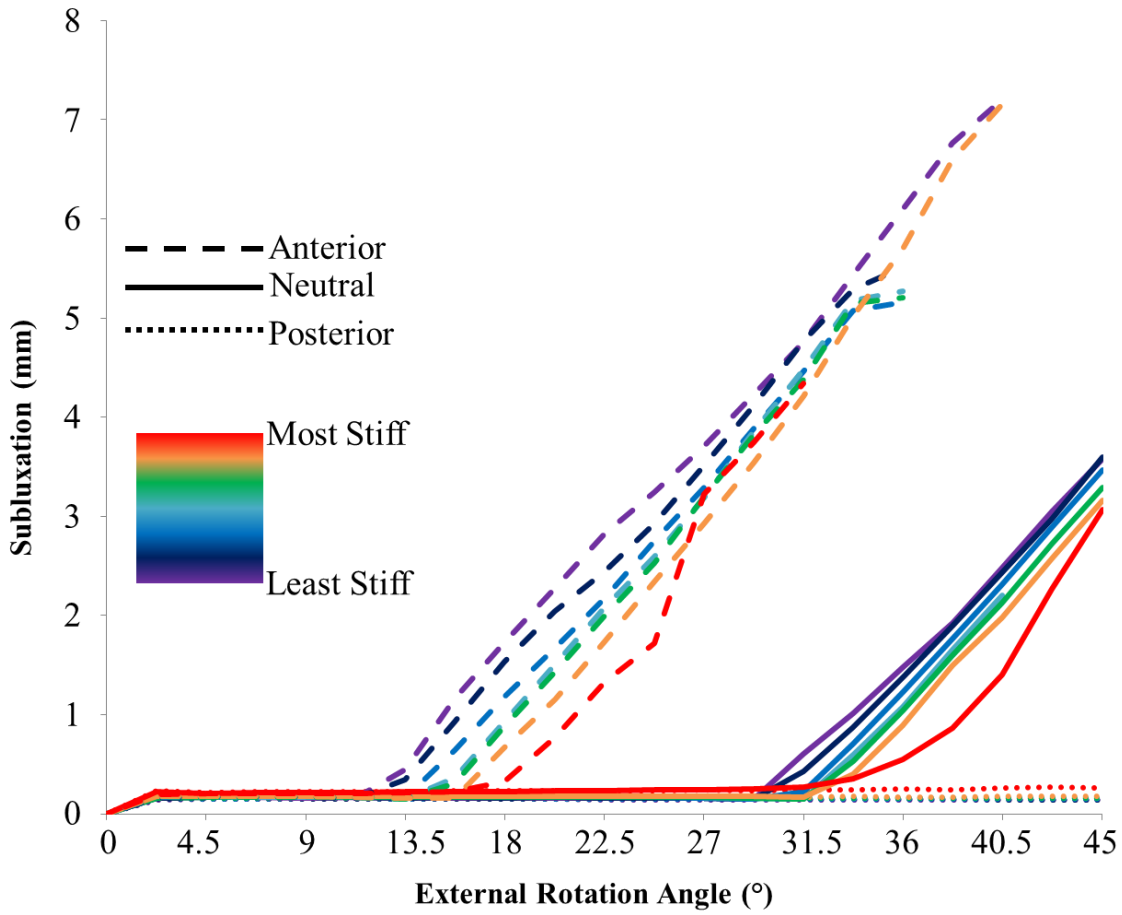

Figure 30: Effect of changes in polyethylene liner rotation and soft tissue tension on subluxation during external rotation. All posteriorly rotated polyethylene liners are plotted as dotted lines, neutral as solid lines, and anterior as dashed lines. Polyethylene liner rotation was found to have much greater effects on subluxation than soft tissue. The red plotted lines represent the least stiff soft tissue, and the purple lines represent the most stiff soft tissue models.

However, soft tissue tension did affect contact stress experienced by the polyethylene liner. Models with less stiff material properties experienced less contact stress at the impingement site. With greater tendon tension, contact stress values at the impingement site became more concentrated. Furthermore, with greater soft tissue tension, contact stress shifted from posterior to anterior. Finally, the models with greatest tension experienced edge loading anterior near the rim of the polyethylene liner. The contour plots of maximum contact stress experienced by every node throughout the entire

external rotation motion are shown in Figure 31. Closer examination of the polyethylene liners for the least and most stiff models is shown in Figure 32.

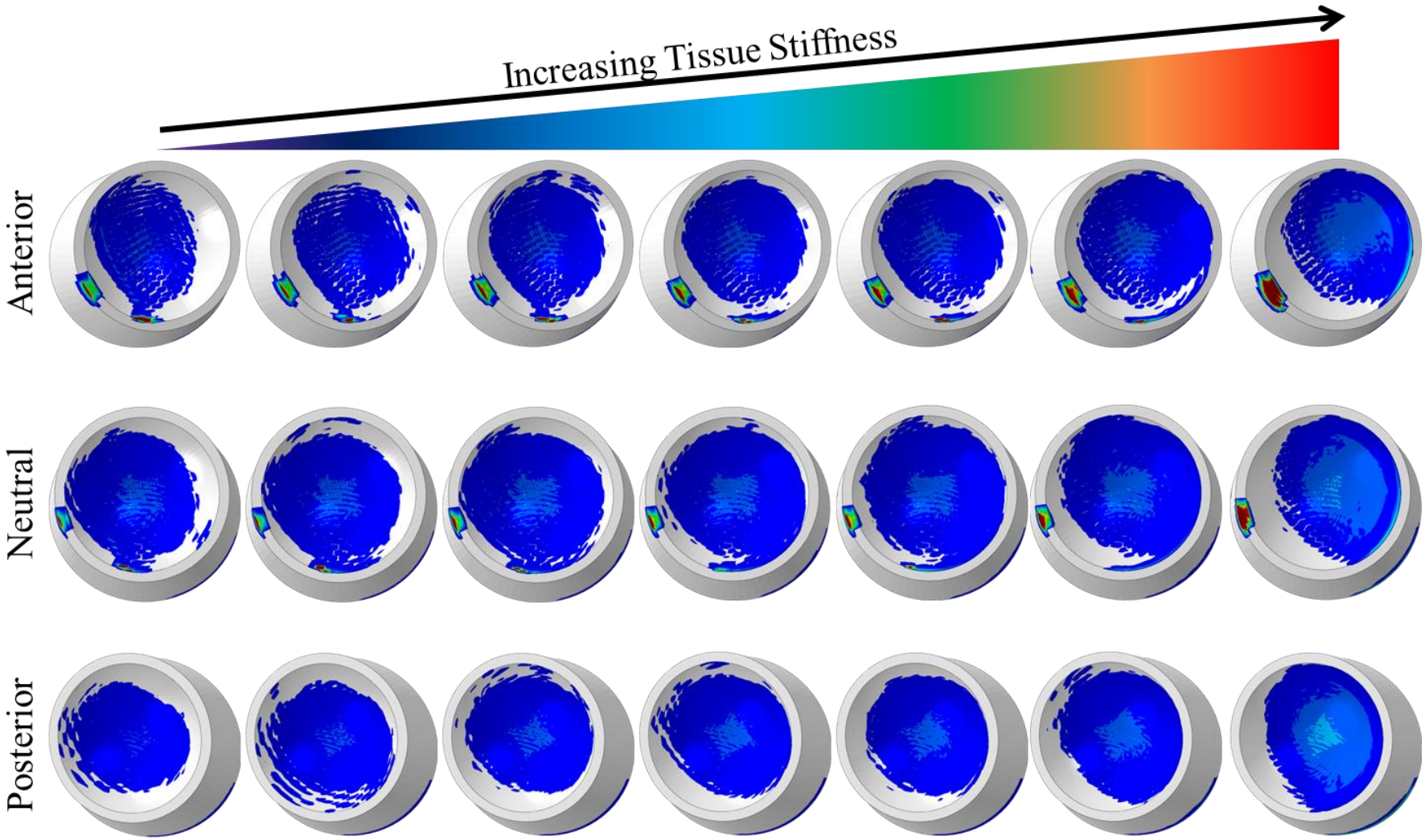

Figure 31: Contour plots of the maximum contact stresses experienced by every node for the entire external rotation motion.

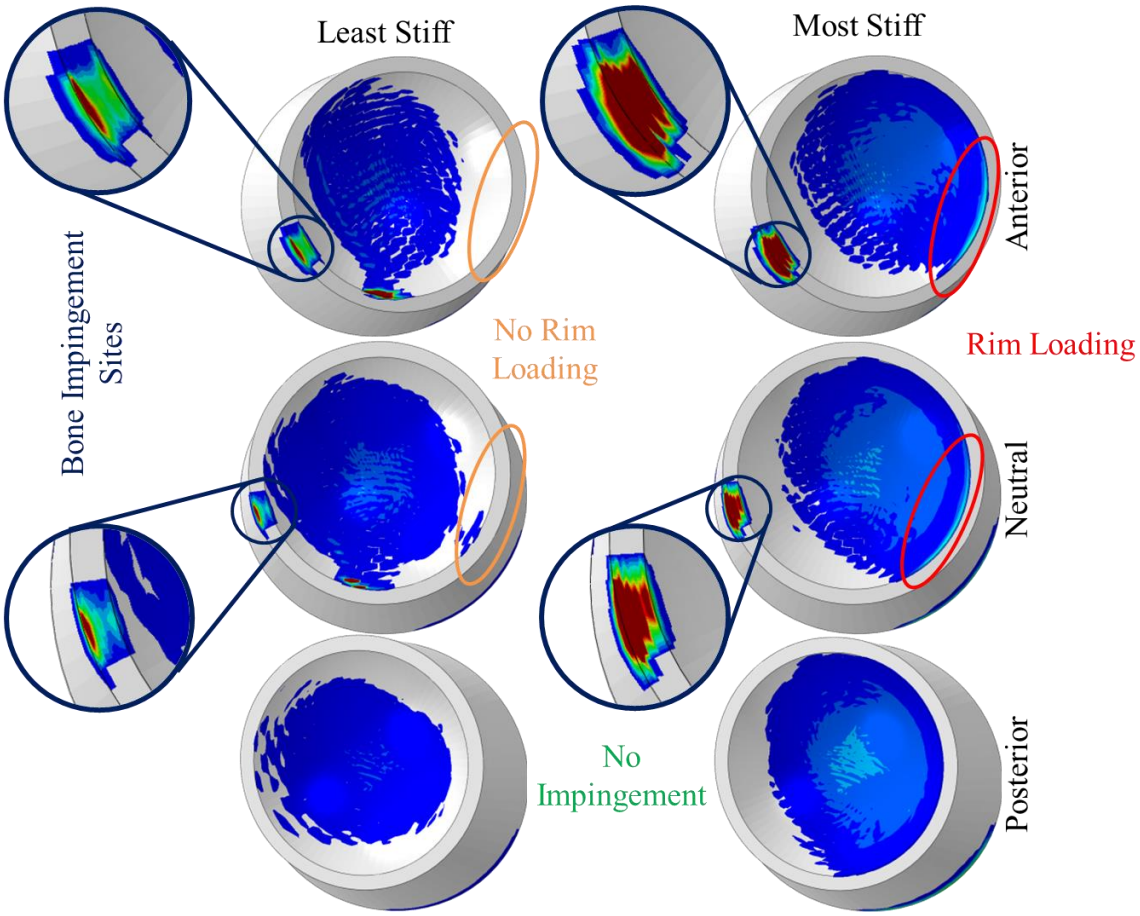

Figure 32: Maximum contact stress contour plots of the polyethylene liner for the least stiff and most stiff subscapularis material models paired with anterior, neutral, and posterior polyethylene liner rotation models. The least stiff material models experienced much lower contact stress at the bone impingement site than the most stiff material model. In addition, contact stress at anterior edge, indicating rim or edge loading, was only seen in the most stiff subscapularis material model. No bone impingement was found for the posterior rotated polyethylene liner models.

Discussion

In this study, explicit representation of the subscapularis and infraspinatus tendon tissues was introduced to investigate the stabilizing influence of soft tissue restraints about the shoulder following RSA. The benefit of this approach over those previously used is the inclusion of continuum tendon elements. Previous models represented rotator cuff soft tissues as spring elements, which lack the option for contact modeling to apply a buttressing distributed load over the polyethylene liner (as would be seen in-vivo). The continuum element approach also provides the ability to study edge loading that develops in the polyethylene liner during impingement.

Varying the method in which the subscapularis tendon is modeled proximally significantly affects the contact stress experienced by the polyethylene liner, as well as the position of the tendon during external rotation. For the constant force magnitude and direction case (BC3) the tendon slipped inferiorly during external rotation, creating more instability. This phenomenon may occur in-vivo, as tendons are free to slide and translate. Also, many clinical examples exist of tendons slipping or migrating from their preferred location such as biceps tendon subluxation [118].

Interestingly, the geometry and orientation of the implant system were found to have significantly more effect on subluxation during external rotation than tendon tension. Although more subscapularis tension reduced subluxation, the amount of reduction was limited, especially when compared to the effect of polyethylene rotation. However, increasing subscapularis tension did affect contact at the bone impingement site, making it more concentrated, higher in magnitude, and larger in size. Furthermore,

higher tendon tension shifted contact in the liner anteriorly, eventually inducing edge or rim loading.

Finally, many of the models experienced high contact stresses at the inferior edge of the polyethylene liner, especially in the lower stiffness subscapularis models. This was caused by a grinding contact between the inferior glenosphere and polyethylene liner when subluxation occurred. As subluxation occurred, the humeral component pivoted about the impingement site, and the rim of the liner would catch on the inferior edge of the glenosphere. In this model, the glenosphere is modeled as a perfect glenosphere, while the physical implant has a partially rounded edge. However, even that rounded edge could cause wear at the interface, and this may be a possible explanation for some wear seen in retrievals.

These results indicate that tissue tension is perhaps less tied to instability and more linked with scapular notching risk than previously thought. In this study, subluxation amount was primarily affect by implant and bone geometry. However, when impingement did occur, the contact at the impingement site was influenced by the tension of the soft tissue. In external rotation, these results indicate that, although external rotation range of motion is tied to scapular notching risk, it is also strongly, or perhaps more strongly, tied to risk of instability than soft tissue tension.

Conclusion

We developed a finite element modeling approach to study stability in RSA using continuum element representation of soft tissue constraints, including the subscapularis and infraspinatus tendons. Contrary to current theories in the field, subluxation and instability were more closely linked to external rotation range of motion, dictated by implant and bone geometry. Furthermore, subscapularis tissue quality was linked to scapular notching risk, with increasing subscapularis tissue stiffness creating larger contact stress values at the impingement site. The spring boundary conditions modeled at the proximal ends of these tendons influence the mechanics of the joint and must be validated. The modeling approach allows computation of complex tendon wrapping and instability of an in vivo joint.

CHAPTER 5: GENERAL DISCUSSION

This project was created to study scapular notching in RSA, and the original FE model was developed for that purpose. However, over time, the project evolved to address factors and complications presented in the literature such as effective deltoid moment arm or strength, glenoid version, polyethylene liner rotation, instability, etc. Currently, the state of the model allows for the study of many issues associated with RSA.

Despite promising computational results, a full physical validation of the results would be good practice. This would likely include RSA implantations of cadaveric specimens. In this current FE model, external rotation is the primary motion studied. As such, a method for prescribing external rotation through a servo hydraulic device like an MTS testing machine would need to be developed. Variables of interest would include contact stress at the impingement site and subluxation. Previously, contact stress at the impingement site was measured using a Tekscan sensor. However, the resolution of the Tekscan was too low to allow direct comparison to the FE model. The mesh resolution of the model is high in the inferior glenoid region to better study contact at the impingement site. For future contact stress measurement, higher resolution Tekscan sensors should be used to better capture the contact. Subluxation would be a more difficult outcome to measure. Optical motion tracking might be valuable in measuring this. However, if the humerus is fixed in rotation, the scapula must be allowed to float to measure subluxation. Overall, the validation effort will be significant but the outcomes of such a study are important.

Once validation is finished, the important issue of tendon tensioning in RSA should be addressed. Over-tensioning of the shoulder capsule has been shown here to have little effect on subluxation and instability, but increase contact stress at the impingement site leading to scapular notching. Now, a platform exists in which the tensioning of the shoulder can be studied. I can envision in the future a study in which multiple surgeons are tasked with closing an RSA procedure in a cadaveric setting. The tension placed on the tissue could then be measured and used as an input into this model. This data would help with boundary condition definition.

The addition of proper soft tissue modeling could lead to the development of wear modeling. Wear is a large issue in RSA. As shown previously, the delamination and destruction of the polyethylene liner associated with scapular notching is evident. When validated, this model can serve to analyze what motions, implant geometries, and implantations can decelerate or accelerate wear in the polyethylene liner. In order to do this however, a great amount of work formulating a wear model would need to be done. Previously, wear was studied in the hip in this lab [119-121]. Much of this, however, was done to address wear of the polyethylene cup due to scratches of the metal bearing surface. In the shoulder, a new contact interface would need to be studied, analyzing the wear characteristics present when scapular bone contacts polyethylene. Also, in the hip, wear is modeled primarily to prevent osteolysis. Although this may be a problem in RSA in the future, currently, the wear seen due to scapular notching is far greater. Therefore, a new wear formulation would need to be developed, most likely incorporating adaptive remeshing of the humeral polyethylene liner and bone with between loading cycles [122].

In general, the work presented here provides an important foundation for additional, complex, clinically helpful FE models studying RSA.

REFERENCES

1. Hall, S.J., *Basic Biomechanics*. 5th ed. 2007, New York, NY: McGraw-Hill.

2. O'Brien, S.J., et al., *The anatomy and histology of the inferior glenohumeral ligament complex of the shoulder.* Am J Sports Med, 1990. **18**(5): p. 449-56.

3. Warner, J.J., et al., *Static capsuloligamentous restraints to superior-inferior translation of the glenohumeral joint*. Am J Sports Med, 1992. **20**(6): p. 675-85.

4. Steinbeck, J., U. Liljenqvist, and J. Jerosch, *The anatomy of the glenohumeral ligamentous complex and its contribution to anterior shoulder stability.* J Shoulder Elbow Surg, 1998. **7**(2): p. 122-6.

5. Hoffman, M. *Picture of the Shoulder*. [cited 2017 February 24th]; Available from: http://www.webmd.com/pain-management/picture-of-the-shoulder#1.

6. Mather, R.C., 3rd, et al., *The societal and economic value of rotator cuff repair.* J Bone Joint Surg Am, 2013. **95**(22): p. 1993-2000.

7. Boileau, P., et al., *Grammont reverse prosthesis: design, rationale, and biomechanics.* J Shoulder Elbow Surg, 2005. **14**(1 Suppl S): p. 147S-161S.

8. Boileau, P., et al., *Neer Award 2005: The Grammont reverse shoulder prosthesis: results in cuff tear arthritis, fracture sequelae, and revision arthroplasty.* J Shoulder Elbow Surg, 2006. **15**(5): p. 527-40.

9. Feeley, B.T., R.A. Gallo, and E.V. Craig, *Cuff tear arthropathy: current trends in diagnosis and surgical management*. J Shoulder Elbow Surg, 2009. **18**(3): p. 484-94.

10. Gerber, C., S.D. Pennington, and R.W. Nyffeler, *Reverse total shoulder arthroplasty.* J Am Acad Orthop Surg, 2009. **17**(5): p. 284-95.

11. Ramirez, M.A., J. Ramirez, and A.M. Murthi, *Reverse total shoulder arthroplasty for irreparable rotator cuff tears and cuff tear arthropathy.* Clin Sports Med, 2012. **31**(4): p. 749-59.

12. Neer, C.S., 2nd, E.V. Craig, and H. Fukuda, *Cuff-tear arthropathy.* J Bone Joint Surg Am, 1983. **65**(9): p. 1232-44.

13. Rittmeister, M. and F. Kerschbaumer, *Grammont reverse total shoulder arthroplasty in patients with rheumatoid arthritis and nonreconstructible rotator cuff lesions.* J Shoulder Elbow Surg, 2001. **10**(1): p. 17-22.

14. Frankle, M., et al., *The Reverse Shoulder Prosthesis for glenohumeral arthritis associated with severe rotator cuff deficiency. A minimum two-year follow-up study of sixty patients.* J Bone Joint Surg Am, 2005. **87**(8): p. 1697-705.

15. Ecklund, K.J., et al., *Rotator cuff tear arthropathy*. J Am Acad Orthop Surg, 2007. **15**(6): p. 340-9.

16. Cuff, D., et al., *Reverse shoulder arthroplasty for the treatment of rotator cuff deficiency*. J Bone Joint Surg Am, 2008. **90**(6): p. 1244-51.

17. Neer, C.S., 2nd, *Replacement arthroplasty for glenohumeral osteoarthritis*. J Bone Joint Surg Am, 1974. **56**(1): p. 1-13.

18. Sirveaux, F., et al., *Grammont inverted total shoulder arthroplasty in the treatment of glenohumeral osteoarthritis with massive rupture of the cuff. Results of a multicentre study of 80 shoulders*. J Bone Joint Surg Br, 2004. **86**(3): p. 388-95.

19. Frankle, M., et al., *The reverse shoulder prosthesis for glenohumeral arthritis associated with severe rotator cuff deficiency. a minimum two-year follow-up study of sixty patients surgical technique*. J Bone Joint Surg Am, 2006. **88 Suppl 1 Pt 2**: p. 178-90.

20. Guery, J., et al., *Reverse total shoulder arthroplasty. Survivorship analysis of eighty replacements followed for five to ten years*. J Bone Joint Surg Am, 2006. **88**(8): p. 1742-7.

21. McFarland, E.G., et al., *The reverse shoulder prosthesis: A review of imaging features and complications*. Skeletal Radiol, 2006. **35**(7): p. 488-96.

22. Rockwood, C.A., Jr., *The reverse total shoulder prosthesis. The new kid on the block*. J Bone Joint Surg Am, 2007. **89**(2): p. 233-5.

23. Wall, B., et al., *Reverse total shoulder arthroplasty: a review of results according to etiology*. J Bone Joint Surg Am, 2007. **89**(7): p. 1476-85.

24. Drake, G.N., D.P. O'Connor, and T.B. Edwards, *Indications for reverse total shoulder arthroplasty in rotator cuff disease*. Clin Orthop Relat Res, 2010. **468**(6): p. 1526-33.

25. Henninger, H.B., et al., *Biomechanical comparison of reverse total shoulder arthroplasty systems in soft tissue-constrained shoulders*. J Shoulder Elbow Surg, 2013.

26. Hsu, J.E., et al., *Addressing glenoid bone deficiency and asymmetric posterior erosion in shoulder arthroplasty*. J Shoulder Elbow Surg, 2013. **22**(9): p. 1298-308.

27. Hyun, Y.S., et al., *Uncommon Indications for Reverse Total Shoulder Arthroplasty*. Clin Orthop Surg, 2013. **5**(4): p. 243-255.

28. Routman, H.D., *Indications, technique, and pitfalls of reverse total shoulder arthroplasty for proximal humerus fractures.* Bull Hosp Jt Dis (2013), 2013. **71 Suppl 2**: p. 64-7.

29. Virani, N.A., et al., *Reverse shoulder arthroplasty components and surgical techniques that restore glenohumeral motion.* J Shoulder Elbow Surg, 2013. **22**(2): p. 179-87.

30. Raiss, P., et al., *Reverse shoulder arthroplasty for the treatment of nonunions of the surgical neck of the proximal part of the humerus (type-3 fracture sequelae).* J Bone Joint Surg Am, 2014. **96**(24): p. 2070-6.

31. Raiss, P., et al., *Reverse arthroplasty for osteoarthritis and rotator cuff deficiency after previous surgery for recurrent anterior shoulder instability.* Int Orthop, 2014. **38**(7): p. 1407-13.

32. Wiater, B.P., et al., *Elucidating trends in revision reverse total shoulder arthroplasty procedures: a retrieval study evaluating clinical, radiographic, and functional outcomes data.* J Shoulder Elbow Surg, 2015. **24**(12): p. 1915-25.

33. Wagner, E., et al., *Glenoid Bone-Grafting in Revision to a Reverse Total Shoulder Arthroplasty.* J Bone Joint Surg Am, 2015. **97**(20): p. 1653-60.

34. Westermann, R.W., et al., *Reverse Shoulder Arthroplasty in the United States: A Comparison of National Volume, Patient Demographics, Complications, and Surgical Indications.* Iowa Orthop J, 2015. **35**: p. 1-7.

35. Teusink, M.J., et al., *Results of closed management of acute dislocation after reverse shoulder arthroplasty.* J Shoulder Elbow Surg, 2015. **24**(4): p. 621-7.

36. Statz, J.M., et al., *Outcomes of primary reverse shoulder arthroplasty in patients with morbid obesity.* J Shoulder Elbow Surg, 2016.

37. Zumstein, M.A., et al., *Problems, complications, reoperations, and revisions in reverse total shoulder arthroplasty: a systematic review.* J Shoulder Elbow Surg, 2011. **20**(1): p. 146-57.

38. Walch, G., et al., *Do the indications, results, and complications of reverse shoulder arthroplasty change with surgeon's experience?* J Shoulder Elbow Surg, 2012. **21**(11): p. 1470-7.

39. Ek, E.T., et al., *Reverse total shoulder arthroplasty for massive irreparable rotator cuff tears in patients younger than 65 years old: results after five to fifteen years.* J Shoulder Elbow Surg, 2013. **22**(9): p. 1199-208.

40. Werner, B.S., D. Boehm, and F. Gohlke, *Revision to reverse shoulder arthroplasty with retention of the humeral component.* Acta Orthop, 2013. **84**(5): p. 473-8.

41. Boileau, P., *Complications and revision of reverse total shoulder arthroplasty.* Orthop Traumatol Surg Res, 2016. **102**(1 Suppl): p. S33-43.

42. Simovitch, R.W., et al., *Predictors of scapular notching in patients managed with the Delta III reverse total shoulder replacement.* J Bone Joint Surg Am, 2007. **89**(3): p. 588-600.

43. Levigne, C., et al., *Scapular notching in reverse shoulder arthroplasty.* J Shoulder Elbow Surg, 2008. **17**(6): p. 925-35.

44. Chou, J., et al., *Biomechanical evaluation of different designs of glenospheres in the SMR reverse total shoulder prosthesis: range of motion and risk of scapular notching.* J Shoulder Elbow Surg, 2009. **18**(3): p. 354-9.

45. de Wilde, L.F., et al., *Prosthetic overhang is the most effective way to prevent scapular conflict in a reverse total shoulder prosthesis.* Acta Orthop, 2010. **81**(6): p. 719-26.

46. Farshad, M. and C. Gerber, *Reverse total shoulder arthroplasty-from the most to the least common complication.* Int Orthop, 2010. **34**(8): p. 1075-82.

47. Falaise, V., et al., *Scapular notching in reverse shoulder arthroplasties: the influence of glenometaphyseal angle.* Orthop Traumatol Surg Res, 2011. **97**(6 Suppl): p. S131-7.

48. Kempton, L.B., et al., *A radiographic analysis of the effects of glenosphere position on scapular notching following reverse total shoulder arthroplasty.* J Shoulder Elbow Surg, 2011. **20**(6): p. 968-74.

49. Levigne, C., et al., *Scapular notching in reverse shoulder arthroplasty: is it important to avoid it and how?* Clin Orthop Relat Res, 2011. **469**(9): p. 2512-20.

50. Nicholson, G.P., E.J. Strauss, and S.L. Sherman, *Scapular notching: Recognition and strategies to minimize clinical impact.* Clin Orthop Relat Res, 2011. **469**(9): p. 2521-30.

51. Kowalsky, M.S., et al., *The relationship between scapular notching and reverse shoulder arthroplasty prosthesis design.* J Shoulder Elbow Surg, 2012. **21**(10): p. 1430-41.

52. Berhouet, J., P. Garaud, and L. Favard, *Evaluation of the role of glenosphere design and humeral component retroversion in avoiding scapular notching during reverse shoulder arthroplasty.* J Shoulder Elbow Surg, 2013.

53. Sadoghi, P., et al., *Infraglenoidal scapular notching in reverse total shoulder replacement: a prospective series of 60 cases and systematic review of the literature.* BMC Musculoskelet Disord, 2011. **12**: p. 101.

54. Cuff, D., et al., *Reverse shoulder arthroplasty for the treatment of rotator cuff deficiency: a concise follow-up, at a minimum of five years, of a previous report.* J Bone Joint Surg Am, 2012. **94**(21): p. 1996-2000.

55. Boileau, P., et al., *Revision surgery of reverse shoulder arthroplasty.* J Shoulder Elbow Surg, 2013. **22**(10): p. 1359-70.

56. Chalmers, P.N., et al., *Early dislocation after reverse total shoulder arthroplasty.* J Shoulder Elbow Surg, 2014. **23**(5): p. 737-44.

57. Nyffeler, R.W., et al., *Analysis of a retrieved delta III total shoulder prosthesis.* J Bone Joint Surg Br, 2004. **86**(8): p. 1187-91.

58. Hettrich, C.M., et al., *Mechanical tradeoffs associated with glenosphere lateralization in reverse shoulder arthroplasty.* J Shoulder Elbow Surg, 2015. **24**(11): p. 1774-81.

59. Permeswaran, V.N., et al., *Cadaveric validation of a finite element modeling approach for studying scapular notching in reverse shoulder arthroplasty.* J Biomech, 2016. **49**(13): p. 3069-3073.

60. Zheng, M., et al., *Finite element models of the human shoulder complex: a review of their clinical implications and modelling techniques.* Int J Numer Method Biomed Eng, 2017. **33**(2).

61. Debski, R.E., et al., *Stress and strain in the anterior band of the inferior glenohumeral ligament during a simulated clinical examination.* J Shoulder Elbow Surg, 2005. **14**(1 Suppl S): p. 24S-31S.

62. Ellis, B.J., et al., *Methodology and sensitivity studies for finite element modeling of the inferior glenohumeral ligament complex*. J Biomech, 2007. **40**(3): p. 603-12.

63. Moore, S.M., et al., *The current anatomical description of the inferior glenohumeral ligament does not correlate with its functional role in positions of external rotation.* J Orthop Res, 2008. **26**(12): p. 1598-604.

64. Drury, N.J., et al., *The impact of glenoid labrum thickness and modulus on labrum and glenohumeral capsule function.* J Biomech Eng, 2010. **132**(12): p. 121003.

65. Ellis, B.J., et al., *Finite element modelling of the glenohumeral capsule can help assess the tested region during a clinical exam*. Comput Methods Biomech Biomed Engin, 2010. **13**(3): p. 413-8.

66. Moore, S.M., et al., *The glenohumeral capsule should be evaluated as a sheet of fibrous tissue: a validated finite element model.* Ann Biomed Eng, 2010. **38**(1): p. 66-76.

67. Drury, N.J., et al., *Finding consistent strain distributions in the glenohumeral capsule between two subjects: implications for development of physical examinations.* J Biomech, 2011. **44**(4): p. 607-13.

68. Moore, S.M., P.J. McMahon, and R.E. Debski, *Bi-directional mechanical properties of the axillary pouch of the glenohumeral capsule: implications for modeling and surgical repair.* J Biomech Eng, 2004. **126**(2): p. 284-8.

69. Ahir, S.P., et al., *Analysis of glenoid fixation for a reversed anatomy fixed-fulcrum shoulder replacement.* J Biomech, 2004. **37**(11): p. 1699-708.

70. Virani, N.A., et al., *In vitro and finite element analysis of glenoid bone/baseplate interaction in the reverse shoulder design.* J Shoulder Elbow Surg, 2008. **17**(3): p. 509-21.

71. Favre, P., et al., *In vitro assessments of reverse glenoid stability using displacement gages are misleading - recommendations for accurate measurements of interface micromotion.* Clin Biomech (Bristol, Avon), 2011. **26**(9): p. 917-22.

72. Nigro, P.T., S. Gutierrez, and M.A. Frankle, *Improving glenoid-side load sharing in a virtual reverse shoulder arthroplasty model.* J Shoulder Elbow Surg, 2013. **22**(7): p. 954-62.

73. Yang, C.C., et al., *Stress analysis of glenoid component in design of reverse shoulder prosthesis using finite element method.* J Shoulder Elbow Surg, 2013. **22**(7): p. 932-9.

74. Quental, C., et al., *Bone remodelling of the scapula after a total shoulder arthroplasty.* Biomech Model Mechanobiol, 2014. **13**(4): p. 827-38.

75. Chae, S.W., et al., *Primary stability of inferior tilt fixation of the glenoid component in reverse total shoulder arthroplasty: A finite element study.* J Orthop Res, 2016. **34**(6): p. 1061-8.

76. Denard, P.J., et al., *Finite element analysis of glenoid-sided lateralization in reverse shoulder arthroplasty.* J Orthop Res, 2016.

77. Wong, M.T., et al., *Implant positioning in reverse shoulder arthroplasty has an impact on acromial stresses.* J Shoulder Elbow Surg, 2016. **25**(11): p. 1889-1895.

78. Elwell, J., J. Choi, and R. Willing, *Quantifying the competing relationship between adduction range of motion and baseplate micromotion with lateralization of reverse total shoulder arthroplasty.* J Biomech, 2017. **52**: p. 24-30.

79. Elkins, J.M., et al., *The capsule's contribution to total hip construct stability--a finite element analysis.* J Orthop Res, 2011. **29**(11): p. 1642-8.

80. Elkins, J.M., et al., *Hard-on-hard total hip impingement causes extreme contact stress concentrations.* Clin Orthop Relat Res, 2011. **469**(2): p. 454-63.

81. Elkins, J.M., et al., *Morbid obesity may increase dislocation in total hip patients: a biomechanical analysis.* Clin Orthop Relat Res, 2013. **471**(3): p. 971-80.

82. Brown, T.D., et al., *Impingement and dislocation in total hip arthroplasty: mechanisms and consequences.* Iowa Orthop J, 2014. **34**: p. 1-15.

83. Elkins, J.M., J.J. Callaghan, and T.D. Brown, *The 2014 Frank Stinchfield Award: The 'landing zone' for wear and stability in total hip arthroplasty is smaller than we thought: a computational analysis.* Clin Orthop Relat Res, 2015. **473**(2): p. 441-52.

84. *Standard Test Methods for Dynamic Evaluation of Glenoid Loosening or Disassociation*. 2014, ASTM International: West Conshohocken, PA.

85. Langohr, G.D., et al., *Contact mechanics of reverse total shoulder arthroplasty during abduction: the effect of neck-shaft angle, humeral cup depth, and glenosphere diameter.* J Shoulder Elbow Surg, 2016. **25**(4): p. 589-97.

86. Seki, N., et al., *Mechanical environment of the supraspinatus tendon: three-dimensional finite element model analysis.* J Orthop Sci, 2008. **13**(4): p. 348-53.

87. Szczesny, S.E., et al., *Biaxial tensile testing and constitutive modeling of human supraspinatus tendon.* J Biomech Eng, 2012. **134**(2): p. 021004.

88. Thunes, J., et al., *The Effect of Size and Location of Tears in the Supraspinatus Tendon on Potential Tear Propagation.* J Biomech Eng, 2015. **137**(8): p. 081012.

89. Araki, D., et al., *Effect of tear location on propagation of isolated supraspinatus tendon tears during increasing levels of cyclic loading.* J Bone Joint Surg Am, 2015. **97**(4): p. 273-8.

90. Keener, J.D., et al., *A prospective evaluation of survivorship of asymptomatic degenerative rotator cuff tears.* J Bone Joint Surg Am, 2015. **97**(2): p. 89-98.

91. Wieser, K., et al., *Fluoroscopic, magnetic resonance imaging, and electrophysiologic assessment of shoulders with massive tears of the rotator cuff.* J Shoulder Elbow Surg, 2015. **24**(2): p. 288-94.

92. Mantovani, M., et al., *A 3D finite element model for geometrical and mechanical comparison of different supraspinatus repair techniques.* J Shoulder Elbow Surg, 2016. **25**(4): p. 557-63.

93. Halder, A., et al., *Structural properties of the subscapularis tendon.* J Orthop Res, 2000. **18**(5): p. 829-34.

94. Halder, A., et al., *Mechanical properties of the posterior rotator cuff.* Clin Biomech (Bristol, Avon), 2000. **15**(6): p. 456-62.

95. Boileau, P., et al., *Arthroplasty of the shoulder.* J Bone Joint Surg Br, 2006. **88**(5): p. 562-75.

96. Boileau, P., et al., *Bony increased-offset reversed shoulder arthroplasty: minimizing scapular impingement while maximizing glenoid fixation.* Clin Orthop Relat Res, 2011. **469**(9): p. 2558-67.

97. Day, J.S., et al., *Prevalence and projections of total shoulder and elbow arthroplasty in the United States to 2015.* J Shoulder Elbow Surg, 2010. **19**(8): p. 1115-20.

98. Nam, D., et al., *Rotator cuff tear arthropathy: evaluation, diagnosis, and treatment: AAOS exhibit selection.* J Bone Joint Surg Am, 2012. **94**(6): p. e34.

99. Day, J.S., et al., *Polyethylene wear in retrieved reverse total shoulder components.* J Shoulder Elbow Surg, 2012. **21**(5): p. 667-74.

100. Roche, C., et al., *An evaluation of the relationships between reverse shoulder design parameters and range of motion, impingement, and stability.* J Shoulder Elbow Surg, 2009. **18**(5): p. 734-41.

101. Permeswaran, V.N., et al., *Cadaveric validation of a finite element modeling approach for studying scapular notching in reverse shoulder arthroplasty.* J Biomech, 2016.

102. Morrow, D.A., et al., *Transversely isotropic tensile material properties of skeletal muscle tissue.* J Mech Behav Biomed Mater, 2010. **3**(1): p. 124-9.

103. Peterson, S.L. and G.M. Rayan, *Shoulder and upper arm muscle architecture.* J Hand Surg Am, 2011. **36**(5): p. 881-9.

104. Friedman, R.J., K.B. Hawthorne, and B.M. Genez, *The use of computerized tomography in the measurement of glenoid version.* J Bone Joint Surg Am, 1992. **74**(7): p. 1032-7.

105. Bryce, C.D., et al., *Two-dimensional glenoid version measurements vary with coronal and sagittal scapular rotation.* J Bone Joint Surg Am, 2010. **92**(3): p. 692-9.

106. Lewicki, K.A., J.E. Bell, and D.W. Van Citters, *Analysis of polyethylene wear of reverse shoulder components: A validated technique and initial clinical results.* J Orthop Res, 2016.

107. Nam, D., et al., *Reverse total shoulder arthroplasty: current concepts, results, and component wear analysis.* J Bone Joint Surg Am, 2010. **92 Suppl 2**: p. 23-35.

108. Andarawis-Puri, N., E.T. Ricchetti, and L.J. Soslowsky, *Interaction between the supraspinatus and infraspinatus tendons: effect of anterior supraspinatus tendon full-thickness tears on infraspinatus tendon strain.* Am J Sports Med, 2009. **37**(9): p. 1831-9.

109. Bellman, R.E. and Rand Corporation., *Dynamic programming*. 1957, Princeton,: Princeton University Press. xxv, 342 p.

110. Pontriagin, L.S., *The mathematical theory of optimal processes*. 1962, New York,: Interscience Publishers. viii, 360 p.

111. Ono, S., *The skin in amyotrophic lateral sclerosis.* Amyotroph Lateral Scler Other Motor Neuron Disord, 2000. **1**(3): p. 191-9.

112. Huiskes, R. and E.Y. Chao, *A survey of finite element analysis in orthopedic biomechanics: the first decade.* J Biomech, 1983. **16**(6): p. 385-409.

113. Smith, C.D., P. Guyver, and T.D. Bunker, *Indications for reverse shoulder replacement: a systematic review*. J Bone Joint Surg Br, 2012. **94**(5): p. 577-83.

114. Clark, J.C., et al., *Complication rates, dislocation, pain, and postoperative range of motion after reverse shoulder arthroplasty in patients with and without repair of the subscapularis.* J Shoulder Elbow Surg, 2012. **21**(1): p. 36-41.

115. Stephenson, D.R., et al., *Effect of humeral component version on impingement in reverse total shoulder arthroplasty.* J Shoulder Elbow Surg, 2011. **20**(4): p. 652-8.

116. Edwards, T.B., et al., *Subscapularis insufficiency and the risk of shoulder dislocation after reverse shoulder arthroplasty.* J Shoulder Elbow Surg, 2009. **18**(6): p. 892-6.

117. Gadea, F., et al., *Deltopectoral approach for shoulder arthroplasty: anatomic basis.* Int Orthop, 2015. **39**(2): p. 215-25.

118. Shi, L.L., et al., *Accuracy of long head of the biceps subluxation as a predictor for subscapularis tears.* Arthroscopy, 2015. **31**(4): p. 615-9.

119. Kruger, K.M., et al., *Encoding scratch and scrape features for wear modeling of total joint replacements.* Comput Math Methods Med, 2013. **2013**: p. 624267.

120. Kruger, K.M., et al., *Modeling polyethylene wear acceleration due to femoral head dislocation damage.* J Arthroplasty, 2014. **29**(8): p. 1653-1657 e1.

121. Kruger, K.M., et al., *A novel formulation for scratch-based wear modelling in total hip arthroplasty*. Comput Methods Biomech Biomed Engin, 2014. **17**(11): p. 1227-36.

122. Maxian, T.A., et al., *Adaptive finite element modeling of long-term polyethylene wear in total hip arthroplasty*. J Orthop Res, 1996. **14**(4): p. 668-75.

APPENDIX A: MECHANICAL TRADEOFFS ASSOCIATED WITH GLENOSPHERE LATERALIZAITON REVERSE SHOULDER ARTHROPLASTY

J Shoulder Elbow Surg (2015) 24, 1774-1781

ELSEVIER

Journal of Shoulder and Elbow Surgery

www.elsevier.com/locate/ymse

Mechanical tradeoffs associated with glenosphere lateralization in reverse shoulder arthroplasty

Carolyn M. Hettrich, MD, MPH*, Vijay N. Permeswaran, MS, Jessica E. Goetz, PhD, Donald D. Anderson, PhD

Department of Orthopaedics and Rehabilitation, University of Iowa, Iowa City, IA, USA

Background: Scapular notching in reverse shoulder arthroplasty occurs in up to 97% of patients. Notching is associated with decreased strength and reduced motion and may lead to long-term failure due to polyethylene wear. Many implant systems lateralize the glenosphere to address scapular notching, but the mechanical tradeoffs of lateralization have not been rigorously evaluated. We hypothesized that lateralization would decrease bony impingement but also decrease the mechanical advantage of the deltoid.

Methods: Finite element models were created using the same implants with different amounts of glenoid lateralization: 5 mm of medialization to replicate glenoid erosion, as well as 2.5, 5, 7.5, and 10 mm of lateralization. Tests were performed with static and dynamic scapulae for motion in either the coronal or scapular plane. The angle of impingement between the scapula and the humeral polyethylene was recorded, as was the deltoid force required to elevate the arm.

Results: Increasing lateralization decreased impingement while increasing the deltoid force required to elevate the arm. Differences were found between the static and dynamic scapulae, with the dynamic scapula model having increased humeral adduction before impinging. The impingement angle was also substantially affected by the bony prominences on the inferior scapula, showing how individual bony anatomy can affect impingement.

Conclusion: Lateralization is effective in increasing impingement-free range of motion but also increases the deltoid force required to perform identical tasks. In addition, impingement is determined by scapular motion, which should be included in all shoulder models.

Level of evidence: Basic Science Study, Computer Modeling.

Keywords: Glenospere lateralization; reverse shoulder arthroplasty; deltoid force; impingement; scapular notching; finite element analysis

The success of reverse shoulder arthroplasty (RSA) has led to expansion of its indications from cuff tear arthropathy (CTA)[9,10,12,13] to any condition of the shoulder in which the rotator cuff is deficient.[1,2,4,5,13,15,18,19,21,28,29] RSA was traditionally only performed in elderly patients, but there has been a shift in use to younger populations.[11]

Institutional review board approval was received for the collection of patient data that were used for data inputs into our model (IRB No. 201211724).

*Reprint requests: Carolyn M. Hettrich, MD, MPH, 2701 Prairie Meadow Dr, Iowa City, IA 52240, USA.

E-mail address: carolyn-hettrich@uiowa.edu (C.M. Hettrich).

1058-2746/$ - see front matter © 2015 Journal of Shoulder and Elbow Surgery Board of Trustees.
http://dx.doi.org/10.1016/j.jse.2015.06.011

As a result, RSA use has increased by 7% to 13% annually since 2007, currently comprising 37% of the shoulder arthroplasty market,[6] and this use is expected to continue to grow.[26]

A recent systematic review of the complications from RSA unfortunately showed that this is a procedure with high complication rates.[34] The global problem rate was 44%, and the complication rate was 24%. The most common problem was scapular notching, which occurred in 35% of patients, and the most common complication was instability (4.7% of patients). Although problems were defined as not being likely to affect the patient's final outcome, the long-term consequences of polyethylene wear from scapular notching have not been determined and this wear may in fact influence the long-term outcome. Many of the most commonly cited problems and complications were attributable to a poor or incomplete understanding of the mechanical implications of a given implant design or implant placement.

Scapular notching has been reported to occur after RSA in 31% to 97% of patients, often within 6 months of surgery.[32] Scapular notching is a result of mechanical impingement of the medial rim of the humeral component against the scapular neck when the arm is adducted, and it is thought to be a risk factor for glenoid loosening, instability, and implant wear. Clinically, scapular notching has been found to result in decreased postoperative strength,[14,19] decreased Constant scores,[24,25] decreased active range of motion,[23,24] and increased pain.[23] Polyethylene wear and osteolysis have not yet been reported to be causes of failure; however, only midterm results have been published to date. Retrieval studies have shown relatively high rates of polyethylene wear in patients with scapular notching,[7] and it is a reasonable concern that this will cause long-term failures.

One solution to notching is to lateralize the glenosphere, either by changing the glenosphere design or by placing bone graft between the baseplate and the remaining glenoid.[3] However, lateralization involves a mechanical tradeoff[17] because it decreases the moment arm of the deltoid,[14] possibly resulting in decreased active range of motion and strength. There is also associated with lateralization an elevation of stress at the glenoid-baseplate interface,[22,27] which can lead to glenoid failure. The clinical and mechanical implications of these modifications to implant design and use are not yet well understood. In addition, modifying the center of rotation is but one of a number of recently proposed design changes, each likewise with largely unexplored mechanical consequences.

Hoenecke et al[14] recently used musculoskeletal modeling software to better characterize the changes in the risk of impingement and deltoid efficiency associated with lateralization of the glenosphere (6 mm and 13 mm of lateralization were studied). They found that lateralization of 13 mm was required to fully avoid impingement, but compared with the baseline positioning, this amount of lateralization resulted in a 20% increase in the muscle force (primarily the deltoid) required to abduct the shoulder to 90°. While providing important new information, the modeling approach used by Hoenecke et al was insufficient to evaluate what happens mechanically during impingement or how surgical technique may influence the development of stress at the interface between the polyethylene humeral component and the medial border of the scapula. By coupling finite element analysis with inverse dynamics modeling, stress, pressure, and strain can be computed. Knowledge of these mechanical metrics, which cannot be obtained using an inverse dynamics package alone, will be critical in understanding impingement and wear.

The long-term objective of our research is to better understand the mechanical tradeoffs in RSA so that implant design and placement can be optimized to avoid complications and improve longevity of the joint replacement. The specific objective of this study was to develop a complementary finite element and musculoskeletal modeling approach to better understand the effects of glenosphere medialization and lateralization on the resulting shoulder mechanics.

Methods

A finite element contact model of RSA patterned on the Tornier Aequalis RSA System (Tornier, Montbonnot, France) was created. By use of this baseline hardware design, varying configurations of medialization and lateralization were studied. The first configuration used medialized positioning of the glenosphere to reflect the constraints of pre-existing glenoid erosion, as is often seen in CTA patients. To study lateralization, the bony increased-offset (BIO) technique was modeled, in which a bone disk harvested from the humeral head is implanted behind the glenosphere.[3] This made it possible to use the same implant for all configurations and to thereby decrease the effect of confounding variables in our analysis. Four different lateralizations were studied using BIO grafts of different thicknesses: 2.5, 5, 7.5, and 10 mm.

The geometries of a 29-mm sized glenosphere, baseplate, and humeral implant were captured using a NextEngine 3D Laser Scanner HD (NextEngine, Santa Monica, CA, USA). Idealized geometric surfaces (cones, spheres, cylinders) were fit to the scans using Geomagic Studio Software (Geomagic USA, Morrisville, NC, USA). Scapular and humeral geometries were obtained by segmenting bony surfaces from computed tomography scans of the female cadaver from the Visible Human Project (National Library of Medicine, Bethesda, MD, USA [http://www.nlm.nih.gov/research/visible/visible_human.html]). The tracing was performed within OsiriX DICOM (Digital Imaging and Communications in Medicine) viewing software (Pixmeo, Geneva, Switzerland) using an Intuos pen tablet/display (Wacom Technology, Vancouver, WA, USA). Under the supervision of a shoulder surgeon (C.M.H.), the implants were placed in the bone models within Geomagic following manufacturer-recommended guidelines. Care was taken not to perforate the cortical boundary of the scapula with the central post of the glenosphere baseplate, and the humeral stem was centered within the shaft of the humerus.

Finite element meshes were generated using TrueGrid (version 2.3; XYZ Scientific Applications, Livermore, CA, USA). The scapular bone and polyethylene humeral insert were modeled with linearly elastic hexahedral elements, whereas the glenosphere, humeral cup backing and stem, and humerus were modeled as rigid shell elements. Modeling the substantially stiffer implant materials (glenosphere and humeral implant) and the non-contacting model features (humerus) as rigid enabled expeditious computational execution of the finite element analysis.

A complementary inverse dynamics model was created using SIMM (Software for Interactive Musculoskeletal Modeling; MusculoGraphics, Santa Rosa, CA, USA) to better understand the contribution of deltoid force to shoulder motion. The Stanford VA Upper Limb Model was used as the initial foundation.[16] The model geometries were then adjusted to reflect the RSA-implanted state, with minor additional adjustments in their positioning to accommodate the implanted components; the native scapular and humeral geometries were modified to include an RSA using surfaces generated from the finite element model. The matching geometries of the finite element and the inverse dynamics models were aligned within Geomagic software using its built-in iterative closest point algorithm. The final deviations between the corresponding surfaces were less than 0.5 mm.

All 5 lateralization configurations were subjected to 4 distinct finite element runs to test for impingement angle and 1 run to determine the deltoid force required to achieve scapular-plane elevation. For all runs, the humerus was initially placed in 40° of abduction (an abduction angle for which none of the cases exhibited impingement). Impingement was tested separately in the scapular and frontal planes. In addition, impingement was tested in models with a static (ie, stationary) scapula and in models with normal scapulothoracic motion (2:1 ratio of glenohumeral to scapulothoracic adduction).[8] The scapula is stationary in the static model. The scapula in the dynamic model moves with constant velocity proportional to the humeral adduction velocity. The humeral component was linked to the scapula by 2 springs located symmetrically about the plane of motion, representing the contribution of soft tissues to prevent dislocation and modeled with glenohumeral capsular ligament material properties as previously reported in the literature.[20,30,31] A load equivalent to the weight of an arm (40 N) was placed at the center of gravity of the humerus, estimated using anthropometric data. Then, the humerus was adducted until impingement occurred, where impingement was defined as generation of non-zero contact pressures on the humeral cup and scapular bone. The adduction angle of the arm at the moment of impingement (Fig. 1) was then recorded for all 4 tests (static scapula in the coronal plane, dynamic scapula in the coronal plane, static scapula in the scapular plane, and dynamic scapula in the scapular plane).

For the deltoid force runs, a series of slip-ring elements was added to represent the deltoid muscle group (Fig. 2). The slip-ring elements are specialty cable and pulley elements fixed to the humerus that represent the deltoid muscle as it wraps over the lateral surface of the humerus. The cable element was aligned with the humerus in the scapular plane to represent the resultant line of action of the deltoid. In the clinic, shoulder strength was tested 6 months postoperatively in RSA patients using a Micro-Fet2 wireless digital handheld dynamometer (Hoggan Scientific, Salt Lake City, UT, USA). For the test of interest, the patient was asked to place the arm in a handshake position, and the dynamometer was placed against the styloid process of the radius. The patient was then asked to raise the arm in the scapular plane with as much force as possible while the dynamometer was held fixed by a research assistant (Fig. 3). The forces generated by the patient over 3 trials were recorded and averaged, and the average force was converted using average anthropometric data into an equivalent moment of 22.5 Nm. In the deltoid force finite element analysis runs, this average moment was applied about the glenosphere center of rotation to rotate the humerus. The deltoid muscle cable and shoulder capsule ligament cables were restricted from extending, allowing the cables to generate tension and restrain adduction of the humerus. The reaction force acting in the deltoid muscle cable was then recorded.

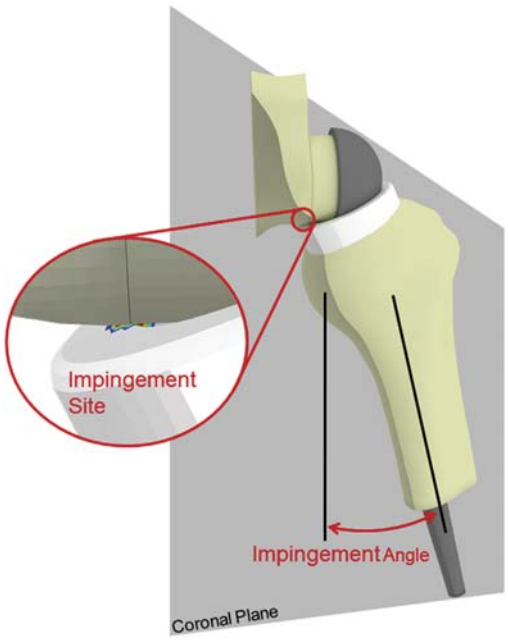

Figure 1 Methodology of impingement test. The humerus starts at 40° of elevation in the plane of interest, a load is placed on the distal end of the humerus, and the humerus is allowed to fall until impingement occurs. The inset shows the location of impingement, evidenced by contact pressure that has developed at the interface between the bone and polyethylene insert.

Results

Scapular-plane tests: static scapula

In the scapular plane, all lateralized glenospheres produced larger impingement-free ranges of motion when compared with the medialized model for the static scapula models. The medialized model achieved the smallest impingement-free range of motion, impinging with a 20.7° adduction deficit. However, the 2.5-mm model achieved the largest impingement-free range of motion, with only a 7.8°

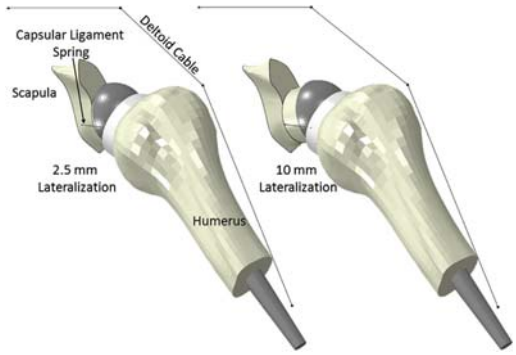

Figure 2 Models with 2.5 mm and 10 mm of lateralization. The deltoid element is displayed as a black line with black dots representing wrapping points.

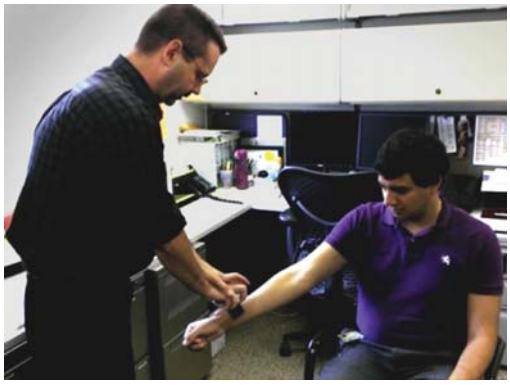

Figure 3 Example of muscle force clinical test. The subject is asked to produce maximal elevation force, and the clinical assistant restricts the motion of the subject with a MicroFet2 wireless digital handheld dynamometer. The force generated is then recorded.

adduction deficit. The results from all other lateralized models found slightly smaller impingement-free ranges of motion than for the 2.5-mm case, although all were larger than the medialized model. This finding is a result of the bony profile of the inferior aspect of the glenoid (which is not completely smooth). The shape and position of the inferior aspect of the scapula caused small changes in the range of motion due to the impingement location in this plane. The 2.5-mm and 7.5-mm lateralizations impinged medially and laterally, respectively, to a small bony protrusion, whereas the 5-mm lateralization impinged on the bony protrusion (Figs. 4 and 5). However, small differences (approximately 4°) in adduction deficit were seen because of this effect. At larger amounts of lateralization (7.5 mm and 10 mm), impingement occurred on the bone graft, not the native scapular neck.

Coronal-plane tests: static scapula

In the coronal plane, impingement-free range of motion was found to increase with increasing lateralization for the static scapula models. The medialized model impinged early at 40° of abduction. The 7.5-mm and 10-mm models produced the largest ranges of motion, with impingement occurring at 25.8° and 26.2°, respectively. Overall, greater lateralizations produced greater ranges of motion.

Scapular-plane tests: dynamic scapula

Larger impingement-free ranges of motion were found for the dynamic scapular-plane test than for the static scapular-plane test. With the dynamic scapula, the scapular-plane test found that the largest impingement-free range of motion occurred with the most lateralized (10-mm) model (no adduction deficit) and the smallest impingement-free range of motion occurred in the medialized 5-mm model (20.7° adduction deficit). In addition, no impingement occurred before the arm was adducted completely to the chest wall (assuming a thin person) for all lateralized models (2.5, 5, 7.5, and 10 mm). When we compared the static and dynamic tests, the scapular-plane tests produced similar differences in impingement-free range of motion between analogous lateralizations.

Coronal-plane tests: dynamic scapula

Similar to the scapular-plane tests, the dynamic coronal-plane test found greater ranges of motion before impingement when compared with the static coronal-plane test. This test found that greater lateralization always produced greater range of motion. The medialized model impinged immediately at 40° of abduction, comparable with the static coronal-plane test, and the 2 greatest lateralizations (7.5 mm and 10 mm) produced the smallest adduction deficits (1.5° and 0°, respectively). Greater variability was seen between different lateralization models in the coronal plane. Smaller differences in impingement-free range of motion were seen at smaller lateralizations, and greater differences were seen at larger lateralizations. The smallest differences were seen at 5 mm of medialization and 2.5 mm of lateralization (0° and 2° between static and dynamic models, respectively), and the largest difference was seen at 10 mm of lateralization (26.2°).

Deltoid force test

In the deltoid force test, models with larger lateralizations required greater deltoid force to resist the identical external loads. The medialized model and the 2.5-mm lateralized model required similar deltoid forces (546 N and 553 N, respectively), with all other lateralized models requiring larger forces (580 N, 616 N, and 660 N). The results of these trials are shown in Table I and Figure 6.

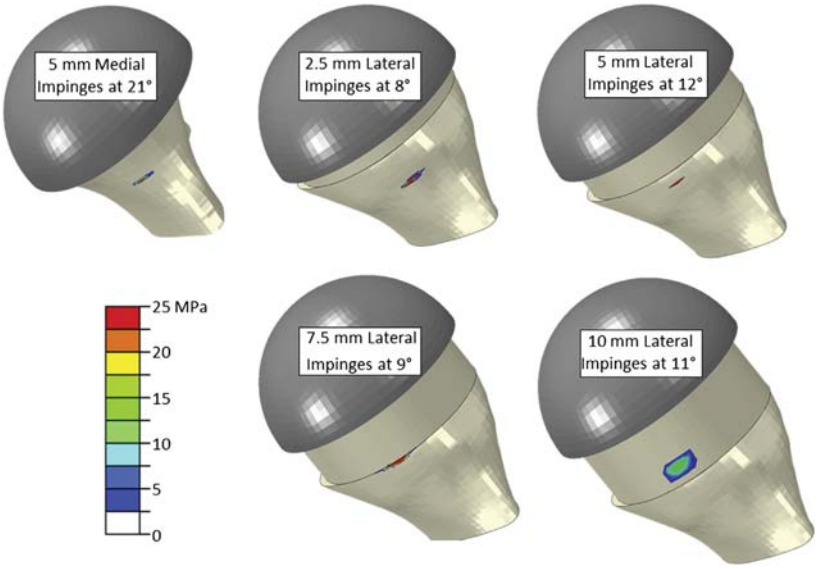

Figure 4 Scapular impingement sites of all models for static scapular-plane range-of-motion tests. The models with 5 mm of medialization and 2.5 mm of lateralization impinge the most medially, and the model with 10 mm of lateralization impinges the most laterally. The most lateral model impinges on the bony increased-offset graft, whereas all other lateralization models impinge on the inferior aspect of the scapula.

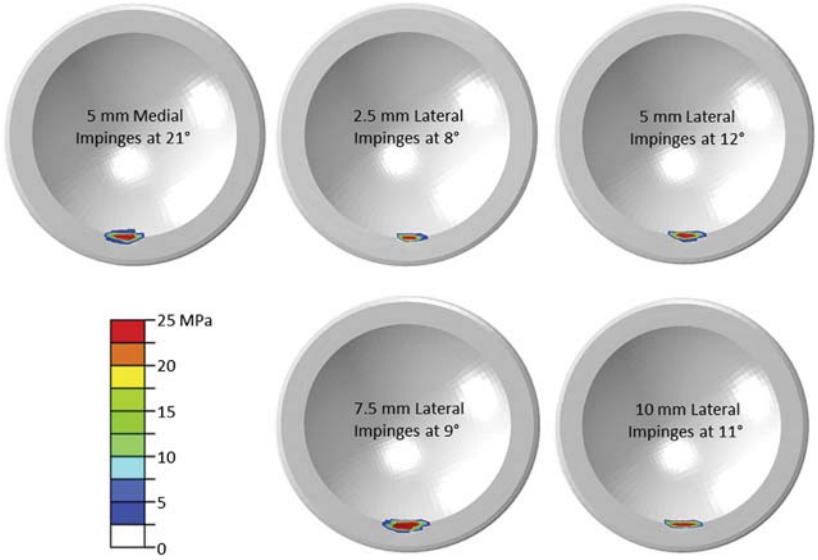

Figure 5 Polyethylene impingement sites of all models for static scapular-plane range-of-motion tests. The impingement site location, contact area, and contact stress values are similar across all models.

Discussion

As hypothesized, increased lateralization produced larger impingement-free range of motion. In the static models, there was an increasing benefit with progressively increasing amounts of lateralization. In the model with scapulothoracic motion, the benefit of lateralization was maximized with 2.5 mm of lateralization in the scapular plane due to bony

Table I Results of impingement angle and deltoid muscle force test for all lateralization models

Implantation	Impingement angle, °				Deltoid force test, N
	Scapular plane		Coronal plane		
	Static	Dynamic	Static	Dynamic	
−5 mm	20.7	11.5	40.0	40.0	546
2.5 mm	7.8	0	36.1	34.1	553
5 mm	12.4	0	30.8	8.6	583
7.5 mm	9.0	0	25.8	1.5	618
10 mm	10.7	0	26.2	0.0	660

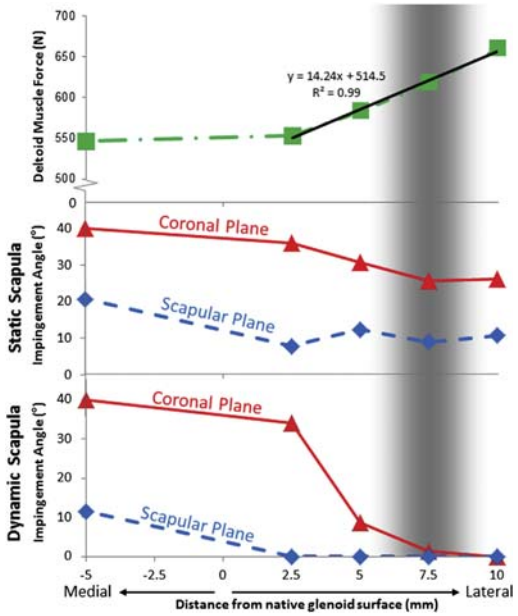

Figure 6 Results of impingement angle and deltoid muscle force test for all models. The top graph depicts the deltoid muscle force test results, the middle graph displays the range of motion results with the static scapula models, and the bottom graph depicts the range of motion results with the dynamic scapula models.

prominences on the undersurface of the inferior glenoid, and there was no further impingement beyond this. However, significant impingement was still present at 2.5 mm of lateralization in the coronal plane. This finding is important to recognize because impingement can occur at different points for different motions, and a variety of shoulder motions should be studied to fully understand when impingement occurs and what is the optimal amount of lateralization. There was significant impingement in both models when the glenoid was medialized to simulate the erosion that occurs with arthritis. It will be important for clinicians to recognize this and consider lateralization most strongly when this scenario is present.

The tests of the force required by the deltoid to elevate the arm demonstrated the tradeoff with lateralization, with increasing force being required by the deltoid with increasing lateralization (14.25 N per millimeter of lateralization between 2.5 and 10 mm). This result signifies that every 1 mm of lateralization requires an additional 2.6% of deltoid force. Our results show that the optimal amount of lateralization in the static scapula model is approximately 7.5 mm. In the dynamic scapula model, 7.5 mm and 10 mm both produce large impingement-free ranges of motion; however, there is a 6.8% difference in deltoid force required between these. The optimal balance between decreasing impingement and deltoid strength will need to be further studied.

This study only modeled normal versus zero scapulothoracic motion. However, patients with CTA leading to RSA often exhibit dysfunctional scapulothoracic motion that falls in between these ranges. In one recent study, scapular motion was found to account for all abduction with no motion occurring at the glenohumeral joint for patients with pseudoparalytic shoulders.[33] In this scenario, the need for lateralization is amplified. If the patient has impingement at low ranges of motion and healthy scapular motion is not restored after RSA, impingement may occur throughout the entire range of motion, leading to a greater likelihood of scapular notching.

We used the BIO technique for our modeling because it allowed us to use the same implants for lateralized and medialized models, as well as to look at differing amounts of lateralization because we were not constrained by existing glenosphere designs. This removes potential confounding factors that occur with studies that use different implants. We are not promoting use of the BIO technique in this study but are simply using this to vary the amount of lateralization without having to change implants.

The strengths of our finite element modeling approach are that it uses a fully 3-dimensional model, which improves on studies in the literature that performed tests only in a single plane. We also have included scapulothoracic motion, which has been shown to make a significant difference over a static scapula. The finite element modeling approach will allow us to explore contact stresses that develop at the site of impingement during whatever motions are modeled. The present weaknesses include only having a simplified deltoid and no other shoulder musculature. This simplified model is more than sufficient to answer the questions in this study, but additional complexity will be required to answer future questions. We have also limited confounding effects of different implant systems by using the same implants in each group; however, the results may not be generalizable to other implant systems. Other studies have varied the implants between groups, and one cannot tell if the changes they are detecting are from lateralization or from other component differences.

Conclusion

The combined finite element and inverse dynamics modeling approach provides useful information for assessing the mechanics of impingement in RSA. Such an approach can guide the selection of an ideal glenosphere lateralization to minimize impingement while maximizing the mechanical advantage of the deltoid. The resulting lateralization recommendations can be considered during surgical planning, taking into account the body habitus and scapulothoracic motion of the patient, and integrated into future implant designs.

Disclaimer

This study was funded in part by a grant from the Orthopaedic Research and Education Fund.

The authors, their immediate families, and any research foundations with which they are affiliated have not received any financial payments or other benefits from any commercial entity related to the subject of this article.

References

1. Boileau P, Baque F, Valerio L, Ahrens P, Chuinard C, Trojani C. Isolated arthroscopic biceps tenotomy or tenodesis improves symptoms in patients with massive irreparable rotator cuff tears. J Bone Joint Surg Am 2007;89:747-57. http://dx.doi.org/10.2106/JBJS.E.01097
2. Boileau P, Chuinard C, Roussanne Y, Neyton L, Trojani C. Modified latissimus dorsi and teres major transfer through a single deltopectoral approach for external rotation deficit of the shoulder: as an isolated procedure or with a reverse arthroplasty. J Shoulder Elbow Surg 2007;16:671-82. http://dx.doi.org/10.1016/j.jse.2007.02.127
3. Boileau P, Moineau G, Roussanne Y, O'Shea K. Bony increased-offset reversed shoulder arthroplasty: minimizing scapular impingement while maximizing glenoid fixation. Clin Orthop Relat Res 2011;469:2558-67. http://dx.doi.org/10.1007/s11999-011-1775-4
4. Boileau P, Sinnerton RJ, Chuinard C, Walch G. Arthroplasty of the shoulder. J Bone Joint Surg Br 2006;88:562-75. http://dx.doi.org/10.1302/0301-620X.88B5.16466
5. Boileau P, Watkinson D, Hatzidakis AM, Hovorka I. Neer Award 2005: the Grammont reverse shoulder prosthesis: results in cuff tear arthritis, fracture sequelae, and revision arthroplasty. J Shoulder Elbow Surg 2006;15:527-40. http://dx.doi.org/10.1016/j.jse.2006.01.003
6. Day J, Paxton ES, Lau E, Abboud J, Gordon V, Williams GR. Use of reverse total shoulder arthroplasty in the Medicare population. J Shoulder Elbow Sur 2015;24:766-72. http://dx.doi.org/10.1016/j.jse.2014.12.023
7. Day JS, MacDonald DW, Olsen M, Getz C, Williams GR, Kurtz SM. Polyethylene wear in retrieved reverse total shoulder components. J Shoulder Elbow Surg 2012;21:667-74. http://dx.doi.org/10.1016/j.jse.2011.03.012
8. de Groot JH, Brand R. A three-dimensional regression model of the shoulder rhythm. Clin Biomech 2001;16:735-43.
9. Drake GN, O'Connor DP, Edwards TB. Indications for reverse total shoulder arthroplasty in rotator cuff disease. Clin Orthop Relat Res 2010;468:1526-33. http://dx.doi.org/10.1007/s11999-009-1188-9
10. Ecklund KJ, Lee TQ, Tibone J, Gupta R. Rotator cuff tear arthropathy. J Am Acad Orthop Surg 2007;15:340-9.
11. Ek ET, Neukom L, Catanzaro S, Gerber C. Reverse total shoulder arthroplasty for massive irreparable rotator cuff tears in patients younger than 65 years old: results after five to fifteen years. J Shoulder Elbow Surg 2013;22:1199-208. http://dx.doi.org/10.1016/j.jse.2012.11.016
12. Feeley BT, Gallo RA, Craig EV. Cuff tear arthropathy: current trends in diagnosis and surgical management. J Shoulder Elbow Surg 2009;18:484-94. http://dx.doi.org/10.1016/j.jse.2008.11.003
13. Guery J, Favard L, Sirveaux F, Oudet D, Mole D, Walch G. Reverse total shoulder arthroplasty. Survivorship analysis of eighty replacements followed for five to ten years. J Bone Joint Surg Am 2006;88:1742-7. http://dx.doi.org/10.2106/JBJS.E.00851
14. Hoenecke HR Jr, Flores-Hernandez C, D'Lima DD. Reverse total shoulder arthroplasty component center of rotation affects muscle function. J Shoulder Elbow Surg 2014;23:1128-35. http://dx.doi.org/10.1016/j.jse.2013.11.025
15. Holcomb JO, Cuff D, Petersen SA, Pupello DR, Frankle MA. Revision reverse shoulder arthroplasty for glenoid baseplate failure after primary reverse shoulder arthroplasty. J Shoulder Elbow Surg 2009;18:717-23. http://dx.doi.org/10.1016/j.jse.2008.11.017
16. Holzbaur KR, Murray WM, Delp SL. A model of the upper extremity for simulating musculoskeletal surgery and analyzing neuromuscular control. Ann Biomed Eng 2005;33:829-40. http://dx.doi.org/10.1007/s10439-005-3320-7
17. Li X, Knutson Z, Choi D, Lobatto D, Lipman J, Craig EV, et al. Effects of glenosphere positioning on impingement-free internal and external rotation after reverse total shoulder arthroplasty. J Shoulder Elbow Surg 2013;22:807-13. http://dx.doi.org/10.1016/j.jse.2012.07.013
18. Martin TG, Iannotti JP. Reverse total shoulder arthroplasty for acute fractures and failed management after proximal humeral fractures. Orthop Clin North Am 2008;39:451-7. http://dx.doi.org/10.1016/j.ocl.2008.06.006
19. Mavrogenis AF, Mastorakos DP, Triantafyllopoulos G, Sakellariou VI, Galanis EC, Papagelopoulos PJ. Total scapulectomy and constrained reverse total shoulder reconstruction for a Ewing's sarcoma. J Surg Oncol 2009;100:611-5. http://dx.doi.org/10.1002/jso.21340
20. O'Brien SJ, Neves MC, Arnoczky SP, Rozbruck SR, Dicarlo EF, Warren RF, et al. The anatomy and histology of the inferior glenohumeral ligament complex of the shoulder. Am J Sports Med 1990;18:449-56.
21. Rittmeister M, Kerschbaumer F. Grammont reverse total shoulder arthroplasty in patients with rheumatoid arthritis and nonreconstructible rotator cuff lesions. J Shoulder Elbow Surg 2001;10:17-22.
22. Roche CP, Stroud NJ, Flurin PH, Wright TW, Zuckerman JD, DiPaola MJ. Reverse shoulder glenoid baseplate fixation: a comparison of flat-back versus curved-back designs and oval versus circular designs with 2 different offset glenospheres. J Shoulder Elbow Surg 2014;23:1388-94. http://dx.doi.org/10.1016/j.jse.2014.01.050
23. Sadoghi P, Leithner A, Vavken P, Holzer A, Hochreiter J, Weber G, et al. Infraglenoidal scapular notching in reverse total shoulder replacement: a prospective series of 60 cases and systematic review of the literature. BMC Musculoskelet Disord 2011;12:101. http://dx.doi.org/10.1186/1471-2474-12-101
24. Simovitch RW, Zumstein MA, Lohri E, Helmy N, Gerber C. Predictors of scapular notching in patients managed with the Delta III reverse total shoulder replacement. J Bone Joint Surg Am 2007;89:588-600. http://dx.doi.org/10.2106/JBJS.F.00226
25. Sirveaux F, Favard L, Oudet D, Huquet D, Walch G, Mole D. Grammont inverted total shoulder arthroplasty in the treatment of glenohumeral osteoarthritis with massive rupture of the cuff.

Results of a multicentre study of 80 shoulders. J Bone Joint Surg Br 2004;86:388-95. http://dx.doi.org/10.1302/0301-620x.86b3.14024
26. Smith CD, Guyver P, Bunker TD. Indications for reverse shoulder replacement: a systematic review. J Bone Joint Surg Br 2012;94:577-83. http://dx.doi.org/10.1302/0301-620X.94B5.27596
27. Stroud N, DiPaola MJ, Flurin PH, Roche CP. Reverse shoulder glenoid loosening: an evaluation of the initial fixation associated with six different reverse shoulder designs. Bull Hosp Jt Dis 2013;71(Suppl 2):S12-7.
28. Wall B, Nove-Josserand L, O'Connor DP, Edwards TB, Walch G. Reverse total shoulder arthroplasty: a review of results according to etiology. J Bone Joint Surg Am 2007;89:1476-85. http://dx.doi.org/10.2106/JBJS.F.00666
29. Wall B, Walch G. Reverse shoulder arthroplasty for the treatment of proximal humeral fractures. Hand Clin 2007;23:425-30. http://dx.doi.org/10.1016/j.hcl.2007.08.002. v-vi.
30. Warner JJ, Deng XH, Warren RF, Torzilli PA. Static capsuloligamentous restraints to superior-inferior translation of the glenohumeral joint. Am J Sports Med 1992;20:675-85.
31. Weiss JA, Gardiner JC. Computational modeling of ligament mechanics. Crit Rev Biomed Eng 2001;29:303-71.
32. Wierks C, Skolasky RL, Ji JH, McFarland EG. Reverse total shoulder replacement: intraoperative and early postoperative complications. Clin Orthop Relat Res 2009;467:225-34. http://dx.doi.org/10.1007/s11999-008-0406-1
33. Wieser K, Rahm S, Schubert M, Fischer MA, Farshad M, Gerber C, et al. Fluoroscopic, magnetic resonance imaging, and electrophysiologic assessment of shoulders with massive tears of the rotator cuff. J Shoulder Elbow Surg 2015;24:288-94. http://dx.doi.org/10.1016/j.jse.2014.05.026
34. Zumstein MA, Pinedo M, Old J, Boileau P. Problems, complications, reoperations, and revisions in reverse total shoulder arthroplasty: a systematic review. J Shoulder Elbow Surg 2011;20:146-57. http://dx.doi.org/10.1016/j.jse.2010.08.001

APPENDIX B: CADAVERIC VALIDATION OF A FINITE ELEMENT MODELING APPROACH FOR STUDYING SCAPULAR NOTCHING IN REVERSE SHOULDER ARTHROPLASTY

Journal of Biomechanics 49 (2016) 3069–3073

Contents lists available at ScienceDirect

Journal of Biomechanics

journal homepage: www.elsevier.com/locate/jbiomech
www.JBiomech.com

Short communication

Cadaveric validation of a finite element modeling approach for studying scapular notching in reverse shoulder arthroplasty

Vijay N. Permeswaran [a,b,*], Jessica E. Goetz [a,b], M. James Rudert [a], Carolyn M. Hettrich [a], Donald D. Anderson [a,b]

[a] Department of Orthopaedics and Rehabilitation, The University of Iowa, USA
[b] Department of Biomedical Engineering, The University of Iowa, USA

ARTICLE INFO

Article history:
Accepted 8 July 2016

Keywords:
Reverse shoulder arthroplasty
Finite element analysis
Validation
Scapular notching

ABSTRACT

Cadaveric experiments were undertaken to validate a finite element (FE) modeling approach for studying impingement-related scapular notching in reverse shoulder arthroplasty (RSA). The specific focus of the validation was contact at the site of impingement between the humeral polyethylene component and the inferior aspect of the scapula during an adduction motion. Lateralization of the RSA center of rotation was varied because it has been advocated clinically to reduce impingement and presumably decrease the risk of scapular notching. Tekscan sensors were utilized to directly measure contact stress at the impingement site, and FE was used to compute contact stresses. Favorable agreement was seen between physically measured and FE-computed impingement site location (within one sensing element of the Tekscan sensor) and contact loads (mean absolute difference of 14.9%). Contact stresses and contact areas were difficult to compare directly due to the disparate spatial resolutions of the Tekscan sensor and the FE model. FE-computed contact at the impingement site was highly focal, with a total contact area comparable to the area of an individual Tekscan sensing element. The good agreement between the physically measured and FE-computed contact data (i.e., contact load and location) support the use of FE modeling as a tool for computationally testing the efficacy of changing various surgical variables associated with RSA.

1. Introduction

Reverse shoulder arthroplasty (RSA) aims to relieve pain and restore motion in a rotator cuff-deficient shoulder by replacing the humeral head with a polyethylene cup and the glenoid with a metallic glenosphere, thereby reversing the anatomy of the glenohumeral joint (Gerber et al., 2009). Early clinical results of RSA showed promise in restoring function to rotator cuff-deficient patients (Frankle et al., 2006; Gerber et al., 2009; Nyffeler et al., 2004; Werner et al., 2013; Wierks et al., 2009). Unfortunately, high short- and mid-term complication rates have been reported after RSA, most commonly involving scapular notching – a localized loss of bone in the inferior medial neck of the scapula resulting from humeral component impingement with the scapula when the arm is adducted (Frankle et al., 2005; Nyffeler et al., 2004; Walch et al., 2012).

A common technique used to prevent scapular notching is lateralization of the RSA center of rotation (Boileau et al., 2011), although modifying the shoulder center of rotation can influence the effective muscle strength, range of motion, and contact stress at any impingement site. In an earlier study, we used a finite element (FE) modeling approach to study the effects of surgical lateralization of RSA hardware on impingement-free range of motion and deltoid muscle force requirements (Hettrich et al., 2015). Greater lateralization permitted a greater range of humeral adduction before impingement. The FE model also predicted that the impingement site would develop large and highly focal contact stresses (Hettrich et al., 2015).

In the present study we aimed to physically validate the FE-computed location of impingement, the contact area, and the contact stress values on cadaveric shoulder specimens.

2. Methods

2.1. Physical testing

CT scans were obtained for two cadaveric shoulder specimens from the same female donor (age at death of 92 years, mass of 54.5 kg) prior to and following implantation of an RSA system. All soft tissues were dissected from the scapulae and humeri. The medial region of each scapula was potted in poly-methylmethacrylate

* Correspondence to: Orthopaedic Biomechanics Laboratory 2181 Westlawn Building Iowa City, IA 52242. Fax: +1 319 335 7530.
E-mail address: vijay-permeswaran@uiowa.edu (V.N. Permeswaran).

http://dx.doi.org/10.1016/j.jbiomech.2016.07.007
0021-9290/

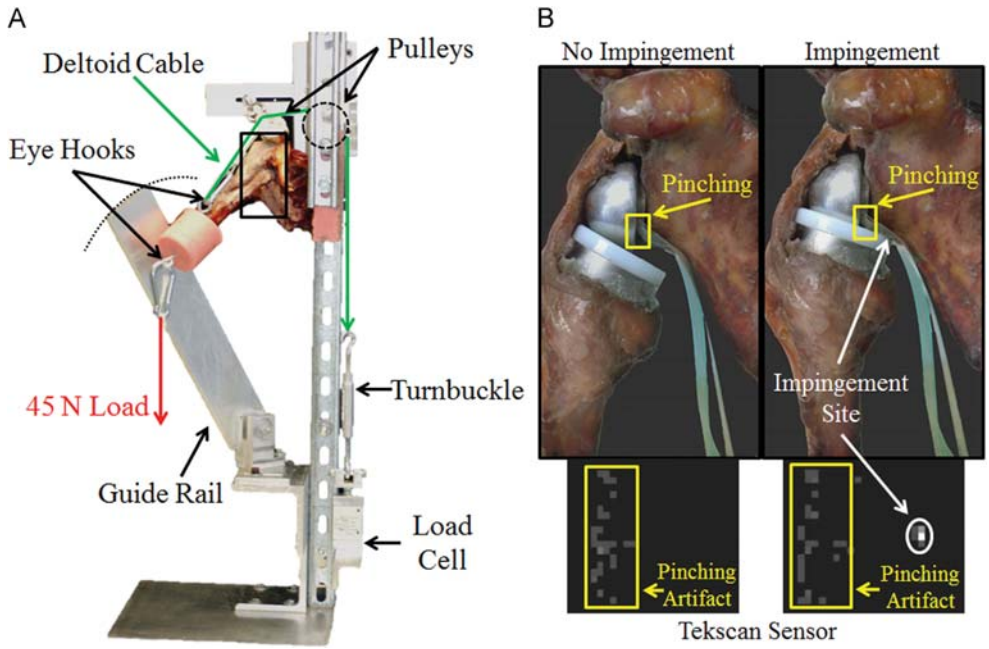

Fig. 1. (A) Physical validation loading frame diagram with (B) Tekscan sensor alignment and positioning. The humerus was placed at impingement and loaded with 22.5-N. Pressure recordings were made before and after loading.

(PMMA) bone cement and bolted to a metallic test frame, orienting the scapula with 0° of upward rotation, elevation, and protraction (Fig. 1A). Patients possessing cuff pathology indicated for RSA exhibit highly dysfunctional scapulo–humeral rhythm, and little data are available describing their scapular function post-operatively (Wieser et al., 2015). This lack of RSA patient scapular kinematic knowledge led us to model the scapula as fixed, matching previous FE model conditions (Hettrich et al., 2015). The humeri were cut 5 cm distal to the deltoid insertion and potted in PMMA. One eye-hook was inserted into the inferior region of the bone cement to facilitate loading and another into the PMMA near the deltoid insertion (Fig. 1A). A cable representing the deltoid was attached to the eye-hook near the deltoid tendon insertion site and routed through two pulleys to redirect the line of action of the cable to a load cell measuring tension. An inline turnbuckle generated tension in the deltoid cable and served to control humeral position.

An Aequalis RSA system (Tornier, Amsterdam, Netherlands) similar to other Grammont style RSA systems was implanted in each of the shoulder specimens by a fellowship-trained shoulder surgeon using a modified BIO technique (Boileau et al., 2011). Rather than bone, metal spacers of varying thickness (2.5, 5, and 7.5 mm) were placed behind the glenosphere to study multiple clinically relevant implant lateralizations for both specimens (Hettrich et al., 2015).

To measure contact stress at the notching impingement site during an adduction motion, a humerus constrained to the coronal plane was loaded with a 22.5-N weight representing the average weight of a human forearm (Chaffin et al., 2006). A calibrated Tekscan pressure sensor (Model #5033, Tekscan, South Boston, MA) was used to measure the contact stress between the humeral cup and the inferior glenoid. This sensor was selected for its high spatial resolution (0.83 mm x 0.83 mm sensing elements [sensels]). To secure the sensor for testing and to minimize wrinkling, each sensor was trimmed into a narrow tab that fit between the lateralization spacers and the glenosphere with minimal extraneous material. Trimming was carefully performed between the leads to ensure the remaining portion of the sensor could provide optimal coverage of the inferior glenoid with full resolution of the sensor. The deltoid cable was tightened using the inline turnbuckle until maximal impingement contact stress was recorded. Any additional adjustment caused humeral abduction and a decrease in contact stress.

2.2. Computational modeling

The bony geometries of each specimen were segmented from pre- and post-implantation CT scans using Seg3D software (CIBC, Salt Lake City, UT). Post-segmentation bone surface models were smoothed to remove voxel surface artifacts and decimated to approximately 100,000 elements using Geomagic Studio Software (3DSystems, Rock Hill, SC). The full FE model included the lateral scapula, the specimen's specific RSA implantation, and the proximal humerus. Hexahedral FE meshes of each lateralization for both specimens were created using TrueGrid software (XYZ Scientific Applications, Livermore, CA). Resulting meshes consisted of approximately 18,000 elements, with a characteristic element edge length of approximately 1 mm in the inferior scapula region. The glenosphere and humeral stem were modeled as rigid, and the bone and polyethylene cup were modeled as linear elastic materials (Hettrich et al., 2015). Slipring elements representing the deltoid and two nonlinear spring elements with glenohumeral capsular ligament properties representing the soft tissue restraint were also introduced (O'Brien et al., 1990; Warner et al., 1992; Weiss and Gardiner, 2001). Slipring elements are specialized connectors consisting of two nodes acting as pulleys and an element acting as a connecting cable. FE analyses were performed using Abaqus/Explicit 6.14-2 (Dassault Systêmes, Vèlizy-Villacoublay, France).

The FE model was loaded using a 22.5-N inferiorly directed load placed on the distal end of the humerus model. The humerus started in 40° of coronal plane abduction and was lowered into impingement. Because Abaqus/Explicit models impingement as a dynamic event, a restart analysis was necessary to obtain a static impingement event similar to the physical testing. The restart was performed beginning from the time interval just after impingement; the humerus was restrained at the impingement position by fixing the deltoid cable, allowing the initial dynamic contact event to relax to a steady state.

Initial global models oftentimes computed contact occurring at just one node. Therefore, in order to obtain higher resolution of the impingement site than the global model could provide, a highly refined submodel was created for each testing case. Upon completion of the global FE model runs, scapular elements reporting contact in the global model were exported and served as the geometric boundaries of a submodel. These small regions of the scapula and humeral cup were meshed with higher refinement (approximate element edge length = 0.1 mm and roughly 46,000 elements) to study impingement site contact, with nodal displacements computed in the global model applied to corresponding nodes in the submodel.

2.3. Validation comparison

Direct spatial comparisons of the FE-computed vs. the Tekscan-measured contact stress distribution on the scapula were performed in MATLAB (MathWorks, Natick, MA). Two corroborating methods were used to spatially register the Tekscan sensor to the FE model. First, the Tekscan sensor recorded the location of pinching between the baseplate and glenosphere (Fig. 1B). A Tekscan sensor surface was generated by calculating the length of the sensor residing over bone and meshed within TrueGrid, with nodal spacing corresponding to physical sensel spacing. To determine this length, the number of rows of sensels from the most medial row at the pinch point to the medial end of the sensor was counted. That

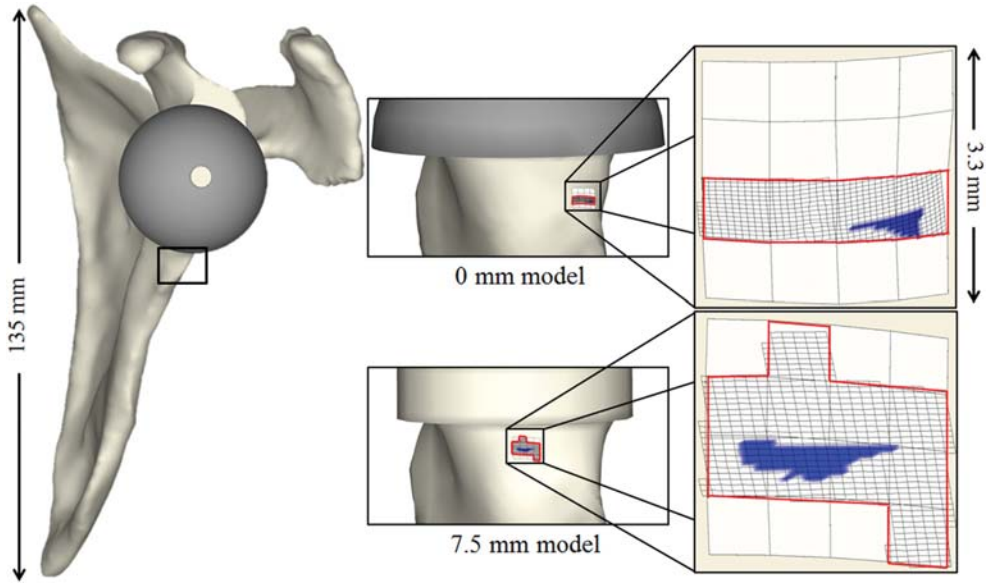

Fig. 2. A lateral view of the scapula following RSA with insets to show scale and location of the impingement site. The contact of the FE submodel is shown as a blue contact patch. Tekscan sensels detecting contact are outlined in red. Finite element mesh edges for the submodel are shown in the right images. (For interpretation of the references to color in this figure legend, the reader is referred to the web version of this article.)

Table 1
Impingement contact stress results.

Impingement contact stress results							
Specimen	**Lateralization (mm)**	**Load recovered (N)**		**FE contact area (mm^2)**	**Contact pressure (MPa)**		
					FE	**Tekscan**	
		FE	**Tekscan**		**Mean**	**Mean**	**Max**
1	0	45.5	40.5	0.99	14.4	9.8	16.2
	2.5	49	45.5	0.65	10.9	8.3	11.2
	5	47.3	45	0.83	17.6	7.2	17
2	0	21.2	31.8	0.91	5.7	2.2	2.5
	2.5	27.7	30.7	0.94	10.2	2.6	3.1
	5	45.5	37.2	0.84	16	4.2	7.6
	7.5	46.6	41	0.72	17.2	5.5	8
Mean		**40.4**	**38.8**	**0.84**	**13.1**	**5.7**	**9.4**

number was multiplied by the length of one sensel and the amount of lateralization was subtracted out to determine the length of the sensor residing over bone. Spurious Tekscan contact stress values attributed to pinching of the sensor were thresholded from contact stress analysis. Contact stress data were mapped to the Tekscan sensor surface, and all submodel finite elements existing in the same spatial position as the Tekscan sensor were retained for analysis (Fig. 2). The mean and maximum values of the FE-computed contact stresses in the extracted elements were compared to the mean and maximum of all thresholded Tekscan sensor values. The load acting over the contact patch was also compared between the physical experiments and the FE models.

3. Results

The data from the 7.5 mm lateralization for specimen 1 had to be discarded, as the contact patch extended off the Tekscan sensor. The impingement site of the FE submodel did, however, correlate well with the partial impingement patch recorded by the Tekscan sensor. For the remaining seven lateralization experiments, load recovery was similar between the physical and experimental models (Table 1). All but two sets of FE and physical model load recovery values were within 15% of each other, and the mean absolute difference between the FE-computed and Tekscan-measured loads was 14.9% across all implant lateralizations (Table 1). The average load recovered for the FE submodels was 40.4 N, while the average Tekscan sensor load recovered for the corresponding models was 38.8 N.

The FE models accurately predicted impingement location when compared to the Tekscan sensor values (Fig. 3). Generally, the FE-computed contact patches were highly concentrated. The FE submodels predicted contact areas between 0.65 and 0.99 mm^2, while the resolution of a single Tekscan sensel is about 0.70 mm^2. Because of this relatively coarse Tekscan sensor spatial resolution, it was difficult to directly compare contact area between the FE models and the physical experiments. The mean of all FE contact stresses was 13.1 MPa, the mean of all Tekscan contact stresses was 5.7 MPa, and the mean of all maximum Tekscan contact stresses was 9.4 MPa (Table 1).

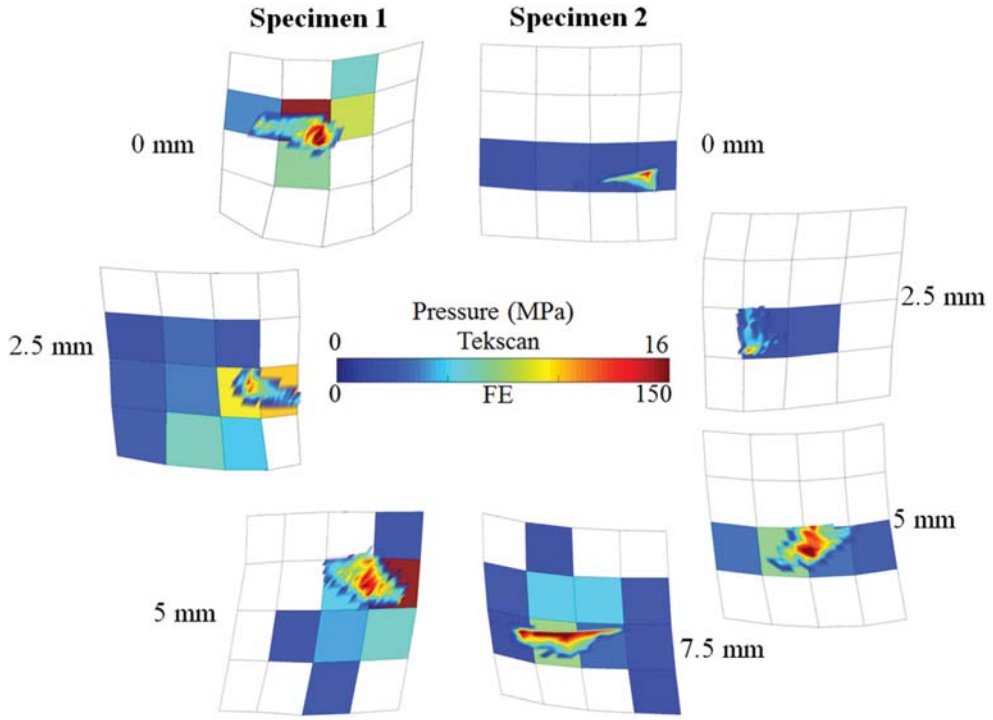

Fig. 3. Composite contact pressure plots for all lateralizations and specimens. The non-zero FE submodel values are superimposed over a 4x4 sensel Tekscan array. Thresholded Tekscan values are plotted in the color corresponding to the pressure value, and values under the threshold are plotted white.

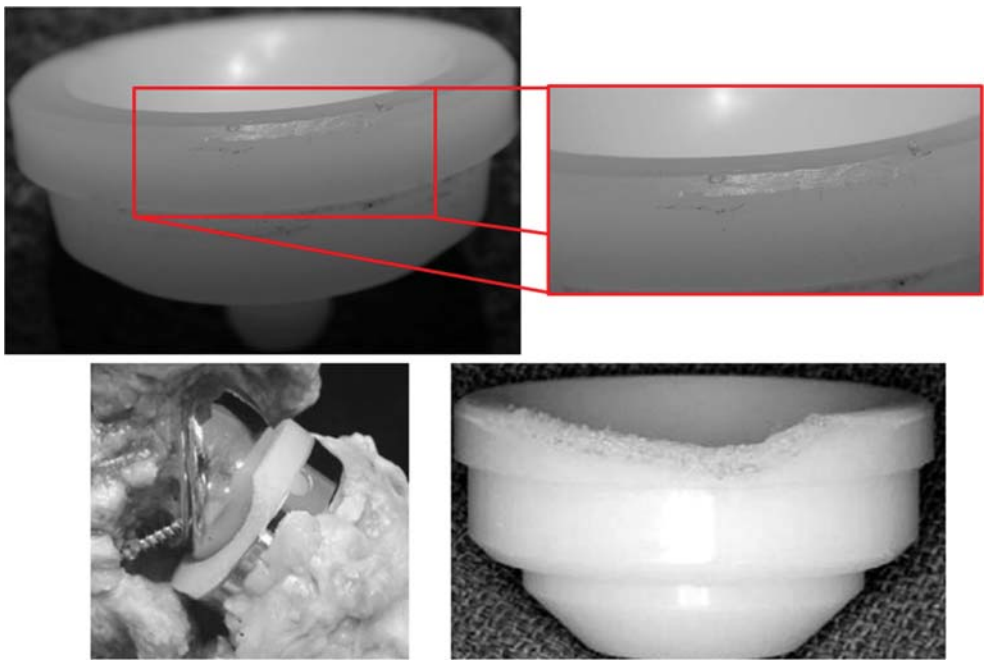

Fig. 4. The top images were taken of the tested humeral cup with small scrapes and scratches shown from loading. The bottom left and right images show humeral cup retrievals of RSA following scapular notching. [These images are reprinted here with permission from (Nyffeler et al., 2004) and (Oh and Choi, 2013).].

4. Discussion

In this study, we aimed to physically measure contact stress at the site of impingement to validate contact mechanics (contact area, contact location, load recovery, and contact stress) computed by an FE model developed to study scapular notching (Hettrich et al., 2015). The contact area was found to be extremely small, making physical measurements difficult. Load recovery values and impingement locations were found to compare favorably.

The similarity of the load recovery and contact data lends credence to the FE analysis. The average FE submodel and Tekscan load recovery measurements were within 2 N. In addition, the FE-computed contact locations agreed with those measured to within one sensel. Finally, the contact area of all the FE submodels was very similar (within 0.3 mm^2) to the area of one Tekscan sensor sensel. Therefore, we compared the maximum Tekscan contact stresses to the mean FE submodel contact stresses. These values were very similar; the average FE submodel contact stress was less than 4 MPa greater than the maximum Tekscan contact stress (13.1 vs. 9.4 MPa).

Interestingly, the contact stress values calculated in the FE analysis were found to exceed the compressive yield stress value of polyethylene (Takeuchi et al., 1995), suggesting that plastic deformation may occur at the impingement site. In fact, we found evidence of plastic deformation at the beveled edge of the tested humeral polyethylene (Fig. 4), similar in location to polyethylene cups studied in scapular notching retrieval studies (Nyffeler et al., 2004; Oh and Choi, 2013).

This work is not without limitations. The task of validating the FE contact variables with physical contact stress measurements was difficult, primarily because the contact was highly focal. Pressure-sensitive film was not used because of impingement site movement during load application, which would produce a broad smearing artifact. Instead, a Tekscan sensor was used for this work because of its real-time nature and ability to isolate steady-state loading. While the area of contact would ideally be many times larger than the resolution of a Tekscan sensel, this was not possible given the extremely focal impingement of the polyethylene on the narrow scapula. Furthermore, a single implant design was tested. Generalization of these results to other non-Grammont style implant systems with different humeral implant designs (onlay vs. inlay socket, varying neck-shaft angle, etc.) should be done with caution as changes to these parameters would most likely change the contact mechanics of the impingement site. Finally, the focus of the study was to validate the previously published model and not to reproduce precise physiological loadings, so care should be taken in extrapolating these results to in-vivo situations.

In conclusion, we have presented the experimental validation of an FE model developed for studying impingement related to notching in RSA. We conducted tests to determine the site of impingement during humeral adduction, as well as contact pressure at the impingement site, using a calibrated Tekscan sensor on two shoulder specimens with varying amounts of implant lateralization. Comparisons of contact stress, contact area, and contact location in physical experiments were made against a previously published FE RSA model (Hettrich et al., 2015). The FE model predicted highly focal contact areas due to the sharp edge-on-edge contact present during an impingement event. Although Tekscan sensor data were unable to capture these highly focal impingement events, macroscopic measures of both the physical and FE models were in good agreement, thereby validating the model.

Conflict of interest statement

The authors involved in this study currently have no conflicts of interest.

Acknowledgments

The shoulder implants used in this study were generously loaned to us by Tornier. The assistance of Jessica Mosqueda and Daniel Bonthius in performing the experiments is gratefully acknowledged. This study was aided by a new investigator grant from Orthopaedic Research and Education Foundation, United States (grant number 14-012).

References

Boileau, P., Moineau, G., Roussanne, Y., O'Shea, K., 2011. Bony increased-offset reversed shoulder arthroplasty: minimizing scapular impingement while maximizing glenoid fixation. Clin. Orthop. Relat. Res. 469, 2558–2567.
Chaffin, D.B., Andersson, Gunnar, B.J., Nartin, Bernard, J., Martin, 2006. Occupational Biomechanics, 4th ed. Wiley-Interscience, Hoboken, New Jersey.
Frankle, M., Levy, J.C., Pupello, D., Siegal, S., Saleem, A., Mighell, M., Vasey, M., 2006. The reverse shoulder prosthesis for glenohumeral arthritis associated with severe rotator cuff deficiency. a minimum two-year follow-up study of sixty patients surgical technique. J. Bone Jt. Surg. Am. 88 (Suppl 1 Pt 2), 178–190.
Frankle, M., Siegal, S., Pupello, D., Saleem, A., Mighell, M., Vasey, M., 2005. The reverse shoulder prosthesis for glenohumeral arthritis associated with severe rotator cuff deficiency. A minimum two-year follow-up study of sixty patients. J. Bone Jt. Surg. Am. 87, 1697–1705.
Gerber, C., Pennington, S.D., Nyffeler, R.W., 2009. Reverse total shoulder arthroplasty. J. Am. Acad. Orthop. Surg. 17, 284–295.
Hettrich, C.M., Permeswaran, V.N., Goetz, J.E., Anderson, D.D., 2015. Mechanical tradeoffs associated with glenosphere lateralization in reverse shoulder arthroplasty. J. Shoulder Elb. Surg. / Am. Shoulder Elb. Surg. 24, 1774–1781.
Nyffeler, R.W., Werner, C.M., Simmen, B.R., Gerber, C., 2004. Analysis of a retrieved delta III total shoulder prosthesis. J. Bone Jt. Surg. Br. volume 86, 1187–1191.
O'Brien, S.J., Neves, M.C., Arnoczky, S.P., Rozbruck, S.R., Dicarlo, E.F., Warren, R.F., Schwartz, R., Wickiewicz, T.L., 1990. The anatomy and histology of the inferior glenohumeral ligament complex of the shoulder. Am. J Sport. Med. 18, 449–456.
Oh M.D., Ph. D., J.H., Choi M.D., J.H., 2013. Current concepts of arthroplasty for the treatment of massive rotator cuff tears. J. Korean Orthop. Assoc. 48, 78–87.
Takeuchi, T., Lathi, V.K., Khan, A.M., Hayes, W.C., 1995. Patellofemoral contact pressures exceed the compressive yield strength of UHMWPE in total knee arthroplasties. J. Arthroplast. 10, 363–368.
Walch, G., Bacle, G., Ladermann, A., Nove-Josserand, L., Smithers, C.J., 2012. Do the indications, results, and complications of reverse shoulder arthroplasty change with surgeon's experience? J. shoulder Elb. Surg. / Am. Shoulder Elb. Surg. 21, 1470–1477.
Warner, J.J., Deng, X.H., Warren, R.F., Torzilli, P.A., 1992. Static capsuloligamentous restraints to superior-inferior translation of the glenohumeral joint. Am. J. Sport. Med. 20, 675–685.
Weiss, J.A., Gardiner, J.C., 2001. Computational modeling of ligament mechanics. Crit. Rev. Biomed. Eng. 29, 303–371.
Werner, B.S., Boehm, D., Gohlke, F., 2013. Revision to reverse shoulder arthroplasty with retention of the humeral component. Acta Orthop. 84, 473–478.
Wierks, C., Skolasky, R.L., Ji, J.H., McFarland, E.G., 2009. Reverse total shoulder replacement: intraoperative and early postoperative complications. Clin. Orthop. Relat. Res. 467, 225–234.
Wieser, K., Rahm, S., Schubert, M., Fischer, M.A., Farshad, M., Gerber, C., Meyer, D.C., 2015. Fluoroscopic, magnetic resonance imaging, and electrophysiologic assessment of shoulders with massive tears of the rotator cuff. J. Shoulder Elb. Surg. / Am. Shoulder Elb. Surg. 24, 288–294.